UCLouvain

École polytechnique de Louvain

# Biomineralized nanostructured biointerfaces mimicking extracellular matrix

Author: **Charlotte LAEREMANS**
Supervisors: **Sophie DEMOUSTIER, Christine DUPONT**
Readers: **Damien DEBECKER, Jessem LANDOULSI**
Academic year 2020–2021
Master [120] in Biomedical Engineering

# Abstract

The elaboration of biointerfaces mimicking native tissue environments for tissue engineering applications has attracted growing interest due to the emergence of nanotechnologies in biological research. The particular case of bone tissue engineering is especially challenging due to the complex anatomical structure and the important functions that bones exert in the body. A promising scaffold for bone regeneration would have a composition and structure similar the bone extracellular matrix (ECM), which constitutes a structural framework providing mechanical support to bone cells *in vivo*. To this end, the subsequent work presents a method to produce biomineralized biointerfaces mimicking the bone ECM. Inspired by the composition and structure of the ECM, the biointerfaces produced consist of intersected nanotubes composed of collagen (Col) and hyaluronic acid (HA). To achieve this, the layer-by-layer (LbL) assembly technique is performed in polycarbonate membranes with a tunable network of intersected nanopores. In order to obtain biointerfaces with suitable mechanical stability, hydroxyapatite, the major component of the inorganic bone ECM, is formed within the nanotubes by the enzymatic-induced mineralization technique using alkaline phosphatase (ALP).

The promising results showed that LbL assembly of $(Col/HA)_3(PAH/ALP)_5$ multilayers followed by mineralization was successful both on planar surfaces and in nanoporous templates. A predominant role of the collagen-based multilayers on the mineralization process was highlighted by a more pronounced mineralization on silicon wafers and the formation of a higher amount of nanotubes reaching longer lengths. Lowering the temperature of the cross-linking process was shown to lead to a better stabilization of the Col/HA based multilayers and using PC membranes with a pore size of 500 nm allowed to achieve promising results of nanotubes with the expected length of the template thickness. This Master thesis therefore pave the way for future investigations towards the formation of intersected nanotube networks with improved mechanical stability mimicking the bone ECM.

# Acknowledgements

I would like to thank all the people who have personally contributed in one way or another to this Master thesis.

First of all, I would like to particularly thank my promoters of UCLouvain and my supervisor at the LRS in Paris, Sophie Demoustier, Christine Dupont and Jessem Landoulsi for their availability, supervision, valuable advice and encouragement throughout my research.

I would also like to thank Damien Debecker for accepting to be part of the readers of my Master thesis.

I also thank Delphine Magnin, for her daily help and good mood during the first academic semester. Especially for all her explanations on the laboratory practices and particularly the use of the SEM.

I would like to thank Jihye Lee and Brittany Foley, my office mates at LRS, for their warm welcome, help and availability throughout my internship.

I thank Clément Guibert for the fruitful discussions and his presence at the meetings and Adama Konaté, assistant engineer at UTC-SAPC, for all the time he spent doing the SEM analyses of my samples during the second academic semester. I also warmly thank Joanne Lê-Chesnais for the ATR analyses.

Thanks to the members of the BSMA and LRS laboratories for welcoming me, the positive working climate and the access to the equipment.

Finally, many thanks to my family for their support and encouraging words during the writing of this thesis despite the distance.

# Contents

# List of abbreviations

**ALG** Alginate

**ALP** Alkaline phosphatase

**ATR** Attenuated total reflectance

**CaP** Calcium phosphate

**Col** Collagen

**ECM** Extracellular matrix

**EDC** N-(3-Dimethylaminopropyl)-N-ethylcarbodiimide hydrochloride

**EDX** Energy-dispersive X-ray spectroscopy

**FTIR** Fourier-transform infrared

**HA** Hyaluronic acid

**HAp** Hydroxyapatite

**LbL** Layer-by-layer

**NHS** N-hydroxysuccinimide

**PAH** Poly(allylamine hydrochloride)

**PC** Polycarbonate

**PEI** Polyethyleneimine

**PET** Poly(ethylene terephthalate)

**pnp** 4-Nitrophenol

**pnpp** 4-Nitrophenyl phosphate

**PPy** Polypyrrole

**PSS** Poly(styrene sulfonate)

**Py** Pyrrole

**RT** Room temperature

**SEM** Scanning electron microscopy

**TEM** Transmission electron microscopy

# Introduction

### Context of the research work

During the last decades, the elaboration of biointerfaces mimicking native tissue environments for applications such as tissue engineering and regenerative medicine has attracted growing interest due to the emergence of nanotechnologies in biological research. Tissue engineering is a promising solution for the regeneration of tissues damaged by trauma, fractures or diseases because it prevents organ rejection and solves donor shortages by avoiding foreign tissue transplantation. This multidisciplinary approach consists of developing functional tissue substitutes based on the combination of three basic elements : cells generating the desired tissue, growth factors guiding the cells to the tissue growth and scaffolds providing structural support to the first two elements. The development of the appropriate scaffold that reproduces the architecture of the targeted tissue, promoting cell adhesion, proliferation and differentiation as in the human body is not free of challenges. *In vivo*, the extracellular matrix (ECM) acts as a physical scaffold that provides mechanical stability and biochemical cues to cells. This three-dimensional network is composed of specific proteins and polysaccharides and its exact composition is unique for each tissue of the body.[1] A suitable scaffold for tissue regeneration has therefore a composition and structure similar to the extracellular matrix of the target tissue.

The particular case of bone tissue engineering, on which this thesis focuses, is especially challenging due to the complex anatomical structure and the important functions that bones exert in the body, such as locomotion, weight-bearing and protection of vital organs. Bone is a mineralized connective tissue that is highly dynamic as it is continuously undergoing remodeling. This process is highly complex and consists of the replacement of old bone tissue by new tissue to maintain homeostasis (i.e. a process of thermodynamic equilibrium by biological systems to maintain stability [2]). Bone remodeling involves the coordinated action of bone cells, beginning with bone resorption by osteoclasts followed by a transition to bone formation by osteoblasts. The extracellular matrix of bones actively participates in bone remodeling and constitutes a structural framework that provides mechanical support to the cells. It is composed of type I collagen, hyaluronic acid and noncollagenous proteins, forming the organic part (40%) of the bone ECM, and of inorganic material (60%) consisting mainly of hydroxyapatite, the result of the nucleation of phosphate and calcium ions. The production and deposition of hydroxyapatite crystals between the collagen fibrils takes place in a process called biomineralization. It is performed in the presence of calcium and inorganic phosphate precursors and is facilitated by the action of the alkaline phosphatase (ALP) enzyme which increases the local concentration of inorganic phosphate. [3, 4]

Numerous techniques aiming at designing bioinspired materials mimicking the mechanical and morphological properties of the extracellular matrix are widely found in the literature. One technique that stands out for its ease, versatility and low cost is the template-assisted layer-by-layer (LbL) deposition method. This process allows the assembly of ECM-derived macromolecules into multilayers by alternately depositing oppositely-charged species that interact by electrostatic attraction. The build-up of these multilayers in a nanoporous template allows the formation of three-dimensional structures with well-defined morphologies and composition. The great advantage of these templates is the ability to easily tune their properties such as pore diameter or pore orientation and therefore allowing to obtain specific structures such as a network of intersected nanotubes.

The LbL assembly of biomacromolecules in nanoporous membranes make it possible to synthesize functional nanotubes whose dimensions and composition resemble those of the extracellular matrix of bones, providing excellent biocompatible and osteoinductive (i.e. growth of new bone tissue on a surface [5]) properties. However, ECM-like nanotubes obtained in this way lack adequate mechanical stability. In order to overcome this, their strengthening has been investigated by taking inspiration from the inorganic bone ECM. Indeed, inducing the mineralization of these nanostructures allows improving their mechanical properties. This was successfully achieved in a previous work of Colaço et al. where they synthesized nanotubes composed of the main constituents of the organic bone ECM, i.e. collagen and hyaluronic acid, and being biomineralized mediated by the action of the alkaline phosphatase enzyme. [6]

### Objectives of the Master thesis

Based on this previous promising study, this Master thesis primarily aims at producing **biomineralized biointerfaces mimicking the bone extracellular matrix** which could be useful in the future for tissue engineering applications. The synthesised structure could indeed serve as a biointerface for the reconstruction of damaged bone tissue that cannot be spontaneously healed by osteoblasts.
Inspired by the composition and structure of the ECM, the biointerfaces produced consist of **intersected nanotubes** composed of **collagen** and **hyaluronic acid**. To achieve this, the **layer-by-layer assembly** technique is performed in a polycarbonate membrane with a tunable network of intersected nanopores. In order to obtain a network with suitable mechanical stability, hydroxyapatite, the major component of the inorganic bone ECM, is formed within the nanotubes by the **enzymatic-induced mineralization** technique using **alkaline phosphatase**.
The final objective is to fine-tune a series of parameters, such as the conditions of the different LbL assembly steps or the composition of the multilayers, to **modulate the mechanical properties** of the produced biomineralized nanostructured biointerfaces mimicking the bone ECM.

### Thesis structure

This thesis is structured in four main chapters. Chapter 1 will provide the theoretical background related to the synthesis of biomineralized nanostructures mimicking the ECM. After a presentation of the composition of the extracellular matrix and its biomineralization, the template synthesis and layer-by-layer assembly techniques used for the synthesis of the structures will be detailed. Finally, a review of the major advances in the production of ECM-based nanotubes will be presented.

Chapter 2 will first describe the different materials used for the formation of the nanotube networks. Then, the experimental processes of LbL assembly and mineralization on different substrates and the characterisation techniques will be detailed.

In Chapter 3, the results obtained will be presented and discussed. This chapter is composed of a first part which will preliminarily study the assembly and mineralization of multilayers on planar surfaces. This is followed by two sections investigating the assembly and mineralization of these multilayers in different porous templates and the influence of certain parameters on the stability of the nanotubes formed. The last part will be a discussion aiming at comparing the two types of porous templates used.

Finally, Chapter 4 will summarise the main conclusions and give perspectives for further improvements and future investigations.

# Chapter 1

# State of the Art

This chapter aims at outlining the theoretical background related to the production of biomineralized nanostructured biointerfaces mimicking the extracellular matrix (ECM). It first describes in detail the extracellular matrix and particularly its main components. In a second step, the different mechanisms of biomineralization are explained as well as the role of the enzyme alkaline phosphatase in this process. The application of enzymatic-induced mineralization inspired by this mechanism is also discussed in this section. Next, methods for the synthesis of the nanostructures are highlighted, in particular the template synthesis method and layer-by-layer assembly. The growth mechanism of polyelectrolyte multilayers and more precisely of protein-based multilayers are also explained in more detail. Finally, the major advances in the production of nanotubes based on the layer-by-layer assembly of ECM components in porous template are reviewed.

## 1.1 The bone extracellular matrix

The extracellular matrix (ECM) is a complex and dynamic three-dimensional network secreted by cells. Its main functions are to provide physical scaffolding, mechanical stability and biochemical cues to the cells. Thereby, it plays an important role in cell migration, proliferation and differentiation for tissue formation and homeostasis. Indeed, integrins and other cell adhesion receptors can bind to the ECM. These interactions allow communication between the intra- and extracellular environment, which is at the origin of tissue formation and homeostasis. Overall, the ECM is composed of specific proteins and polysaccharides but its exact composition and topology are unique for each tissue of the body depending on their main function. [1, 7, 8, 9, 10]

In bones, the ECM interacts dynamically with bone cells, i.e. osteoblasts and osteoclasts, to regulate the formation of new bone tissues. This ECM is made up of organic components (about 40%) giving elastic properties to the bones and inorganic components (about 60%) which give rigidity. However, the exact composition of bone ECM differs from person to person depending on age, health, gender and living conditions. The organic components consist mainly of type I collagen and hyaluronic acid but also of non-collagenous proteins, while the inorganic components mostly contain hydroxyapatite, a calcium phosphate. [1, 8]

### 1.1.1 Organic components of bone ECM

#### Collagen

Collagen constitutes the main structural element of the organic part of the bone ECM, about 90%, and it is also the most abundant class of proteins in the human body in general. Its main functions are to provide tensile strength, maintain homeostasis and direct tissue development. [7, 10].
Collagen fibres are a heterogeneous mix of different types but the one that predominates in bones is type I collagen. It is an extremely dense and crosslinked collagen that gives mechanical and chemical stability to the bones. [7, 11, 12]

The unique properties of type I collagen result from the structural complexity of the collagen molecule, which is shown in Figure 1.1. It is a right-handed triple helix with a length and a diameter of about 300 nm and 1.5 nm respectively. It is composed of three polypeptide $\alpha$-chains and each of these chains is a left-handed helix. The polypeptide chains are made up of repeating amino acids triplets, Gly-X-Y, where the X and Y positions are most of the time occupied by proline (Pro) and hydroxyproline (Hyp) respectively. These chains are linked together by direct interchain hydrogen-bonds which limit rotation, therefore ensuring the stability of the triple-helix collagen.
The collagen molecules self-assemble by fibrillogenesis to form microfibrils which then lead to collagen fibrils. Collagen molecules are shifted by 67 nm within these microfibrils. Depending on the type of tissue, the diameter of these collagen fibrils reaches values between 10 and 500 nm. [12, 13]

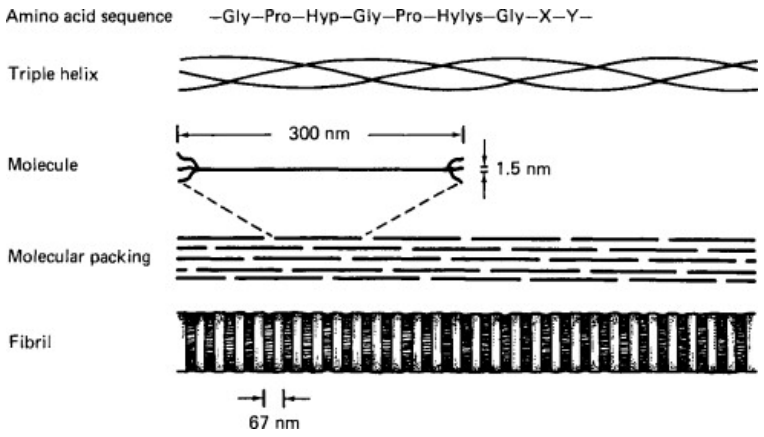


Figure 1.1: Structure of type I collagen from amino acid sequence (above) to collagen fibril (below).[14]

Thanks to its excellent biological and physicochemical properties, collagen is used in many biomedical applications. Since it is the most present compound in bone ECM, many collagen-based scaffolds are used in tissue regeneration due to their ability to deliver biological information for cell migration, adhesion and proliferation. [15]

### Hyaluronic Acid

Hyaluronic acid (HA) is the second important class of macromolecules of the organic bone ECM. It is a long linear polysaccharide that is widely distributed in the human body. More precisely, hyaluronic acid is an acidic, non-sulfonated glycosaminoglycan and is composed of repeating disaccharide units made of D-glucuronic acid and N-acetyl glucosamine, as represented in Figure 1.2. [16]

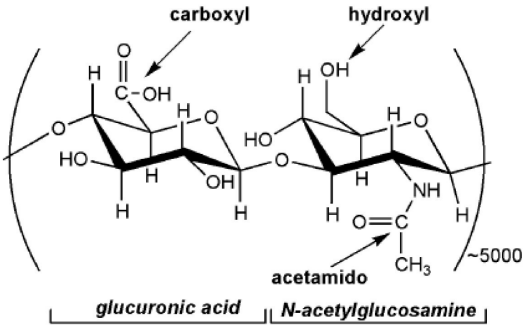


Figure 1.2: Chemical structure of the disaccharide repeating unit of hyaluronic acid with indications of the groups influencing the structural and physical properties, i.e. carboxyl, hydroxyl and acetamido groups. [17]

The particularity of hyaluronic acid is its capacity to tightly bind water molecules through its hydroxyl groups by forming hydrogen bonds, which makes it highly hydrophilic. Bonds are also formed between the carboxyl and acetamido groups of the disaccharide units components forming a left-handed helix. These groups are highlighted on Figure 1.2. Moreover, HA is very viscous in aqueous solution due to strong intermolecular interactions as well as a high molecular weight which can reach values up to $10^8$ Da. [16, 18, 19]
Given its chemical and physical properties, the main functions of HA are to maintain and modulate the viscoelasticity of the ECM. It therefore has a role of lubrication and support of the cellular structure. In this way, it allows cells and other ECM components such as collagen to be maintained in a hydrated and stable extracellular space. [8, 10, 16, 19]
Due to its unique properties, hyaluronic acid widely studied for therapeutic applications such as the development of HA-based carriers to deliver drugs or proteins. It is also used for wound healing due to its role in tissue repair and for tissue regeneration in the form of a 3D HA-based microenvironment. [18, 19]

### 1.1.2 Inorganic components of bone ECM

Hydroxyapatite (HAp) is the main inorganic constituent of the ECM of bones and, in general, of the hard tissues of the human body. The deposition of hydroxyapatite in the ECM takes place in a process called biomineralization. This procedure consists of the production and deposition of hydroxyapatite between the collagen fibrils. [1, 11] This mechanism of mineralization is described in more detail in section 1.2.
HAp is one of the most stable calcium phosphate salt with $Ca_{10}(PO_4)_6(OH)_2$ as chemical formula.
Large variations in HAp composition are present and in general it is a relatively non-stoichiometric solid. The Ca/P ratio is used to quantify this non-stoichiometry, the ratio in the stoichiometric case being 1.67, and also to determine the acid-base behaviour. Indeed, the properties will be different depending on this ratio, and thus depending on the non-stoichiometry. The solid will be more acidic in the case of a Ca deficit, thus at a low Ca/P ratio, while it will be more basic when the ratio is higher than the stoichiometric case. [20]
The crystallographic structure of HAp is usually hexagonal with the unit cell parameters being a = b = 0.942 nm, c = 0.688 nm and $\gamma = 120°$. As it is represented on Figure 1.3, the $PO_4^{3-}$ ions occupy tetrahedral sites and the $Ca^{2+}$ ions occur in two non-equivalent sites. Four calcium ions, called Ca(I) or columnar Ca, are distributed vertically along the c-axis and six calcium ions, called Ca(II) or screw axis Ca, are arranged triangularly around the c-axis adjacent to the $OH^-$ ions. [20, 21]
Hydroxyapatite has excellent biocompatible and osteoconductive properties. This is why it is widely used as biomedical materials such as bone tissue engineering scaffold, drug-delivery carrier or bone fillings. [21, 22]

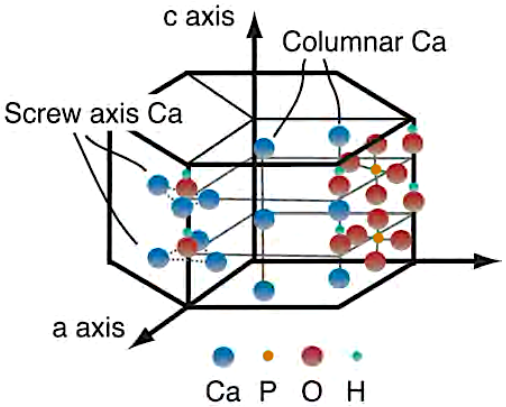


Figure 1.3: Crystallographic structure of hydroxyapatite representing the occupation sites of the $PO_4^{3-}$ ions as well as the two different sites of the $Ca^{2+}$ ions, i.e. screw axis Ca and columnar Ca. (Adapted from [23])

## 1.2 Biomineralization

Biomineralization is the mechanism by which hydroxyapatite is deposited in an organized manner in the extracellular matrix of hard tissues. More precisely, it is the formation of apatite crystals in collagen fibrils. Tissues mineralization plays an essential role in ensuring rigidity and mechanical strength. The main function of hard tissues is therefore to support the body weight and allow locomotion. If this process is not well regulated, mineralization will be excessive or insufficient, which is the main cause of bone disease. An example is Osteomalacia, a metabolic bone disease caused by a lack of minerals that results in softening of the bones. Understanding these diseases and their causes has made it possible to identify the important agents in biomineralization and thus to deduce its mechanism. [24, 25]

### 1.2.1 Mechanisms of collagen biomineralization

Despite the numerous studies dedicated to the determination of the exact mechanism of mineralization, it remains highly debated. Two main theories have been identified: direct nucleation of calcium phosphate (CaP) crystals in collagen fibrils and mineralization mediated by matrix vesicles. These two different routes are schematically summarized in Figure 1.4.

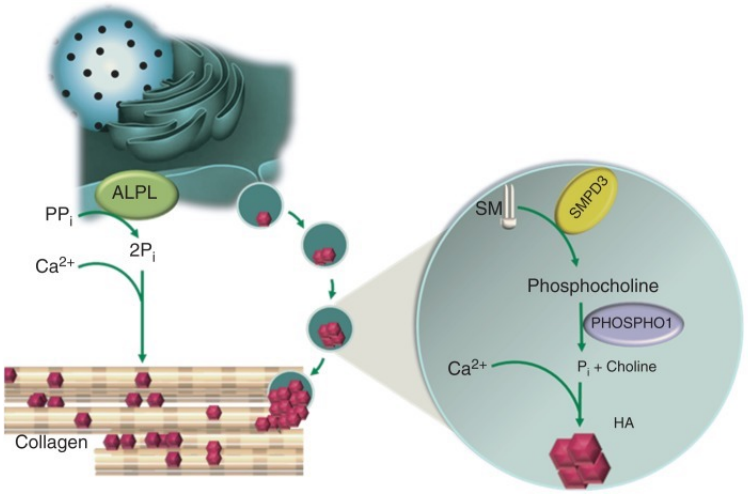


Figure 1.4: Two main routes of biomineralization mechanism : collagen template-mediated (left) and matrix vesicle-mediated (right) mineralization. [25]

**Collagen template-mediated biomineralization** Direct nucleation in collagen fibrils consists firstly of the formation of stable mineral droplets comprising CaP clusters with biopolymers that bind to specific regions on the collagen fibrils. In order for cluster formation to take place, the extracellular level of ionic calcium ($Ca^{2+}$) and ionic phosphate (Pi) must be sufficiently high. This is followed by the diffusion through the fibres where the droplets solidify and arrange themselves into hydroxyapatite crystals oriented along the collagen fibrils. Therefore the size and organisation of the fibrils will determine the final dimensions of the crystals. These steps are illustrated in detail in Figure 1.5. [26]

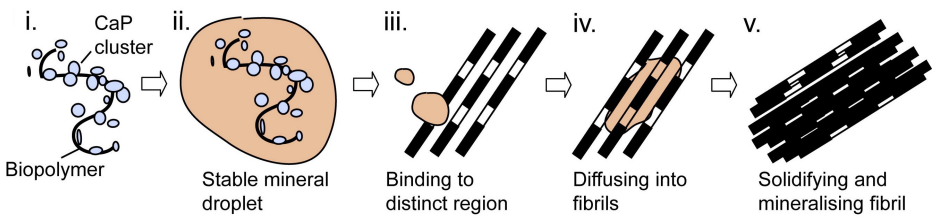


Figure 1.5: Mechanism of direct nucleation of calcium phosphate crystals in collagen fibrils from the the formation of stable mineral droplets to their solidification in collagen fibrils. [26]

**Matrix vesicle-mediated biomineralization** This second route requires the production of nanosized matrix vesicles by the osteoblasts, more precisely by polarised budding of their surface membrane. The initial phase of this route consists of the formation of hydroxyapatite crystals in these vesicles from $Ca^{2+}$ ions and inorganic phosphate (Pi). This step is facilitated by the production of phosphate by the cytosolic phosphatase (PHOSPHO1) through hydrolysis of phosphocholine and phosphoethanolamine derived from the phospholipid membrane. The next phase is therefore the destruction of the vesicle membrane. This will expose the formed HAp to the extracellular fluid and if the fluid contains an appropriate concentration of calcium and phosphate, it will support the continuous formation of new HAp crystals. Finally, these crystals integrate into the collagen fibrils. This mechanism is illustrated on the right part of the scheme in Figure 1.4. [24, 26, 27]

Depending on the distribution of hydroxyapatite relative to the collagen fibrils, the biomineralization of collagen can be divided into intrafibrillar and extrafibrillar mineralization.
Intrafibrillar mineralization consists of the incorporation of HAp into the gap zone of collagen fibrils. It has been shown that the minerals nucleate preferentially in that zone and grow with their c-axis parallel to the main axis of the fibrils exceeding the gap zone, as represented in figure 1.6(A).
Extrafibrillar mineralization is a more straight-forward and well-understood process compared to intrafibrillar mineralization. It involves the deposition of HAp crystals on the surface of collagen fibrils in the absence of inhibitors. An image of a result of this process is shown in Figure 1.6(B). [28, 29]

(A) 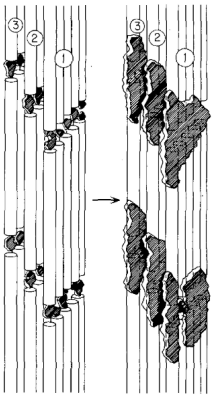

(B) 


Figure 1.6: (A) Intrafibrillar mineralization, HAp forming in the gap zone of collagen fibrils [29] and (B) Extrafibrillar mineralization, HAp depositing on the surface of collagen fibrils [30].

It was long believed that the role of collagen in biomineralization was essentially passive and that it only served as a structural matrix. However, it has been shown that it was rather an active scaffold. Indeed, a positively-charged region was discovered between the gap zone and the overlap zone of collagen molecules arranged in the fibrils. This region provides binding sites for non-collagenous proteins of the extracellular matrix, therefore regulating crystal deposition. Indeed, it seems that non-collagenous proteins have a significant influence as signaling molecules in inhibition and promotion mechanisms of the mineralization process. In addition, the role of collagen in biomineralization is not only to initiate and direct the growth of hydroxyapatite, but it also affects the size, shape and orientation of the formed crystal through its fibrillar structure. [24, 28, 29]

### 1.2.2 Role of alkaline phosphatase in biomineralization

The level of the ratio between inorganic phosphate (Pi) and inorganic pyrophosphate (PPi) is particularly crucial in the mineralization process. Indeed, PPi, produced by intracellular and extracellular enzymatic reactions, has been shown to be an inhibitor of mineralization. Alkaline phosphatase (ALP) promotes hydroxyapatite formation by reducing the amount of PPi in the bone microenvironment and increasing the quantity of Pi required for biomineralization. The role of ALP is therefore crucial in the mineralization of hard tissue and is thus expressed early in the development. [25]

Alkaline phosphatase is a plasma membrane-bound enzyme. It catalyses at high pH values the hy-

drolysis reaction of various monophosphate esters, R-O-$PO_3$, releasing inorganic phosphate and alcohol with a chemical reaction as follows:

$$R - PO_4^{2-} + H_2O \rightarrow R - OH + HPO_4^{2-}$$

Human ALP is divided into four isoenzymes depending on the site of tissue expression, namely placental, intestinal, germ cell and tissue non-specific or liver/bone/kidney alkaline phosphatase. Each isoenzyme is encoded by separate gene loci from the same common ancestral gene and they are 86-98$\%$ identical at the amino acid level. [31]
ALP is a metalloenzyme whose active site is composed of a serine residue and three metal ions, two $Zn^{2+}$ and one $Mg^{2+}$, essential for enzymatic activity. The three-dimensional structure of ALP is a dimer and each monomer contains four metal atoms, including calcium and the three atoms forming the active site, and a phosphate ion. Alkaline phosphatase is attached to the plasma membrane through the glycosylphosphatidyl-inositol (GPI) anchors. The mammalian ALP is characterised by a specific domain, a flexible loop, which is called the crown domain. An overview of the three-dimensional structure of ALP is shown in Figure 1.7. [27, 31, 32]

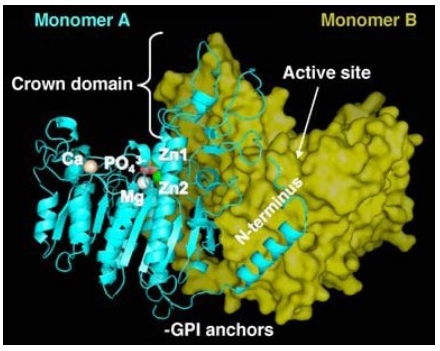


Figure 1.7: Three-dimensional structure of alkaline phosphatase representing monomer A in ribbon form and monomer B in surface representation form. The four metal sites, phosphate ions, crown domain and GPI anchor are highlighted. [32]

### 1.2.3 Enzymatic-induced mineralization

Bone-substituting materials mineralization has been widely investigated in the literature for its many advantages for clinical applications. Firstly, hydroxyapatite minerals increase the biological performance of scaffolds by improving their bioactivity, thus enhancing the incorporation of the material with the surrounding tissues. Secondly, HAp crystals have an intrinsic affinity with biological proteins such as growth factors that will stimulate the natural formation of new bone tissue. Then, the incorporation of hydroxyapatite also improves the mechanical properties of the formed material, resembling those of bones. Finally, as mineralization leads to the formation of rougher and stiffer surfaces, it promotes the differentiation of cells into osteoblasts and thus improves biocompatibility with bone tissue. [33]

The most popular and simple strategy to induce mineralization, and thus to introduce hydroxyapatite into a scaffold, is the incorporation of inorganic phases such as calcium phosphate ceramics. These particles act as nucleation sites for the formation of HAp crystals. However, this technique tends to result in aggregation of the CaP particles, inhomogeneous dispersion and poor reproducibility. [33, 34]
An alternative to the incorporation of calcium phosphate particles is the use of alkaline phosphatase to induce mineralization due to its crucial role in the *in vivo* mineralization of hard tissue. Therefore, extensive research has been conducted on the incorporation of ALP into scaffolds and on its ability to induce mineralization.

Enzymatic mineralization allows the formation of hydroxyapatite on or within materials in a homogeneous manner. This technique uses homogeneously dispersed enzymes, in this case alkaline phosphatase, which convert precursor molecules into active mineralization components. More precisely, ALP-containing materials are incubated in a calcium glycerophosphate solution and under the action of

ALP, phosphate is released and reacts with calcium ions to build CaP particles leading to the formation of HAp. [33, 35]

The biofunctionalization of surfaces by ALP has attracted much interest in recent years. Indeed, numerous research studies have focused on the immobilisation of ALP on inert surfaces to catalyse and induce the production of hydroxyapatite. Different techniques of ALP immobilisation on surfaces have been identified, such as binding the enzyme by a covalent cross-linking system or incorporating it into a multilayer film. It was demonstrated that the enzymatic activity of ALP was preserved despite immobilisation and that a mineralized film was successfully formed. In addition, it has been shown that the growth mechanism of the mineralized layer was dependent on the physicochemical conditions and particularly on temperature and pH. [36, 37]

The numerous investigations on enzymatic-induced mineralization are not only limited to flat surfaces. Indeed, the immobilisation of ALP in 3D scaffolds has been widely studied in order to induce mineralization in these materials which is particularly interesting for applications such as tissue engineering. Due to their many advantages such as the ease of incorporating cells and bioactive substances, hydrogels are a widely investigated class of materials. To induce strong interactions with hard tissues such as bones, a lot of research is aimed at developing hydrogels capable of enzyme-induced mineralization. Polysaccharide hydrogels containing uniformly distributed hydroxyapatite minerals were obtained by immobilising ALP in the hydrogel network by fixation with a reactive polyglutaraldehyde (PGL) solution, as represented on Figure 1.8. It has been shown that this technique of enzymatic-induced mineralization allows easy tuning of the mechanical properties of hydrogels. [35, 38] A dense and uniform deposition of hydroxyapatite minerals on a chitosan scaffold was also achieved by Li et al. They highlighted the important parameters for the optimal decomposition of calcium glycerophosphate by ALP leading to HAp formation. The main ones are the concentration of ALP and calcium source, the incubation time in the substrate and the characteristics of the chitosan template. They also demonstrated through *in vitro* and *in vivo* experiments that the presence of HAp in the scaffold promoted osteogenic differentiation of pre-osteoblast cells and tissue integration through improved cell adhesion, proliferation and viability. [34] In addition, enzymatic-induced mineralization in hydrogels formed from type I collagen, the main organic component of ECM, have led to an excellent mineral/polymer ratio offering a promising alternative for the repair of bone defects. [33]

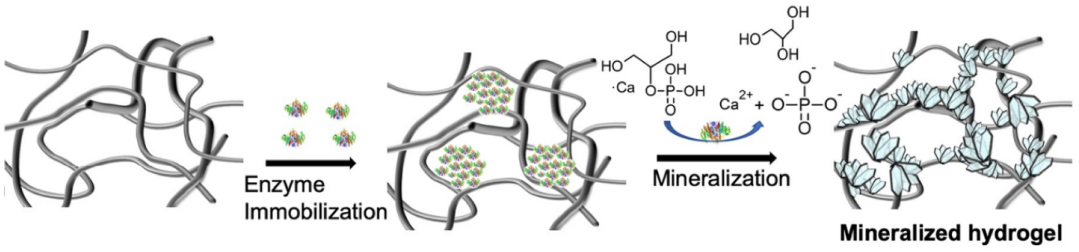


Figure 1.8: Mechanism of enzymatic-induced mineralization in hydrogels. ALP is first immobilised in the structure to induce mineralization and the formation of HAp crystals in the hydrogel. (Adapted from [35]).

## 1.3 Template synthesis

Nanofabrication techniques are processes that allow the construction of engineered nanostructures with at least one dimension smaller than 100 nm. These methods have been strongly developed in recent years due to numerous technological applications in various fields such as informatics, nanoelectronics, nano-medicine and optics. The major need is therefore to manufacture nanomaterials with the desired physical, structural, optical or electronic properties.
These nanofabrication techniques are divided into two main categories : "bottom-up" and "top-down" methods. A "bottom-up" approach involves the assembly of molecular or atomic components into larger

and more complex structures. While a "top-down" approach consists in starting from larger dimensions and reducing them to the desired dimensions, shapes and characteristics. [39]

The hard templating method is a bottom-up approach consisting in the deposition of materials in the pores of a template membrane in order to obtain micro- or nanoscopic structures, as schematically represented on Figure 1.9. Depending on the size and geometry of the pores but also on the deposited materials, the obtained structures can be homogeneous or heterogeneous, of cylindrical, tubular or fibrillar shape and of desired length. [40]

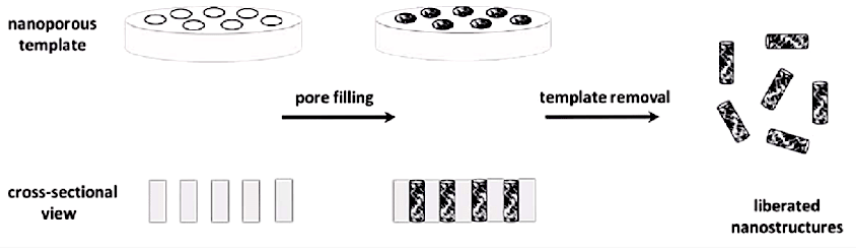


Figure 1.9: Template synthesis process consisting of the filling of the template nanopores followed by the template removal to release the formed nanostructures. [41]

The main role of the template membrane is therefore to allow the reproduction of the desired structures by acting as a skeleton. The two most commonly used and commercially-available membrane templates are ion-track etched and anodized aluminium membranes. These are characterized by cylindrical pores through the thickness of the membrane and flat external surfaces.
In the ion-track etched membrane, nanoscale or microscale cylindrical holes are formed by exposure to an ion source. To do this, a polymer film is subjected to a heavy ion beam in a cyclotron while being unwound at a constant speed. The intensity of the ion beam and the unwinding speed determine the pore density. Then, the damaged tracks formed in the membrane are selectively chemically etched to obtain the desired pores. Figure 1.10 shows the resulting surface of an ion-track etched membrane and the polymer film that is unwound.
The most common track-etched membranes are made of polycarbonate and can have pore diameters ranging from 10 nm to 30 $\mu$m and a porosity up to 50% . The size of these pores depends on the etching conditions such as the temperature and the nature and concentration of the chemical etchant.[42, 43]

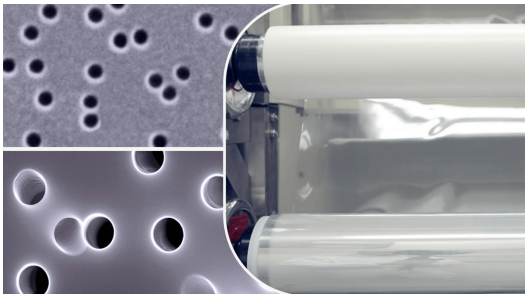

Figure 1.10: Surfaces of ion-track etched membranes (left) and unwinding of a polymer film during ion beaming (right). [42]

In anodized alumina membranes, nanoscopic pores arranged in a hexagonal array are formed by anodization. This is an electrochemical process by which pores self-form in an aluminium oxide film. The pores diameter can range from 5 to 300 nm and the length varies according to the anodization time. Due to their excellent thermal properties and ease of fabrication, these membranes are mainly used for the production of metallic and semiconductor nanowires. [43]

## 1.4 Layer-by-Layer assembly

Layer-by-layer (LbL) assembly is one of several techniques used to fill the pores of template membranes. This easy, versatile and inexpensive process allows the formation of multilayers with tailored properties by sequentially depositing different types of species such as nanoparticles, polymers, proteins and lipids in various templates. The assembly of these species into multilayers can be done through different types of intermolecular interactions such as hydrogen bonding, covalent bonding, hydrophobic interactions or complementary base pairing, but it is mainly conducted through electrostatic interactions, as illustrated in Figure 1.11.
In practice, the first step of this process is the adsorption of a charged species onto a substrate carrying an opposite charge by immersing it into a solution of the layering material. In Figure 1.11, this step is represented by the adsorption of the polyanion on the positively-charged surface. This is followed by a washing step to remove the unbound material and then the adsorption of a second species of opposite charge, the polycation represented on Figure 1.11. Different multilayers are therefore formed by the alternating adsorption of oppositely charged species onto the substrate with high freedom of the number of layers formed. [44, 45, 46]

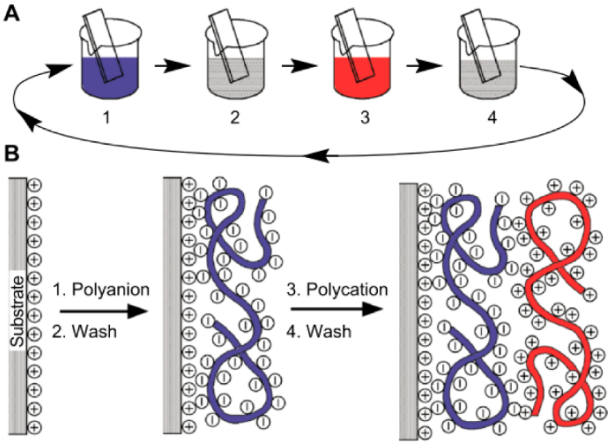


Figure 1.11: Mechanism of layer-by-layer assembly consisting of the alternating adsorption of oppositely charged species. [46]

By varying the type of adsorbed species, the type of substrate used and the number of layers deposited, LbL films with desired properties such as composition, thickness and function can be obtained. Two main classes of templating substrates are commonly used with the layer-by-layer assembly technique : planar and colloidal which can be both nonporous and porous.
The LbL templating technique with a planar porous template as substrate allows the formation of three-dimensional nanostructures with well-defined morphologies. As shown on Figure 1.12, by immersing the porous template with cylindrical pores in solutions of polyelectrolytes, LbL assembly occurs by the diffusion of these polyelectrolytes through the template pores. Removing the template allows to obtain nanotubes whose composition, thickness, diameter and length are defined by the type of species in the multilayers, the number of multilayers deposited, the pore diameter and the membrane thickness respectively. [44]

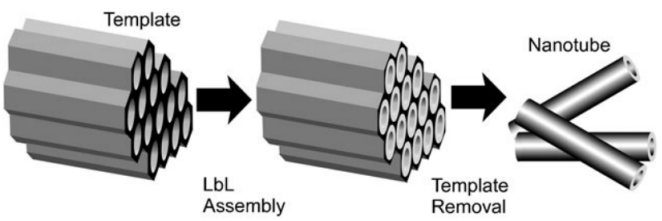


Figure 1.12: Layer-by-layer assembly mechanism in a porous planar template leading to the synthesis of nanotubes. [45]

### 1.4.1 Growth mechanism of polyelectrolyte multilayers in porous templates

A considerable amount of research have been carried out on the growth mechanism of polyelectrolyte multilayers on planar surfaces while few similar studies have been performed in porous templates. Indeed, the difficulty is mainly to apply the majority of the characterisation techniques used on surfaces. However, due to the influence of confinement on macromolecular chains, it has been shown that the growth mechanism of polyelectrolyte multilayers in pores is different from the one on flat surfaces. [47]

Alem et al. investigated the growth mechanism of strong polyelectrolytes of different molecular weights, more precisely poly(vinylbenzylammonium chloride) (PVBAC) and poly(styrene sulfonate) (PSS), on flat surfaces and in track-etched polycarbonate membranes. They showed that the growth on surfaces was linear and that the thickness increment was independent of the molar mass of the chains. In the nanopores of the membrane, they observed that the filling process was homogeneous throughout the entire thickness of the membrane and that the thickness increment per deposition cycle was significantly larger in membrane pores than on flat surfaces. The authors showed that the size of the chains had no significant influence on the final structure and the thickness was mainly dependent on the pore diameter. They also observed that the pores of the membranes were quickly completely filled, which can be explained by the entanglement of the chains as they passed through the pores forming a dense gel. [48]

The work of Roy et al. allowed to demonstrate the existence of two regimes in the growth mechanism of polyelectrolytes in porous templates. They investigated the assembly of poly(allylamine hydrochloride) (PAH) and poly(styrene sulfonate) (PSS) of different molecular weights and determined the evolution of the relative radial polyelectrolyte multilayer increment ($\Delta_\mathrm{r}$) as a function of the number of bilayers formed in pores of different sizes. This parameter describes the relative gain in multilayer thickness as a function of the number of bilayers and is defined by the following relation:

$$\Delta_\mathrm{r} = \frac{d_\mathrm{P}(i) - d_\mathrm{P}(n)}{d_\mathrm{P}(i)} \times 100$$

with $d_\mathrm{P}(i)$ the initial pore diameter and $d_\mathrm{P}(n)$ the pore diameter measured after the assembly of $n$ bilayers. The evolution of $\Delta_\mathrm{r}$ in different pore sizes for high and low molecular weight polyelectrolytes was therefore determined, shown in Figure 1.13, and revealed the two growth regimes by the occurrence of a slope change, the second being highlighted by a shaded region on the graphs.

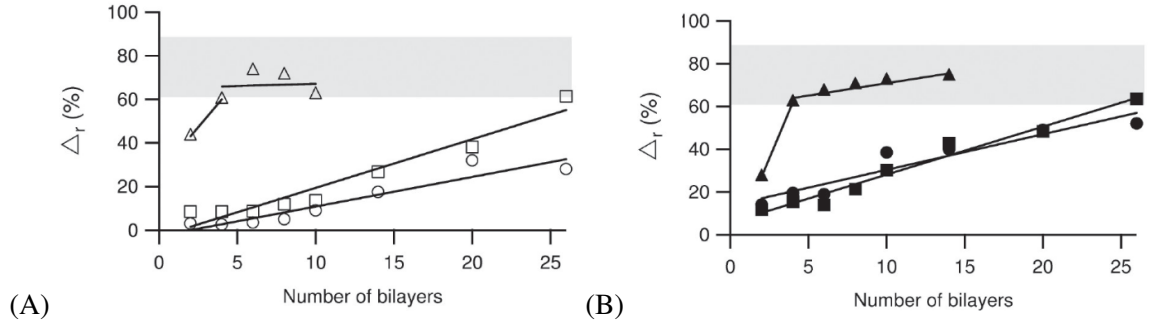


Figure 1.13: Evolution of the relative radial polyelectrolyte multilayer increment ($\Delta_\mathrm{r}$) as a function of the number of PAH and PSS bilayers, of low (A) and high (B) molecular weight, formed in pores of 100 (triangles), 200 (circles) and 500 nm (squares). The shaded region marks the second growth regime determined by a change in slope. [47]

The first growth regime corresponds to the first deposited layers and is similar to that on a flat surface, i.e. linear growth, whereas the second regime shows a decrease in the growth kinetics of multilayers. This suggests that the deposition of polyelectrolytes in the first regime is not limited by their diffusion through the pores of the template and that the adsorption on the pore walls is similar to that on flat surfaces. As suggested by Alem et al., from a certain number of multilayers, the polyelectrolyte chains make

entanglement connections which lead to the formation of a dense gel. This gel slows down the diffusion of polyelectrolytes through the pores, which explains the occurrence of a second growth regime. The diffusion of polyelectrolytes is therefore the growth controlling parameter in this case. The transition between the two regimes depends mainly on the pore size of the template and on parameters influencing the geometrical arrangement of the formed multilayers such as the macromolecular structure of the polyelectrolytes and the type of interaction driving the layer-by-layer assembly. [47, 49]
They also demonstrated that the polyelectrolyte multilayers grew uniformly along the length of the membrane pores and that the diameter of the resulting nanotubes corresponds to the pore size. However, these observations are only valid for a minimum number of bilayers for the structure to be sufficiently rigid. Otherwise, the mechanical integrity of the nanotubes is not preserved and they deform by flattening, scrolling and twisting. By studying the influence of the ionic strength of the solution in the first growth regime, it was shown that thicker multilayers were deposited when the ionic strength increased. This can be explained by the fact that polyelectrolyte chains have a more coiled conformation in solutions of high ionic strength. They also studied the impact of the molecular weight of the polyelectrolytes on the growth of the multilayers in the first regime. They were able to show a slight increase in film thickness for high molecular weight polyelectrolytes depending on the pores diameter, the effect being more significant for medium size pores, i.e. around 200 nm. [47]

### 1.4.2 Growth of protein-based multilayers

Since they are charged and mostly water-soluble, the basic principles of layer-by-layer assembly of polyelectrolytes can be applied with proteins, i.e. polymers consisting of different amino acids. However, it is more difficult to assemble them by LbL due to their high heterogeneity. Indeed, the charge distribution is critical for LbL assembly and compared to polyelectrolytes, proteins are formed from a combination of 20 different amino acids of which only five are charged. [50]

Two main types of parameters influence the LbL assembly of proteins with polyelectrolytes: intrinsic and extrinsic parameters. The former is not specific to the desired multilayers while the latter will define the multilayers. The influence of these parameters has mainly been studied for LbL assembly on flat surfaces, which should therefore be representative for the first growth regime in porous templates, as explained in the previous section. [50]

A first extrinsic parameter that is critical for the layer-by-layer assembly of proteins is pH. It has been shown that the pH of the solution must be sufficiently deviated from the isoelectric point value of the protein, at least one pH unit below or above, for the protein to be adequately charged. Thus when the pH of the solution is lower than the isoelectric point, the protein will have a net positive charge and will have to be assembled with a negative polyelectrolyte for LbL to take place, and vice versa in the case of a higher pH. It should be noted that the pH of the solution must be carefully chosen in order to avoid denaturing the protein. The targeted application must also be taken into account when selecting the pH so that the film formed is not disturbed. Although a smaller amount of protein would be adsorbed into the construct, it is preferable to perform the assembly at the pH of the desired application and thus reach a higher stability.
The presence of salts in solution is a second extrinsic parameter influencing the assembly of protein with polyelectrolytes. As already highlighted in the previous section, the salt concentration has an influence on the conformation of polyelectrolytes. An increase in salt concentration leads to a decrease in electrostatic repulsion which results in a more coiled conformation. In addition, a larger amount of protein is incorporated into the LbL construct at increased salt concentration due to a decrease in lateral repulsion between the adsorbed proteins. However, if the salt concentration is too high, the electrostatic attraction decreases and it is therefore impossible to form a film by alternate adsorption.
The influence of temperature and of protein concentration in the solution are other extrinsic parameters also studied in the growth of multilayers. The rate of diffusion of polyelectrolytes on the surface increases with temperature and protein concentration, adsorption equilibrium can thus be reached faster. This results in a higher amount of proteins being adsorbed on the surface. [50]

The natures of the polyelectrolytes and proteins are the intrinsic parameters influencing their assembly into LbL films. Concerning the nature of the polyelectrolytes, they must be flexible enough to adapt to the structure of the protein. In addition, the nature of their charged group also has a significant influence as the interaction through ion-pair formation varies depending on the polyanion and polycation. Finally, the ability of the polyelectrolyte to form hydrophobic interactions or hydrogen bonds with the protein also plays a role in the LbL film formation. The influence of the nature of the proteins on LbL assembly is a more difficult parameter to generalise due to the large number of different protein structures. The main factors influencing the assembly are geometrical characteristics, charge distribution and the ability to avoid unfolding during adsorption. [50]

To be used in different applications, it is important that the bioactivity of the proteins in the LbL film is preserved. One type of protein that has been particularly studied is enzymes. The most important factor influencing their activity is the diffusion of the substrate through the film. Thus, the nature of the last layer and the presence of spaces between the layers will influence the ability of the enzyme to react when deposited on a flat surface. Concerning the enzymatic activity in LbL films formed in a porous template, it was shown that the film was very active for few added layers, whereas a higher number of layers on a flat surface is required to achieve a similar activity. For a similar number of layers, it was indeed shown that a much higher catalytic speed, up to three times higher, was obtained in a porous template. Indeed, a greater amount of enzyme can be deposited in pores, therefore available to participate in the catalytic reaction. However, the limiting factor is the diffusion of the substrate through the membrane pores. [50, 51, 52]
Extracellular matrix proteins are another class studied in LbL films such as collagen for its biocompatibility improving properties. It should be noted that the order of the layers is important. This was demonstrated in a study of multilayers formed of hyaluronic acid and collagen where only the film terminated by type I collagen allowed chondrosarcoma cells to produce their own ECM. [50]

The growth process of linear polyelectrolytes, more precisely poly(allylamine hydrochloride) (PAH) and poly(styrene sulfonate) (PSS), was compared to the one of globular proteins, i.e. avidin and biotinylated bovine serum albumin, on a flat surface and in a porous anodic aluminium oxide (AAO) by Lazzara et al. It was observed that due to steric limitation the growth terminated faster in the porous template and that the maximum number of layers deposited ($n_{max}$) was significantly lower in the case of protein layers. The $n_{max}$ is defined by a film thickness that remains constant despite the addition of proteins or polyelectrolytes. Indeed, as shown in the graphs on Figure 1.14, the value of $n_{max}$ in the porous substrate is 9 for linear polyelectrolytes whereas it is only 3 in the case of protein multilayers. This can be explained by the influence of the more globular shape of the proteins in the adsorbed state. Therefore, multilayers of linear polyelectrolytes are more compact than those made of more rigid proteins. These observations confirm the presence of the two growth regimes in the case of protein multilayers assembly in a porous template. [49]

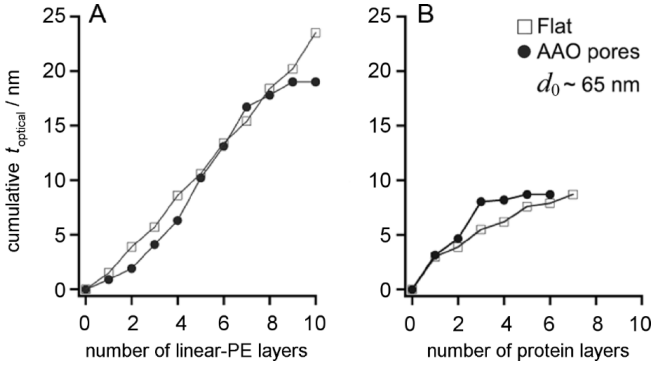


Figure 1.14: Evolution of the cumulative optical film thickness ($t_{optical}$) as a function of the number of linear polyelectrolyte layers (A) and protein layers (B) built on a flat surface (squares) and in an AAO substrate (dots). [49]

## 1.5 ECM-like nanotubes

The evolution of nanotechnology in recent years has led to new research in the development of nanostructures that mimic the extracellular matrix. The combination of template synthesis and layer-by-layer assembly techniques allows the formation of nanotubes whose dimensions and composition are easily tunable. Therefore, the synthesis of nanotubes composed of collagen, hyaluronic acid and/or alkaline phosphatase has drawn attention from researchers to mimic the complex environment in which bone cells evolve. This section reviews the major advances in the production of nanotubes based on the layer-by-layer assembly of ECM components in porous polycarbonate membranes.

Landoulsi et al. studied the formation of size-controlled collagen nanotubes. They were particularly interested in the influence of the parameters related to the geometrical constraint, using porous templates of different diameters, and to the protein conformation, either native or denatured collagen. The denaturation of collagen consists of the thermally induced rupture of the hydrogen bonds and the rearrangement of the triple helix into a random coil conformation. Due to its conformation, it was expected that denatured collagen would diffuse more easily into a porous template.
Owing to its fibrillar structure, collagen has a particular charge distribution and the experimental values of its isoelectric point vary between 6 and 9.3. In this study, collagen was used as a polycation to form multilayers with the strong polyanion poly(styrene sulfonate) (PSS) by the LbL assembly technique.
Their results demonstrated the successful formation of nanotubes in both cases, i.e. with native and denatured collagen, whose outer diameter corresponded to the diameter of the template membrane pores. The major difference observed was the kinetics of the LbL construction. Indeed, denatured collagen, having a coil conformation, diffused more easily into the 200 nm diameter nanopores. The second growth regime, described in section 1.4.1, was more rapidly observed with native collagen because its fibrillar structure favours the formation of entanglements. This difference in behaviour was not observed in the template membrane of 500 nm pores size.
Therefore, the authors were able to conclude that the use of denatured collagen was more interesting for the formation of nanotubes with an external diameter of 200 nm, which is smaller than the length of the native collagen molecule ($\sim$ 300 nm). [13]

With the aim of improving the mechanical integrity of biomacromolecules, Lefèvre et al. focused on the construction of a rigid self-supporting polymer network combining mechanical stability and bioactivity by functionalizing with ECM-derived macromolecules. For this purpose, a structure of intersecting polypyrrole (PPy) nanotubes was synthesised by chemical polymerisation in a polycarbonate membrane with intersected nanopores. The resulting rigid network was biofunctionalized by the LbL technique assembling hyaluronic acid (HA) and type I collagen (Col) biomacromolecules on the surface of the nanotubes.
The authors first monitored the electrophoretic mobility of both macromolecules as a function of pH to determine the favourable conditions for the assembly of multilayers of HA and Col. This allowed them to determine the experimental isoelectric point of these polymers. As represented on the graph on Figure 1.15(A), the isoelectric point of HA was estimated to be lower than 3 and the one of Col around 5.5. To have an electrostatic interaction between these two biomacromolecules, a pH value around 4 was chosen using HA as polyanion and Col as polycation in the LbL assembly.
The SEM images they obtained of their structure proved the successful build-up of biomacromolecules multilayers around the PPy nanotubes, these results are shown in Figure 1.15(B). In addition, they performed a preliminary study on the adhesion and proliferation of murine pre-osteoblast cells. This showed that their formed network elicited good cell adhesion and proliferation, which is therefore promising for future use as a cell-instructive material.
In conclusion, the authors highlighted the successful construction of a hybrid structure with advantageous features such as easily tunable geometry, interconnected porosity, mechanical stability and excellent biocompatibility. [53]

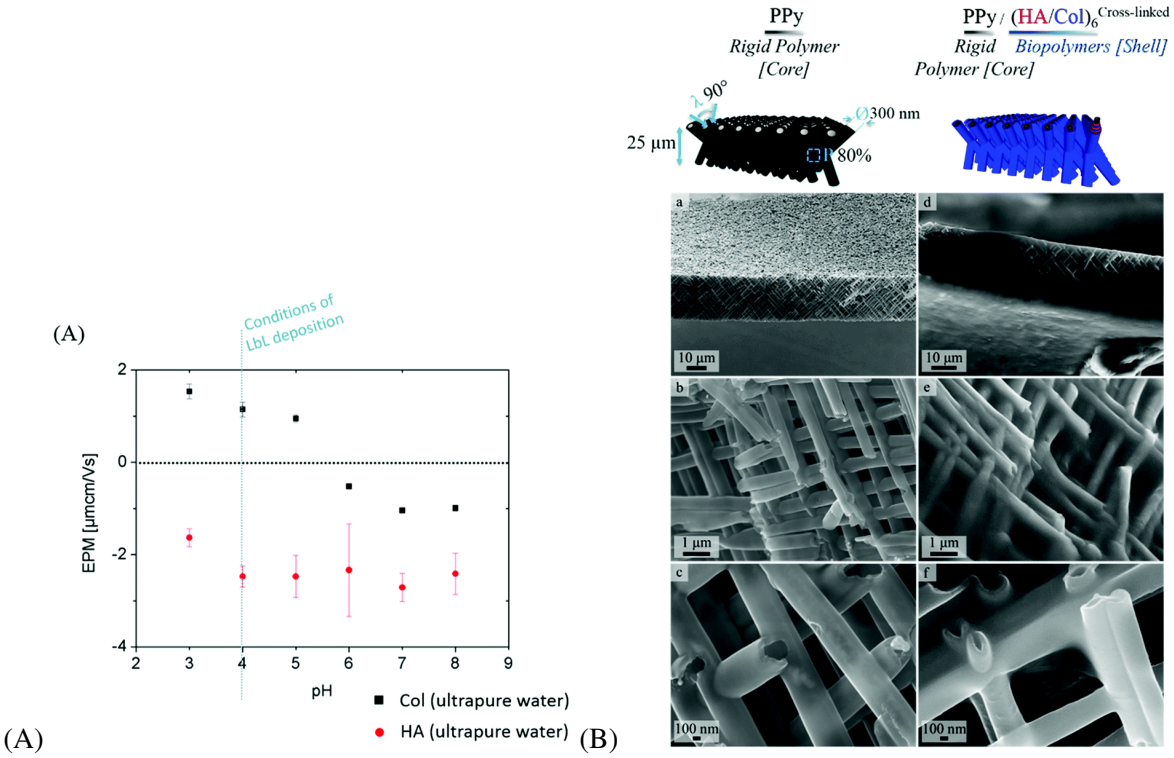


Figure 1.15: Results of Lefèvre et al. : (A) Electrophoretic mobility of HA (red dots) and Col (black squares) as a function of pH and (B) SEM images of the network of intersected PPy nanotubes before biofunctionalization (a-c) and after LbL deposition of $(HA/Col)_6$ (d-f). [53]

The enzyme-assisted mineralization method, explained in detail in section 1.2.3, is another promising technique for improving the mechanical stability of the formed nanotubes. Indeed, based on the inorganic composition of the ECM of hard tissues, the incorporation of hydroxyapatite minerals into the structure can enhance its stability. For this purpose, Colaço et al. carried out a preliminary study on the biomineralization process in a confined environment by incorporating alkaline phosphatase (ALP) into a multilayer film in a porous polycarbonate (PC) membrane to form mineralized nanotubes.
They first experimentally measured the isoelectric point of the enzyme and obtained a pH value close to 5. They therefore decided to study the LbL assembly and the subsequent mineralization at different conditions: pH 7,4 (RT), pH 7,4 (37°C) and pH 9 (RT). At these pH values, ALP has negatively-charged residues and is therefore used as a polyanion to adsorb onto the poly(allylamine hydrochloride) (PAH) polycation. After the formation of five $(PAH/ALP)_5$ bilayers in the pores of the PC membrane, the structure was mineralized by incubating the template in a solution containing $Ca^{2+}$ ions and $\alpha$-glycerol phosphate.
Their results showed the influence of several parameters on the biomineralization in a confined environment, such as physiological conditions and diameter of the template pores. Indeed, the nanotubes formed in the membrane with a pore size of 500 nm had CaP particles distributed all along the structure. This proved the successful mineralization of nanotubes for the three conditions studied. However, in 200 nm pore size membranes, only mineralization at pH 7.4 and 37°C for 48h resulted in nanotubes uniformly filled with the mineral particles and with high mechanical stability.
In addition, they demonstrated the influence of pore size on the morphology and crystallinity of the CaP particles in the nanotubes formed. Indeed, as shown on the TEM images in Figure 1.16(a), LbL assembly and mineralization in a membrane with a pore diameter of 200 nm resulted in nanowires densely filled with crystalline hydroxyapatite platelets, whereas in a 500 nm pore size template, hollow tubes made of amorphous particles were obtained. In this way, they were able to demonstrate that the confined environment had an impact on the crystallinity of the mineral phase.
A preliminary study on LbL assembly and mineralization of PAH and ALP in a PC membrane with in-

tersected nanopores showed promising results on the production of a mineralized network of intersected nanotubes. This result is shown in Figure 1.16(b).
To conclude, the study of Colaço et al. demonstrated the successful enzymatic-induced mineralization in a confined environment leading to the formation of nanotubes. According to their result, the optimal physiological conditions for the construction of LbL multilayers of PAH and ALP followed by mineralization were pH 7.4 and 37°C. These promising results on the formation of tubes with good mechanical stability pave the way for the formation of mineralized nanotubes composed of ECM-derived macromolecules. [37]

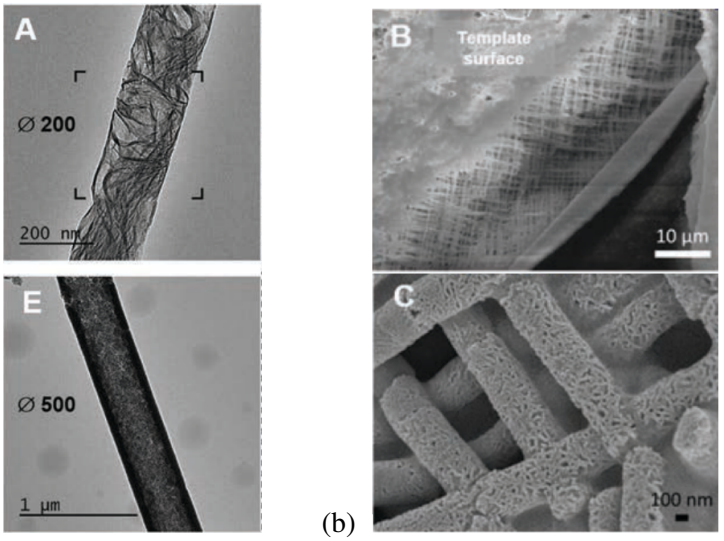


(a) (b)

Figure 1.16: (a) TEM images of nanotube built in a 200 nm (A) and 500 nm (E) pore size membrane at pH 7.4 and 37°C. (b) SEM images of a mineralized intersected nanotube network of $(PAH/ALP)_5$ multilayers viewed from the side (B) and at high magnification (C). [37]

In the continuation of their previous study, Colaço et al. improved the control of the biomineralization of nanostructures and particularly the nucleation and growth of calcium phosphate particles. Indeed, to enhance the previously obtained ALP-mediated biomineralized nanotubes, they added type I collagen (Col) and hyaluronic acid (HA) in the LbL multilayers assembling in the membrane templates. Given its crucial role in hard tissue mineralization, collagen is an ideal chemical environment for enzymatic-induced mineralization. As demonstrated in their first study, the confinement in the membrane nanopores is also favourable for the control of the crystallinity of the mineral phase.
First, in order to have a successful layer-by-layer assembly of the different biomacromolecules, they evaluated their isoelectric point. For collagen and hyaluronic acid, they obtained similar results to those of Lefèvre et al. defining an optimal pH below 6 for the Col/HA assembly.[53] As in their previous study, they suggested that ALP was negative at physiological pH and could therefore assemble with positively-charged PAH at this pH value. Since the Col/HA multilayer is not stable at pH 7.4, the assembly of these biomacromolecules was first carried out at pH 4.5 followed by cross-linking with EDC and NHS to obtain a stable layer. The PAH/ALP bilayers were then assembled at physiological pH.
They firstly studied the assembly on planar surfaces to confirm the feasibility of the LbL assembly of the $(Col/HA)_3(PAH/ALP)_5$ system followed by mineralization. The enzyme-assisted mineralization was performed under physiological conditions (pH 7.4, 37°C) for 48h by incubation in the enzyme substrate, i.e. a solution of $Ca^{2+}$ ions and $\alpha$-glycerol phosphate. The authors were able to highlight the influence of the $(Col/HA)_3$ multilayer on the nucleation and growth of the CaP particles. Indeed, isolated particles were observed in the case of $(PAH/ALP)_5$ multilayers whereas $(Col/HA)_3(PAH/ALP)_5$ multilayers led to the formation of large particles with a high surface coverage. This can be explained by the fact that collagen modifies the surface energy of the solid with which it interacts, leading to the formation of crystalline phases during mineralization.

The assembly of this multilayer systems as well as the subsequent mineralization was then performed in the pores of PC membranes, with pore sizes of 200 and 500 nm. The mineralized $(PAH/ALP)_5$ multilayers gave similar results to their previous study, i.e. nanowires filled with platelet-like HAp structures for 200 nm pore size and nanotubes composed of amorphous calcium phosphate in the case of 500 nm pore size. Concerning the mineralized $(Col/HA)_3(PAH/ALP)_5$ multilayers, similar structures to the $(PAH/ALP)_5$ case were obtained in the 200 nm pore size. However, the nanostructures formed in the 500 nm pores were nanowires composed of platelet-like but also fibrillar structures. These different results observed with TEM micrographs are shown in Figure 1.17. This highlighted the significant role of collagen on the mineralization process in a confined environment. [6]

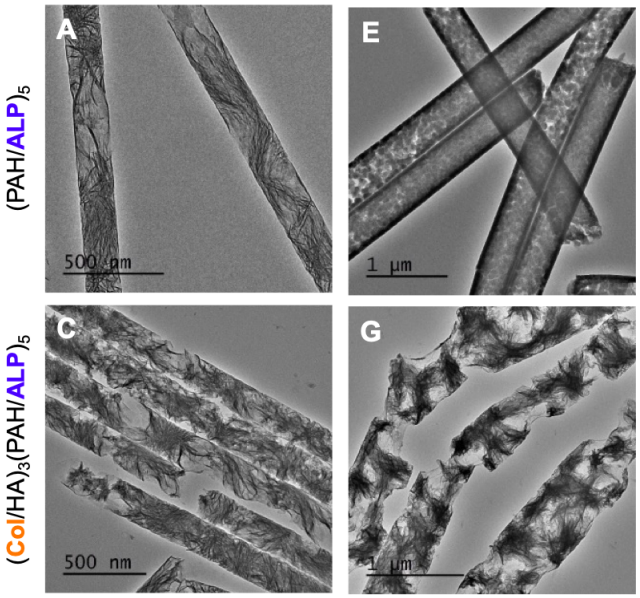


Figure 1.17: TEM images showing the morphology and crystalline structure of mineralized nano-objects composed of $(PAH/ALP)_5$ (A,E) and $(Col/HA)_3(PAH/ALP)_5$ (C,G) multilayers formed in a PC membrane template of pore diameter of 200 nm (A,C) and 500 nm (E,G).[6]

In addition, low-magnification TEM micrographs revealed that the morphology of the nanotubes composed of mineralized $(PAH/ALP)_5$ multilayers was like straight lines and often broken, suggesting that the structures were rather fragile, as shown in Figure 1.18B. A similar morphology was observed for $(Col/HA)_3(PAH/ALP)_5$ tubes formed in 200 nm pores, although the mineralized nano-objects formed in 500 nm pores had a more bent morphology, visible in figure 1.18D. This suggested a high flexibility of the nanotubes and thus better mechanical stability. A higher-magnification TEM image, shown in figure 1.18F, suggested that the origin of this flexibility was due to fibrillar collagen nanostructures bonded together with HAp minerals. [6]

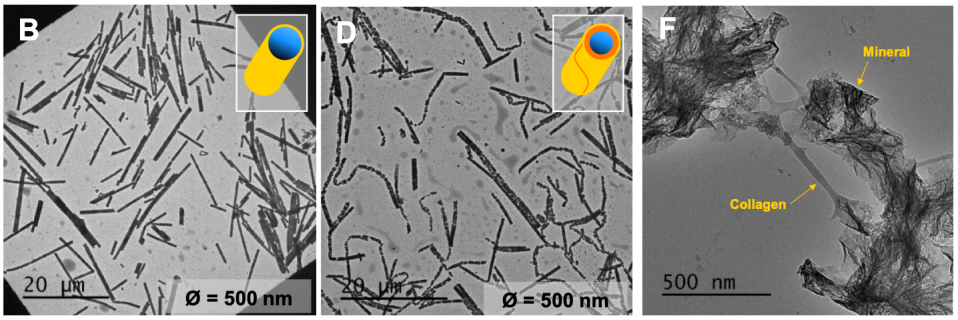


Figure 1.18: Morphologies of mineralized nano-objects composed of $(PAH/ALP)_5$ (B) and $(Col/HA)_3(PAH/ALP)_5$ (D,F) multilayers formed in a PC template of 500 nm pore size recorded from low-magnification (B,D) and high-magnification (F) TEM micrographs. [6]

Finally, the complete morphology as well as the mechanical stability of the nanostructures were studied by SEM. As shown in Figure 1.19B, the mineralized $(PAH/ALP)_5$ nanotubes were well defined but most of them were broken with an unstable structure. In contrast, the mineralized $(Col/HA)_3(PAH/ALP)_5$ nanostructures had different characteristics. Indeed, as visible in Figure 1.19F, the structure was preserved with a significantly larger length, reaching a value similar to the thickness of the template membrane. In addition, the topology of their surface was rough with a high degree of porosity. These characteristics were more pronounced for the structures formed in the 500 nm pores compared to the 200 nm ones probably due to a higher adsorption of collagen in the 500 nm nanopores. As a result, these observations proved once again that the incorporation of $(Col/HA)_3$ multilayers allows obtaining nanostructures with better mechanical stability.
The authors demonstrated the successful formation of mineralized nanotubes formed from collagen, hyaluronic acid and alkaline phosphatase. They highlighted the important role of collagen in the control of crystallinity as it allows the formation of crystalline phases of HAp by enzymatic-induced mineralization, independently of the degree of confinement. Moreover, the incorporation of collagen allowed achieving interesting mechanical properties such as the increase of the flexibility of the nanotubes. [6]

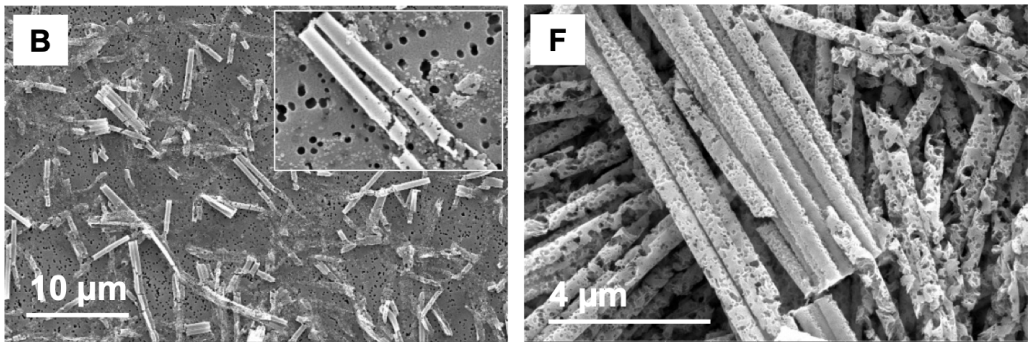


Figure 1.19: SEM images of mineralized nanotubes composed of $(PAH/ALP)_5$ (B) and $(Col/HA)_3(PAH/ALP)_5$ (F) multilayers built in a PC template of 500 nm pore size. [6]

# Chapter 2

# Materials and methods

As a reminder, the objective of this thesis is to synthesise biomineralized nanostructured biointerfaces mimicking the extracellular matrix of bones for future use in tissue engineering applications. The biointerfaces produced consist of intersected nanotubes composed of collagen (Col) and hyaluronic acid (HA) and their mechanical stability is enhanced by the formation of hydroxyapatite, induced by the enzymatic-induced mineralization technique using alkaline phosphatase (ALP). The final aim is to fine-tune a series of parameters to modulate the mechanical properties of the synthesised nanostructured biointerfaces.

These nanostructures were produced by the combination of the template synthesis, layer-by-layer assembly and enzymatic-induced mineralization techniques. To achieve this, the strategy was initially to deposit ECM-derived macromolecules, i.e. collagen, hyaluronic acid and alkaline phosphatase, by LbL assembly followed by mineralization on planar surfaces to then extend the technique into nanoporous templates. For this purpose, two types of templates were used giving rise to two different types of nanostructures: PC membrane with parallel or intersected nanopores. The influence of some parameters on the mechanical stability of the formed nanotubes was finally explored, mainly in parallel nanopores, by morphological analyses.

In this chapter, the different materials used for the formation of the nanostructures are presented, followed by the description of the experimental processes of LbL assembly and mineralization on different substrates and the characterisation techniques used.

## 2.1 Materials

Poly(allylamine hydrochloride) (PAH, Mw $\sim$ 17.5 kDa), branched polyethyleneimine (PEI, Mw $\sim$ 800 Da), poly(sodium-4-styrenesulfonate) (PSS, Mw $\sim$ 70 kDa), DL-$\alpha$-glycerol phosphate magnesium salt hydrate ($\sim$ 85%), calcium chloride ($CaCl_2$, $\geq$ 99%), alkaline phosphatase from bovine intestinal mucosa (ALP, $\geq$ 10 U/mg), alginic acid sodium salt (ALG, Mw $\sim$ 120-190 kDa), N-(3-Dimethylaminopropyl)-N'-ethylcarbodiimide hydrochloride (EDC, Mw $\sim$ 191,70 Da), N-hydroxysuccinimide (NHS, $\geq$ 97%), 4-Nitrophenyl phosphate disodium salt hexahydrate (pnpp, $\geq$ 99%) and 4-Nitrophenol (pnp, $\geq$ 99%) were purchased from Sigma-Aldrich (France). Type I collagen G from bovine calf skin (Col, 4 mg/mL) was bought from Biochrom GmbH (Germany) and sodium hyaluronate (HA, Mw $\sim$ 151-300 kDa) from Lifecore Biomedical (USA). Sodium chloride (NaCl) was obtained from Merck Millipore (France) and hydrochloride acid (HCl, 37%) from VWR (France). Dichloromethane ($CH_2Cl_2$) and sodium hydroxide anhydrous pellets (NaOH) were purchased from CARLO ERBA Reagents (France). Iron chloride ($FeCl_3$, 98%), 2-(N-morpholino)ethanesulfonic acid monohydrate (MES, 99%) and pyrrole monomer (Py, 99%) were bought from Acros (France).

Track-etched polycarbonate (PC) membranes with parallel nanopores of an average diameter of 200, 300 and 500 nm, a pore density of $10^8$ cm$^{-2}$ and a thickness of 25 $\mu$m were provided by It4ip (Belgium). For the synthesis of networks of intersected nanotubes, the PC track-etched membranes with intercon-

nected pores, also provided by It4ip (Belgium), were fabricated by exposing a 25 microns thick PC film to a two-step irradiation process: a first irradiation at two fixed angles of - 45° and + 45° with respect to the normal axis of the film plane. After rotating the PC film in plane by 90°, the second irradiation step was performed at the same fixed angular irradiation flux to finally formed a 3D nanochannel network. The diameter of the latent tracks was further enlarged by chemical etching to obtain membranes with average pore diameter of 300 nm . The pore density of these membranes was 2,8 $10^8$ $cm^{-2}$. Hydrophilic polyester (PET) membranes, used for filtration, with an average pore diameter of 1 $\mu$m, a pore density of 2.2 $10^7$ $cm^{-2}$ and a thickness of 22 $\mu$m were also provided by It4ip (Belgium).

## 2.2 Solutions preparation

All solutions were freshly prepared the day before or the day of the LbL assembly and diluted in Milli-Q water (Millipore, France). Milli-Q water used for rinsing baths after layers deposition was adjusted to pH 4; 4.5 or 7.4 with NaOH or HCl (0.1 M), depending on the composition of the deposited layers.

**Synthetic polyelectrolytes** The anchoring layer solutions, i.e. PAH or PEI and PSS, were prepared at a final concentration of 1 mg/mL each and adjusted to pH 4.5 with NaOH or HCl (0.1 M).
The solution of PAH, assembling with ALP, was prepared to reach a final concentration of 1 mg/mL and its pH was then adapted to physiological pH (7.4).

**Biopolymers** The HA and ALG solutions were prepared at a final concentration of 1 mg/mL and their pH was adjusted with HCl (0.1 M). The final pH value reached for the HA solution was 4.5 while for the ALG solution it was 4.

**Proteins** The Col solution (4mg/mL) was diluted to obtain a final concentration of 0.1 mg/mL and its pH was adjusted with NaOH (0.1 M) to reach a final value of 4.5 or 4. The ALP solution was prepared to reach a final concentration of 0.1 mg/mL and its pH is then adapted to physiological pH (7.4), paying particular attention to pH variations to avoid denaturation of the enzyme.

**Mineralization solution** The mineralization solution was prepared by dissolving $\alpha$-glycerol phosphate magnesium salt hydrate and $CaCl_2$ to reach a final concentration of 7 mM and 11.4 mM respectively. The pH of the solution was adjusted with HCl (0.1 M) to reach a final value of 7.4. The solution being poorly soluble, it is strongly stirred for at least 1 h followed by agitation at 37°C for at least 30 min.

## 2.3 Layer-by-layer assemblies and mineralization on planar surfaces

The planar surfaces on which the LbL assembly and subsequent mineralization were carried out were pieces of silicon wafers cleaned with Piranha solution ($H_2O_2$ (30%) / $H_2SO_4$ (96%, in 1:3 ratio)) and dried with $N_2$ gas flow.

**Mineralized (PAH/ALP)$_5$ multilayers** The LbL assembly of the multilayers was initially carried out by immersing the silicon wafers in PAH solution and then in ALP solution for 15 min and 30 min each. The substrates were dipped in three successive rinsing baths of Milli-Q water for 2 min each after the adsorption of each layer. Following the build-up of the five bilayers, the surfaces were incubated in the mineralization solution during 24h at 37°C. One silicon wafer was dried without the mineralization step, for further analysis of non-mineralized multilayers.
After 24h, the mineralization was stopped and the substrates were rinsed in three baths of 2 min each followed by drying with $N_2$ gas flow.

**Mineralized (Col/HA)$_3$(PAH/ALP)$_5$ multilayers** The LbL assembly was first conducted by the build-up of an anchoring layer by immersing the cleaned silicon wafers in PEI solution followed by PSS solution for 10 min each with three rinsing steps between each layer deposited.
After the construction of this anchoring bilayer, the three (Col/HA)$_3$ bilayers were built by alternatively dipping the substrates in the Col and HA solutions for 30 min and 15 min each followed by rinsing steps. The alternating immersion process with Col and HA was performed three times and the substrates were then incubated in the cross-linking solution (EDC 30 mM/NHS 50 mM) overnight under mild agitation at RT.

The day after, the substrates were rinsed in a bath of Milli-Q water for 10 min. Then, in order to build the $(PAH/ALP)_5$ multilayers followed by the mineralization step, the silicon wafers were immersed in the different solutions following the procedure described previously.

## 2.4 Layer-by-layer assemblies and mineralization in nanoporous templates

**Nanoporous templates**

Two types of nanoporous templates were used for the template synthesis method combined with the layer-by-layer assembly technique: PC membrane with parallel pores and intersected pores. The first membrane allows the formation of individual nanotubes while the second one makes it possible to build up a network of intersected nanotubes. Illustrations of the porous structures of these templates are shown in Figure 2.1 and the properties of the membranes used for the nanotubes formation are described in detail in section 2.1.

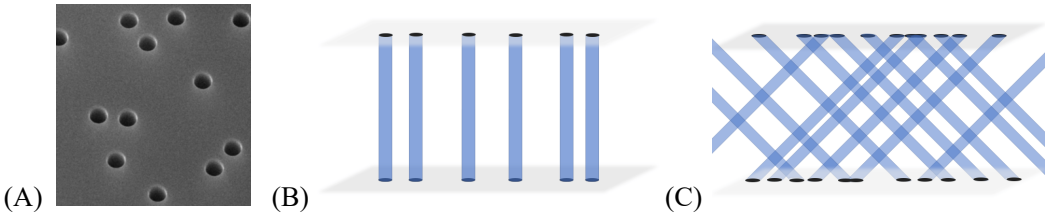


Figure 2.1: SEM image of the top view of the surface of a track-etched PC membrane (A) and schematic representation of the side view of the internal structure of a membrane with parallel straight pores (B) and intersected pores (C). [42]

To identify the exact pore structure of the PC membrane containing intersected nanopores, a replicate was produced by chemical oxidative polymerization of polypyrrole (PPy). To do this, a $\sim$12 $cm^2$ piece of the PC membrane was placed between the two compartments of a diffusion cell. The first compartment was filled with a solution of Py monomer. The solution was prepared by dissolution in a 100 mM MES buffer at pH 5.5 to reach a Py concentration of 500 mM and then filtered through silica gel before use. After 20 min, the $FeCl_3$ oxidation solution (500 mM in Milli-Q water) was added to the second compartment to induce the polymerization reaction during 5 min. The PC membrane filled with PPy was then rinsed abundantly in Milli-Q water. Its both faces were then gently rubbed to remove the PPy crust formed on the membrane surfaces. To dissolve the PC membrane and obtain the network of intersected PPy nanotubes, the membrane was immersed in dichloromethane ($CH_2Cl_2$). The obtained network was then observed by scanning electron microscopy (SEM, JSM- 7600F, Jeol) at 5 kV and the acquired images are shown in Figure 2.2.

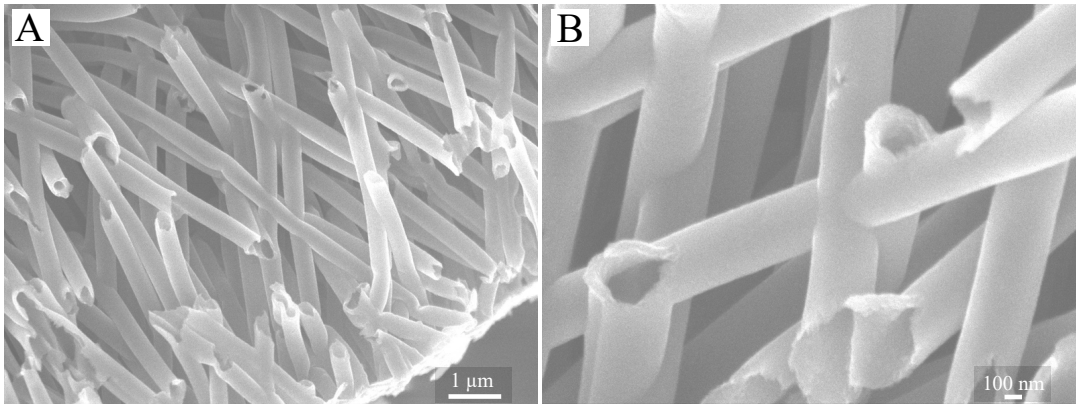


Figure 2.2: SEM images of intersected PPy nanotubes replicating the porous structure of the PC membrane with intersected nanopores. Global image of the network (A) and magnification of the intersection between the nanotubes (B).

### Different approaches

Layer-by-layer assembly and mineralization in porous templates were carried out using different approaches in order to study the influence of some parameters on nanotube properties. The main parameters that were varied were the composition of the anchoring layer ((PAH/PSS) or (PEI/PSS)), the use of hyaluronic acid (HA) or alginate (ALG) in the first bilayers and the conditions of cross-linking of these layers. The different conditions of assemblies performed in PC membranes with either parallel or intersected nanopores are listed in Table 2.1 below. Figure 2.3 shows the chemical structures of the polyelectrolytes involved in these different approaches.

Table 2.1: List of different approaches for LbL assembly and mineralization in nanoporous templates.

| | **PC membrane pores** | **Anchoring layer** | **Multilayers** | **Cross-linking** |
|---|---|---|---|---|
| 1 | Parallel (300nm) | (PAH/PSS) | $(Col/HA)_3(PAH/ALP)_5$ & $(PAH/ALP)_5$ | EDC 30mM, NHS 50mM at RT |
| 2 | Parallel with 200, 300 and 500nm pores | (PAH/PSS) | $(Col/HA)_3(PAH/ALP)_5$ & $(PAH/ALP)_5$ | EDC 30mM, NHS 50mM at RT |
| 3 | Parallel (300nm) | (PAH/PSS)<br>(PAH/PSS)<br>or (PEI/PSS) | $(Col/HA)_3(PAH/ALP)_5$ | EDC 30mM, NHS 50mM at RT<br>EDC 7.5mM, NHS 50mM at 4°C<br>EDC 30mM, NHS 50mM at 4°C |
| 4 | Parallel (300nm) | (PAH/PSS)<br>or (PEI/PSS) | $(Col/ALG)_3(PAH/ALP)_5$ | EDC 30mM, NHS 50mM at RT<br>EDC 100mM, NHS 50mM at 4°C |
| 5 | Intersected (300nm) | (PAH/PSS) | $(Col/HA)_3(PAH/ALP)_5$ & $(PAH/ALP)_5$ | EDC 30mM, NHS 50mM at RT |

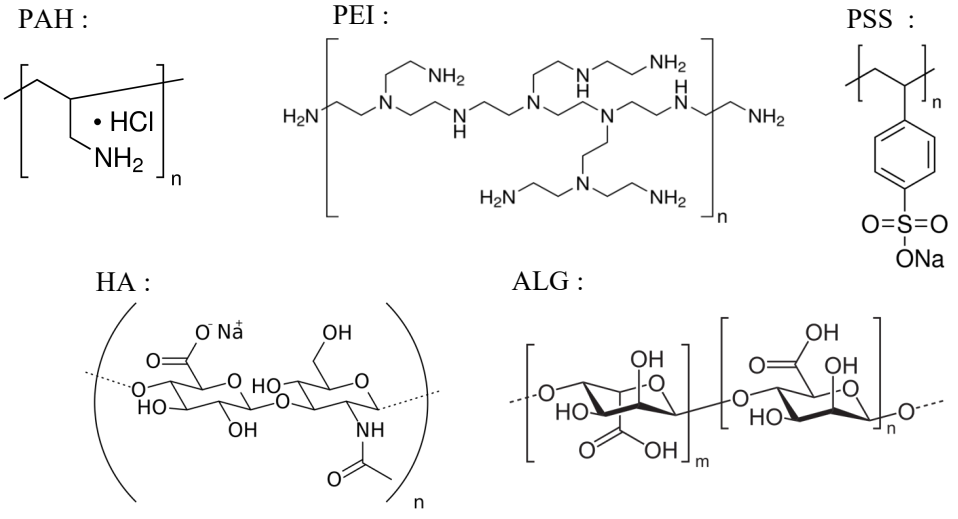


Figure 2.3: Chemical structure of the polyelectrolytes used in this study : poly(allylamine hydrochloride) (PAH), polyethyleneimine (PEI), poly(styrene sulfonate) (PSS), hyaluronic acid (HA) and alginate (ALG).

### LbL assemblies and mineralization in nanoporous templates

The process of LbL assembly and mineralization in the nanoporous templates were similar for the different approaches studied (listed in Table 2.1).

**Mineralized $(PAH/ALP)_5$ multilayers** The LbL assembly in nanoporous templates was carried out at 37°C by alternatively immersing a piece of PC membrane ($\sim$1 cm $\times$ 1 cm) in PAH and ALP solutions following the same process as for planar surfaces (section 2.3), except the incubation time that was

increased to 30 min and 1 h respectively. Following the formation of the five bilayers, both faces of the membranes were decrusted with a cotton swab impregnated with a solution of NaCl 3 M (pH 12) and then abundantly rinsed in two water baths at pH 7.4. The membranes were then incubated in the mineralization solution for 48 h at 37°C. A quarter of the PC templates was cut, without the mineralization step, and immersed in the rinsing solution (Milli-Q water at pH 7.4) to be kept at 4°C for further analysis of the enzymatic activity, described in section 2.5.
After 48 h, the mineralization was stopped and the PC templates were rinsed in two water baths at pH 7.4 followed by drying with $N_2$ gas flow.

**Mineralized (Col/HA)$_3$(PAH/ALP)$_5$ or (Col/ALG)$_3$(PAH/ALP)$_5$ multilayers** The LbL assembly was first conducted by the build-up of an anchoring layer composed of (PAH/PSS) or (PEI/PSS) bilayers by immersing the PC membranes in the polyanion and polycation solutions for 30 min each, followed by rinsing steps. The three (Col/HA)$_3$ or (Col/ALG)$_3$ bilayers were then build-up following the same process described for planar surfaces (section 2.3) with immersion times of 1 h, for Col, and 30 min, for HA and ALG, and rinsed at pH 4.5 or 4. Before incubating in the cross-linking solution (EDC 7.5; 30 or 100 mM/NHS 50 mM) at RT or 4°C overnight, both faces of the membranes were decrusted with the solution of NaCl 3 M (pH 12).
The day after, the templates were rinsed two times in Milli-Q water at pH 7.4 for 10 min each and subsequently decrusted. Then, for the building of the (PAH/ALP)$_5$ multilayers followed by the mineralization step, the PC membranes were immersed in the different solutions following the procedure described above.

#### Collect of nanotubes

In order to release the nanotubes formed in the PC membrane, a small piece of the template ($\sim$0.25 cm$^2$) was immersed in a beaker containing 3 mL of dichloromethane ($CH_2Cl_2$) allowing the dissolution of the membrane. The nanotubes were then collected using a pipette and filtered under vacuum through a PET filter, followed by the pouring of 10 mL of fresh dichloromethane to remove the residual PC.

## 2.5 Characterization techniques

#### Morphology

The morphology of the synthesized nanotubes as well as the mineralized layers on planar surfaces were studied using scanning electron microscopy (SEM, FEI Quanta FEC 250) equipped with an Everhart-Thornley detector, at an acceleration voltage of 20 kV. Samples were metalized by platinum sputtering to avoid changing effects and obtain a better image contrast.

The surface of the silicon wafers was also analyzed by optical microscopy (Olympus BX51M) at different magnifications ($\times$10 and $\times$20) in order to study each step of the LbL assembly and mineralization on planar surfaces.

#### Elemental composition

The elemental composition of the formed nanotubes was determined by energy-dispersive X-ray spectroscopy (EDX) measurements. For this purpose, the sample was placed in the chamber of the scanning electron microscope which is equipped with an energy-dispersive X-ray spectrometer. The acquisition was performed in backscatter mode following the diffraction of the X-rays by a monochromator crystal (Si or Ge). The measured backscattered electrons therefore allowed the identification and quantification of the elements in the sample. The EDX spectrum was then plotted with OriginPro software. [54]

#### Chemical composition

The determination of the chemical composition of the mineralized multilayers formed on the surface of the silicon wafers was performed using Fourier-transform infrared (FTIR) spectroscopy. The analyses were performed on a Bruker Vertex 80 spectrometer equipped with a horizontal reflection ATR accessory

including a diamond crystal. The spectrometer was equipped with a nitrogen cooled MCT detector. Silicon wafers were placed face down on the crystal, and a force was applied with a pressure tip. The background was recorded under ambient conditions without any substrate pressed against the crystal. For each spectrum, 250 scans were collected with a nominal resolution of 4 $cm^{-1}$.

**Enzymatic activity**

The catalytic activity of alkaline phosphatase (ALP) immobilised in PC membranes was measured with a UV-visible spectrophotometer (Biochrom Libra S60) as a function of time at 410 nm and 37°C . The production of 4-nitrophenol (pnp) was measured in the presence of the 4-nitrophenyl phosphate (pnpp) substrate, as ALP catalyses the hydrolysis reaction of pnpp as shown in Figure 2.4.

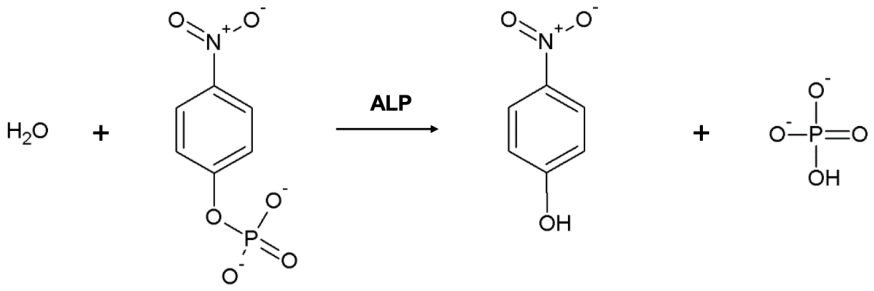


Figure 2.4: Hydrolysis reaction of 4-nitrophenyl phosphate (pnpp) catalysed by alkaline phosphatase (ALP) releasing 4-nitrophenol (pnp).

The measurement of absorbance versus time was performed by placing a piece of PC membrane ($\sim$0.6 $\times$ 0.6 $cm^2$), containing the multilayers with ALP, in a plastic cuvette (10 mm optical path length) filled with 2 mL of pnpp solution. The pnpp substrate solution was prepared by dissolution in Milli-Q water to reach a final concentration of 7 mM. The pH of the solution was adjusted with HCl (0.1M) to a value of 7.4.
In order to relate the absorbance measured by the spectrophotometer to the pnp concentration, a calibration curve was defined. To do this, the absorbance of pnp at different concentrations, i.e. at 0.01, 0.02, 0.03, 0.05, 0.1 and 0.15 mM, was measured at pH 7.4 and 37°C. The curve obtained is shown in Figure 2.5.

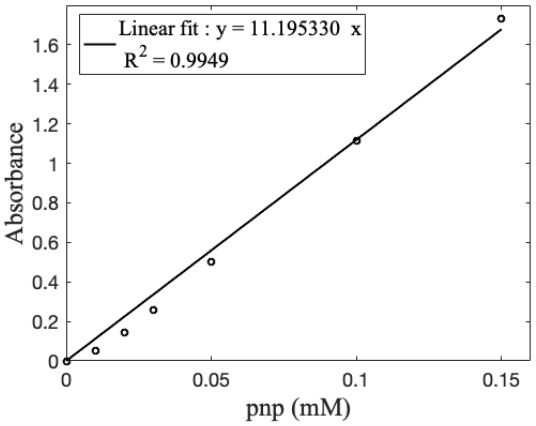


Figure 2.5: Calibration curve relating absorbance to 4-nitrophenol (pnp) concentration.

According to Lambert-Beer law :

$$A = \epsilon \cdot l \cdot c$$

where $A$ is the absorbance, $\epsilon$ is the molar extinction coefficient ($mM^{-1}.cm^{-1}$), $l$ is the optical path length (cm) and $c$ is the concentration (mM). By using the calibration curve, the molar extinction coefficient can

be determined ($\epsilon$ = 11.195), and was therefore used to convert the absorbance into pnp concentration.

For the comparison of the enzymatic activity in different PC membranes, the measured activity was normalised by the surface area of the membrane pores.
For a membrane with parallel straight pores, the surface area of one pore is defined by the relation :

$$S^p_{pore} = 2\pi \cdot r \cdot t$$

with $S^p_{pore}$ the surface of one pore, r the radius of the pore and t the thickness of the membrane. The surface area of all pores is then obtained by multiplying the surface area of one pore by the number of pores defined by the relation :

$$N = s \cdot d$$

with N the number of pores, s the surface area of the membrane and d the pore density. The surface area of all parallel pores ($S^p_{all}$) is therefore given by the relation :

$$S^p_{all} = S^p_{pore} \cdot N$$

Following the same reasoning, the surface area of all pores of a PC membrane with intersected nanopores ($S^i_{all}$), given that the pores are oriented at 45° to the membrane surface, is determined by the relation :

$$S^i_{all} = 2\pi \cdot r \cdot \frac{t}{sin(45)} \cdot s \cdot d$$

.

# Chapter 3

# Results and discussion

This chapter presents the main results obtained for the different steps leading to the formation of biomineralized nanostructured biointerfaces mimicking the extracellular matrix. A discussion that aims at explaining these different results is also proposed.
These nanostructures are synthesised by combining the techniques of template synthesis, layer-by-layer assembly and enzymatic-induced mineralization. In a first step, the build-up of multilayers containing ECM-derived macromolecules and the ALP enzyme followed by mineralization is investigated on planar surfaces. In a second step, the layer-by-layer assembly and subsequent mineralization are studied in nanoporous templates. For this purpose, two types of templates are used giving rise to two different types of nanostructures: PC membrane with parallel nanopores, forming individual nanotubes and PC membrane with intersected nanopores, resulting in a network of intersected nanotubes. The latter structure is the most promising due to its three-dimensional network mimicking the structure of the extracellular matrix.

## 3.1 LbL assemblies and mineralization on planar surfaces

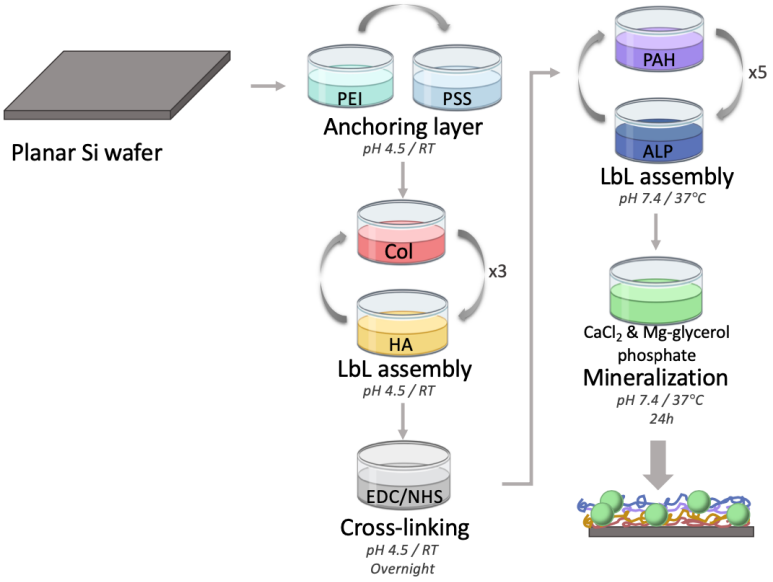


Figure 3.1: Schematic representation of the strategy used for the formation of mineralized $(Col/HA)_3(PAH/ALP)_5$ multilayers on a planar silicon wafer.

In order to confirm and understand the assembly of collagen with hyaluronic acid followed by the incorporation of multilayers containing alkaline phosphatase, layer-by-layer assembly was carried out on planar surfaces, more precisely on silicon wafers. The enzymatic-induced mineralization by ALP in the presence of calcium phosphate precursors was also investigated.

For this purpose, positively-charged collagen at pH 4.5 was adsorbed on negatively-charged PSS layer, the top layer of the anchoring film deposited on the silicon wafer. Subsequently, hyaluronic acid, being negatively-charged at this pH value, was deposited onto the first collagen layer. By repeating this process, three $(Col/HA)_3$ bilayers were built on the planar surface. The pH values of 4.5 were chosen to facilitate the electrostatic interactions between collagen and hyaluronic acid, being below the isoelectric point of Col (between 6 and 7) and above the pKa of HA (below 3), as shown previously by electrophoretic mobility measurement. [6, 53] To stabilise the multilayers and avoid their destruction when the pH value was increased to 7.4 for the second LbL assembly of $(PAH/ALP)_5$, cross-linking with EDC and NHS was performed overnight at room temperature. Afterwards, five bilayers of PAH and ALP, positively- and negatively-charged at physiological pH, were deposited on the $(Col/HA)_3$ layers. To induce mineralization, the surface was placed in a solution containing $CaCl_2$ and Mg-glycerol phosphate at 37°C during 24h. The purpose is to induce the nucleation and growth of calcium phosphate (CaP) particles in the built film. The different steps and the main conditions for the LbL assembly of $(Col/HA)_3(PAH/ALP)_5$ followed by mineralization are schematically illustrated in Figure 3.1.

To determine whether the LbL assembly and mineralization have been successfully completed, the $(PAH/ALP)_5$ and $(Col/HA)_3(PAH/ALP)_5$ multilayers formed on the silicon wafer were studied by optical microscopy before and after mineralization. The results obtained are shown in Figure 3.2. Firstly, the images of the non-mineralized surfaces highlight the difference between those containing or not the $(Col/HA)_3$ multilayers (Figure 3.2A and C). Indeed, in Figure 3.2C, fibrillar nanostructures are clearly visible, indicating a successful assembly of collagen-containing multilayers. Secondly, the images of the mineralized surfaces show the formation of mineral particles in both cases (Figure 3.2B and D). This suggests that the ALP embedded in the multilayers remained active and that its catalytic activity led to the formation of mineral. It also appears that the mineralization is more pronounced on the surface containing the $(Col/HA)_3(PAH/ALP)_5$ multilayers, indicating that collagen and hyaluronic acid have an influence on the mineralization process.

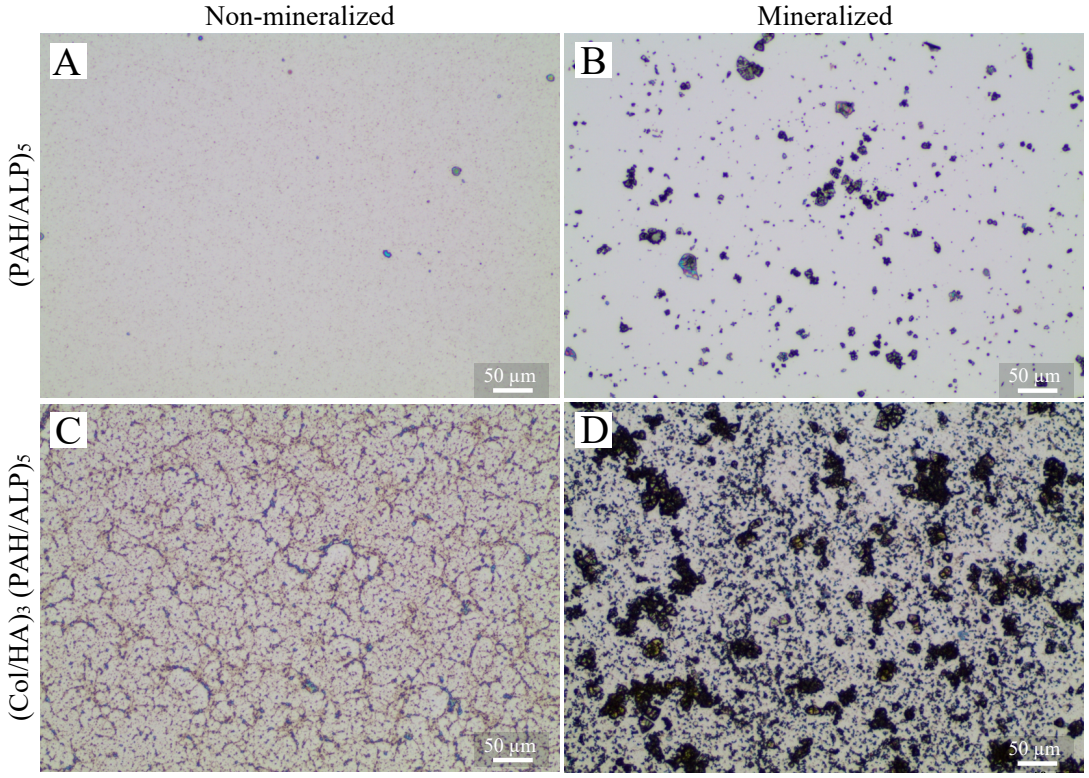


Figure 3.2: Optical microscope images recorded on silicon wafers after the build-up of $(PAH/ALP)_5$ (A,B) and $(Col/HA)_3(PAH/ALP)_5$ (C,D) multilayers before (A,C) and after (B,D) mineralization at 37°C during 24h.

More direct evidences regarding the topography of the mineralized layer are provided by scanning electron microscopy (SEM), shown in Figure 3.3. The surface covered by the $(PAH/ALP)_5$ multilayers (Figure 3.3A) contains a few isolated CaP particles whereas the mineral is more developed with a higher surface coverage on the $(Col/HA)_3(PAH/ALP)_5$ multilayers (Figure 3.3B). This confirms the findings from the optical microscope images of the mineralized surfaces. SEM images at higher magnification highlight the differences between the two types of mineralized multilayers on the surfaces, visible in Figures 3.3C and D. Indeed, the mineralized $(Col/HA)_3(PAH/ALP)_5$ multilayers contain small aggregated particles and also larger spheres of a few micrometres (Figure 3.3D). Moreover, collagen fibres can be distinguished on the SEM image, indicated with arrows in Figure 3.3D, which is consistent with the optical microscope results. Concerning the surface containing mineralized $(PAH/ALP)_5$ multilayers (Figure 3.3C), only isolated large particles of a few micrometers are formed.

The different results of the morphology analyses show the successful formation of multilayers of collagen, hyaluronic acid and alkaline phosphatase on silicon wafers, indicating that the conditions used for the LbL assembly are appropriate. Moreover, the formation of mineralized particles indicates that ALP remains active when immobilized in the multilayers. Finally, it was found that the presence of the $(Col/HA)_3$ multilayer induces a more pronounced mineralization.

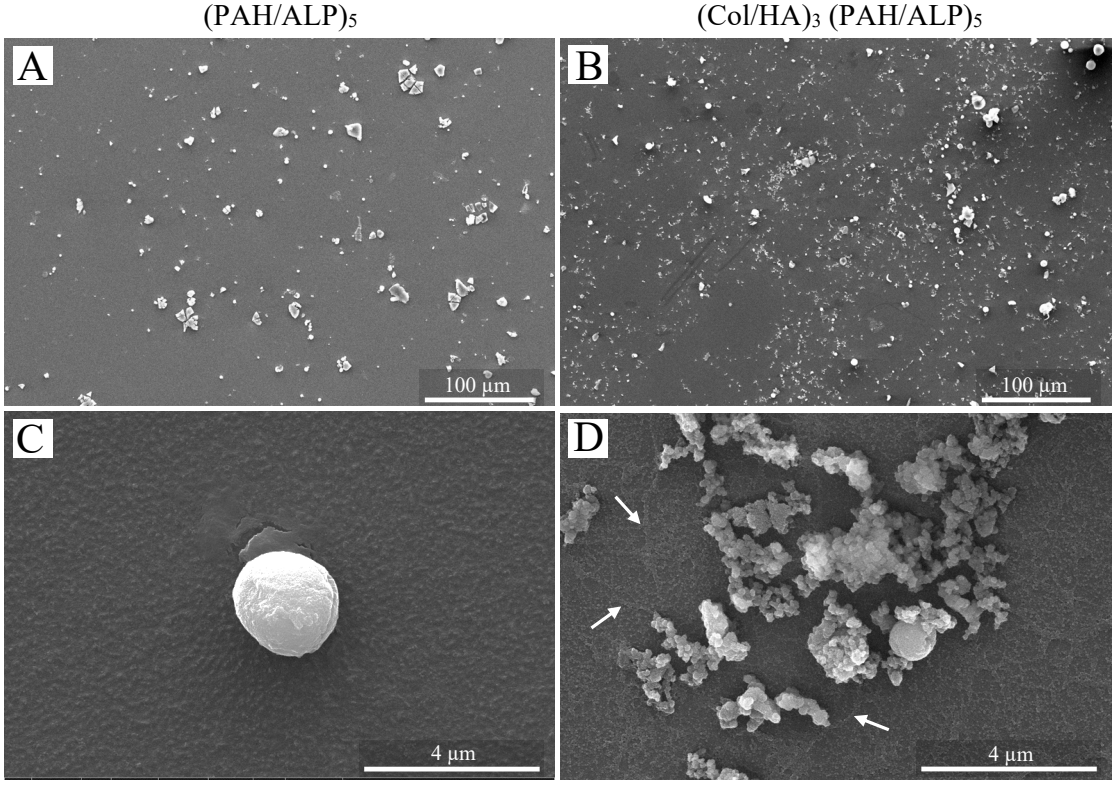


Figure 3.3: SEM images recorded on silicon wafers after the build-up of $(PAH/ALP)_5$ (A,C) and $(Col/HA)_3(PAH/ALP)_5$ (B,D) multilayers and subsequent mineralization at 37°C during 24h. Low magnification images show an overall view of the particle distribution (A,B) and a higher magnification exposes the mineral phase (C,D), arrows indicate mineralized collagen fibres.

In a previous study, Colaço et al. showed the influence of collagen on the control of the crystallinity of the CaP phase in a confined environment. Indeed, they demonstrated the formation of crystalline phases of hydroxyapatite by enzymatic-induced mineralization, independently of the degree of confinement. [6] As the pivotal role of collagen on the mineralization process has been demonstrated on planar surfaces, its particular influence on crystallinity and the chemical composition of the mineral formed were then studied. For this purpose, the silicon wafers containing the mineralized $(PAH/ALP)_5$ and

$(Col/HA)_3(PAH/ALP)_5$ multilayers were studied by infrared analysis. The resulting ATR spectra are shown in Figure 3.4A and B respectively. It appears that the vibrational fingerprints in the 900-1200 $cm^{-1}$ region are relatively similar in the two cases studied. The two main bands observed correspond to $\nu_3(PO_4^{-3})$ and $\nu_1(PO_4^{-3})$ respectively, confirming the presence of CaP compounds. This leads to the conclusion that the particles observed in the SEM analyses are indeed calcium phosphate. Secondly, the shape of the spectra suggests the formation of poorly crystalline/amorphous CaP phases in both cases studied. These results are indeed similar to the ones observed by Colaço et al. in a study on the crystallization of CaP compounds in the absence of collagen on planar surfaces, linking the shape of the IR spectrum to selected area diffraction (SAED) patterns. [37]

In conclusion, the results of the infrared analyses highlight the formation of CaP compounds on the planar surfaces, therefore confirming the successful mineralization of the $(PAH/ALP)_5$ and $(Col/HA)_3$ $(PAH/ALP)_5$ multilayers. In addition, it appears that the Col/HA based bilayers do not have a significant effect on the crystallinity of the CaP phase on planar surfaces, which seems to be poorly crystalline/amorphous in both cases studied.

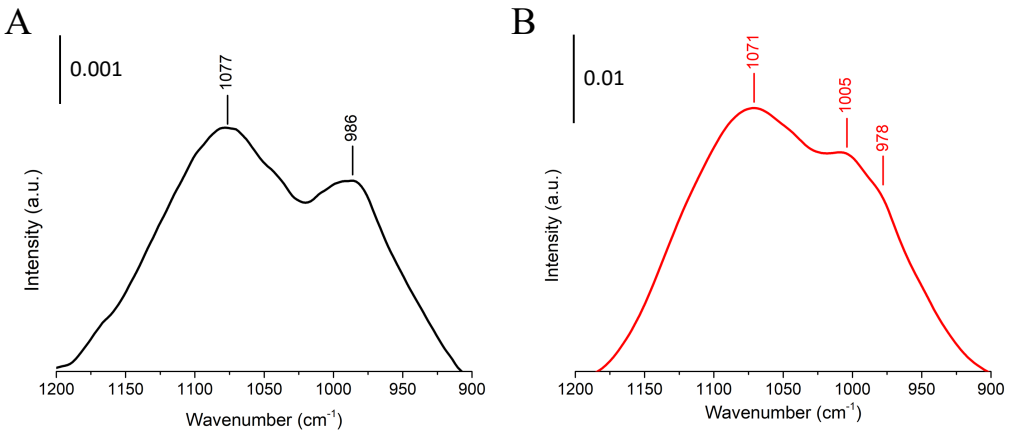


Figure 3.4: ATR spectra identifying the chemical composition of the mineralized $(PAH/ALP)_5$ (A) and $(Col/HA)_3(PAH/ALP)_5$ (B) multilayers built on silicon wafers.

## 3.2 LbL assemblies and mineralization in parallel nanopores

Given the promising results obtained on planar surfaces, the assembly of collagen, hyaluronic acid and alkaline phosphatase multilayers followed by mineralization was studied in porous templates. The LbL assembly was first performed in PC membranes with parallel pores since the formation of individual nanotubes is more straightforward and their collection and analysis are simpler.
In the first instance, mineralized $(Col/HA)_3(PAH/ALP)_5$ multilayers were built in the pores of the membrane with similar steps and conditions as those used in the case of planar surfaces. Then, the influence of a set of parameters was investigated with the aim of improving the complete formation and the mechanical strength of the individual nanotubes. Therefore, the influence of confinement on tube formation was explored using PC membranes with different pore sizes. In addition, the conditions of cross-linking of the $(Col/HA)_3$ multilayers were varied. Finally, the replacement of hyaluronic acid (HA) by alginate (ALG), an anionic polysaccharide produced by brown seaweed and extensively used in tissue engineering, was studied.
As a reminder, the main steps leading to the formation of the $(Col/HA)_3(PAH/ALP)_5$ or $(Col/ALG)_3(PAH/ALP)_5$ multilayers followed by mineralization are the following: an anchoring layer was first deposited in order to subsequently build the $(Col/HA)_3$ or $(Col/ALG)_3$ multilayers which were then stabilised by cross-linking. These steps were followed by the build-up of five bilayers $(PAH/ALP)_5$ and the subsequent enzymatic-induced mineralization by incubating in the enzyme substrate solution. Finally, the dissolution of the PC membrane with dichloromethane ($CH_2Cl_2$) results in the release of individual nanotubes. These different steps and the main conditions for the LbL assembly in the parallel pores of the template membrane are illustrated in Figure 3.5, the process is similar for the different parameters studied.

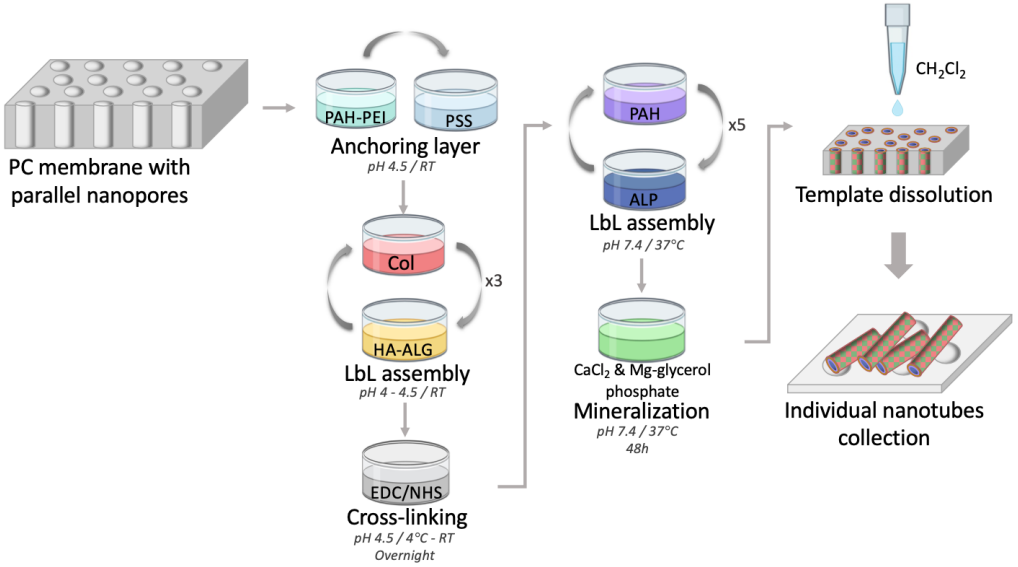


Figure 3.5: Schematic representation of the strategy used for the formation of mineralized $(Col/HA)_3(PAH/ALP)_5$ or $(Col/ALG)_3(PAH/ALP)_5$ multilayers in a PC membrane with parallel nanopores.

### 3.2.1 Formation and mineralization of $(Col/HA)_3(PAH/ALP)_5$ individual nanotubes

Based on the previous results obtained on planar surfaces, mineralized multilayers of similar composition were formed in the PC membrane pores of 300 nm diameter to obtain nanotubes with the desired properties, i.e. composed of ECM-derived macromolecules and biomineralized for achieving good mechanical strength. The conditions defined for the LbL assembly of $(Col/HA)_3(PAH/ALP)_5$ are similar to those used for planar surfaces. The major difference being the incubation time in each solution that has been increased because of the possible diffusion constraints of (bio)macromolecules into nanopores. In addition, a step of PC membrane dissolution was added to collect the formed nanotubes on a PET membrane and to be able to analyse them afterwards.

To investigate whether alkaline phosphatase remains active when embedded in the membrane pores, the enzyme activity was measured over time. For this purpose, the amount of 4-nitrophenol (pnp) produced in the presence of 4-nitrophenyl phosphate (pnpp) was recorded by UV-visible spectrophotometer at 37°C during 20 min by agitating the pnpp solution every 5 minutes. In this way, a graph of absorbance versus time was recorded. The measurement was carried out on two types of samples: a PC membrane in which $(PAH/ALP)_5$ multilayers were built and another one containing the $(Col/HA)_3(PAH/ALP)_5$ multilayers and was measured before mineralization rapidly after the assembly of the multilayers. The absorbance versus time curves obtained for these samples are shown in Figure 3.6A (fresh).

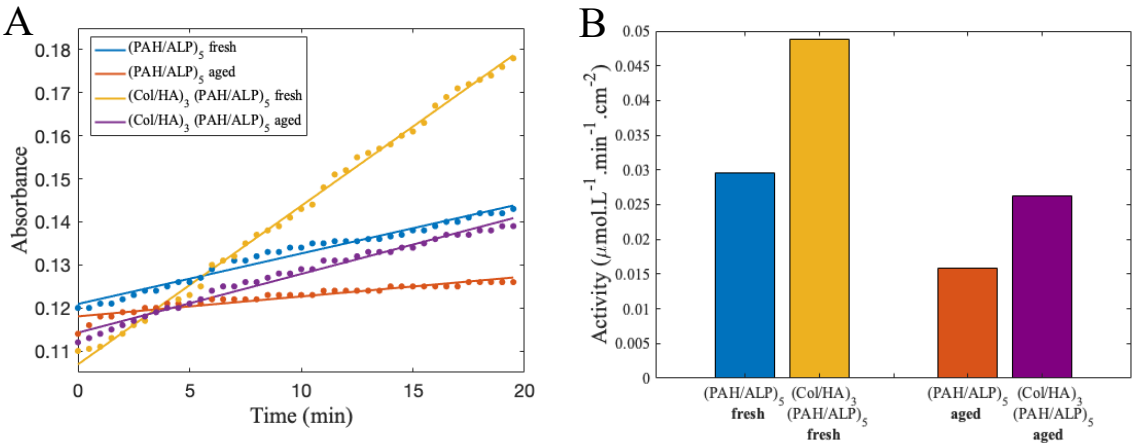


Figure 3.6: ALP activity in $(PAH/ALP)_5$ (blue and orange) and $(Col/HA)_3(PAH/ALP)_5$ (yellow and purple) multilayers built in PC membranes with parallel pores, measured rapidly after the assembly (fresh) and after 12 days (aged). (A) Evolution of the absorbance versus time due to the production of pnp, measured by UV-visible spectrophotometer at 410 nm and 37°C. (B) Histogram of enzyme activity computed from pnp concentration versus time.

The enzymatic activity of ALP (in $\mu$mol.L$^{-1}$.min$^{-1}$), corresponding to the initial rate of pnp production, was determined by converting the absorbance measured into pnp concentration and taking the slope of the linear regression line. In order to be able to compare the activities obtained, the measured values were normalised by the surface area of the membrane pores, as the membrane pieces used for the different analyses were not exactly of the same size. The enzymatic activity values, in $\mu$mol.L$^{-1}$.min$^{-1}$.cm$^{-2}$, obtained for each sample are shown in the form of a histogram in Figure 3.6B.
By comparing the enzyme activities measured shortly after LbL assembly (Figure 3.6B, fresh), it appears that the activity is about 39% higher in the case of multilayers containing the three $(Col/HA)_3$ bilayers. This may be due to the fact that the $(Col/HA)_3$ multilayer allows more ALP enzymes to be trapped, thus explaining that a higher activity is produced. Another explanation could be that Col and/or HA enhance the enzymatic activity when interacting with ALP. This hypothesis will be investigated hereafter (see section 3.4).

Afterwards, to verify whether the enzymatic activity is preserved over time, the measurement was carried out 12 days after the build-up of the $(PAH/ALP)_5$ or $(Col/HA)_3(PAH/ALP)_5$ multilayers by storing the membranes at 4°C in the rinsing solution (Milli-Q water at pH 7.4). The graphs of absorbance versus time obtained by UV-visible spectrophotometer measurements are shown in Figure 3.6A (aged). As with the freshly measured activities, the enzymatic activities normalised by the surface area of the membrane pores were calculated and can be seen in the histogram in Figure 3.6B (aged). This graph shows an increase in activity of about 40% in the presence of multilayer $(Col/HA)_3$, similar to the result obtained when activity was measured rapidly after LbL assembly (fresh). Furthermore, it appears that the activity is significantly lower, by about 46% for both systems, when measured after 12 days compared to when it is monitored rapidly after the deposition of the multilayers. This could be explained in two ways, the first being that ALP becomes inactive over time, and the second being that a non-negligible amount of enzyme is desorbed from the multilayers during storage of the membranes, both phenomena are also

possible.

The hypothesis of ALP desorption from the multilayers formed in the PC membrane when stored for a few days at 4°C was investigated by measuring the activity in the supernatant containing the stored membranes. This assumption could explain the decrease in enzyme activity when recorded after 12 days. To this end, 1.8 mL of the supernatant was poured into a plastic cuvette and 200 $\mu L$ of pnpp (70 mM) was then added to achieve a final pnpp concentration of 7 mM. The absorbance versus time was measured during 15 min by UV-visible spectrophotometer at 410 nm and 37°C. The graphs of absorbance versus time obtained for the supernatant that stored the membranes containing the $(PAH/ALP)_5$ multilayers and the one with the membranes filled with the $(Col/HA)_3(PAH/ALP)_5$ multilayers are shown in Figure 3.7. These graphs reveal activity in solution, which can be explained by the presence of the ALP enzyme in the supernatant. This means that the enzyme has indeed desorbed from the multilayers when the membranes were kept in solution. These results therefore confirm that the decrease in enzyme activity observed after 12 days is partly due to the hypothesis stated. However, further experiments should be carried out to determine whether other factors are involved in this decrease in enzymatic activity.

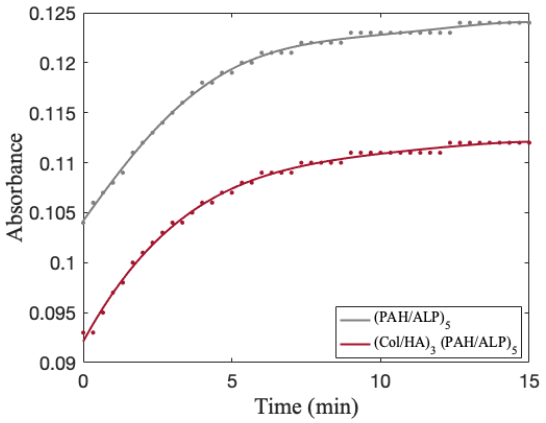


Figure 3.7: Amount of pnp produced in the supernatant storing PC membranes containing $(PAH/ALP)_5$ (grey) and $(Col/HA)_3(PAH/ALP)_5$ (red) multilayers, measured 16 days after the deposition of the membranes in the storage solution at 4°C.

Since the preservation of ALP activity when immobilised in multilayers assembled in membrane pores was successfully demonstrated, the morphologies of the mineralized individual tubes after their release from the PC template were imaged by SEM. Two types of systems were studied, the LbL assembly of $(PAH/ALP)_5$ and $(Col/HA)_3(PAH/ALP)_5$ multilayers in the parallel pores of a PC membrane followed by mineralization, by incubation in $CaCl_2$ and Mg-glycerol phosphate during 48 h at 37°C. The results are shown in Figure 3.8.

Low magnification SEM images reveal the formation of nanotubes in both cases studied (Figure 3.8A and B). However, these are less clearly visible in the case of mineralized $(PAH/ALP)_5$ nanotubes, indicated by arrows on Figure 3.8A, due to the presence of polycarbonate residues originating from the template membrane. This could be due to an insufficient decrusting of the PC membrane surfaces resulting in the formation of a mineralized layer on the surface, which could partly inhibit the proper dissolution of the PC membrane. In Figure 3.8B, the dissolution issue is less pronounced and a higher amount of mineralized $(Col/HA)_3(PAH/ALP)_5$ nanotubes is obtained compared to the previous case. Moreover, these tubes reach longer lengths, up to 12 nm, indicating a potential influence of the $(Col/HA)_3$ layers on nanotubes formation and mineralization.

High magnification SEM images (Figure 3.8C and D) show that the mineralization of both types of multilayers results in nanotubes whose thickness corresponds to the membrane pore diameters (300 nm). The morphology of these nanotubes suggests their successful mineralization compared to non-mineralized $(PAH/ALP)_5$ tubes which are flattened and without mechanical strength, shown in Appendix A. However, it appears that both systems studied result in globally not well defined and mainly broken nanotubes.

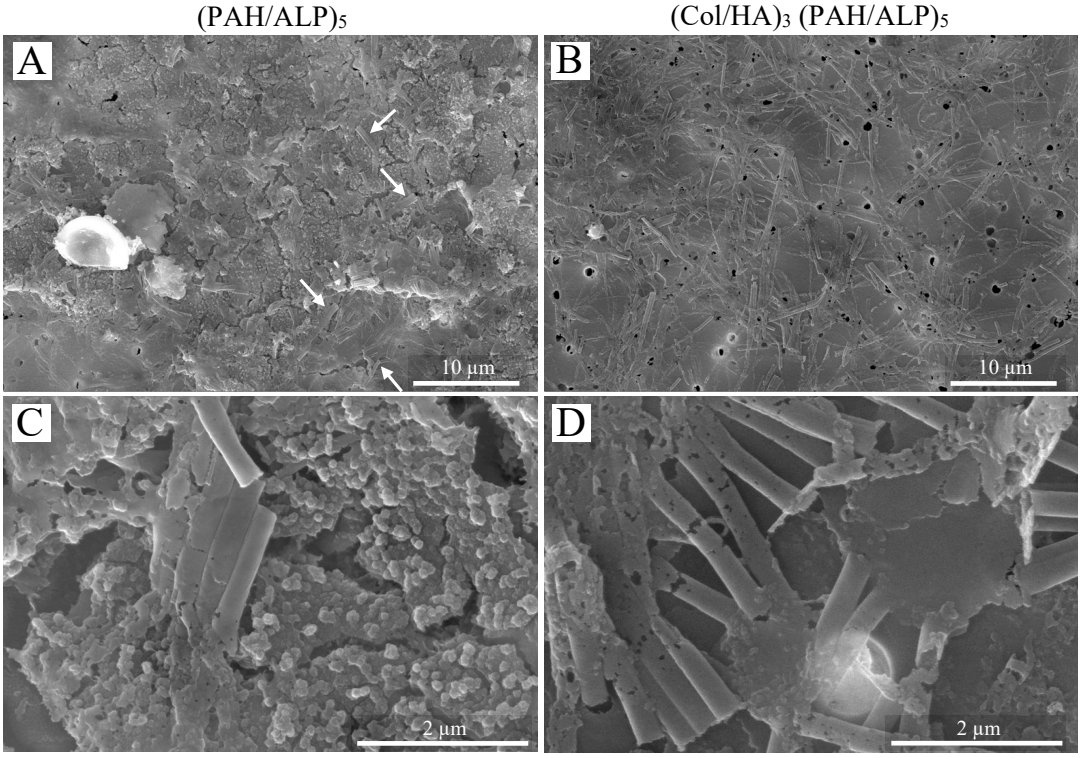


Figure 3.8: SEM images of the $(PAH/ALP)_5$ (A,C) and $(Col/HA)_3(PAH/ALP)_5$ (B,D) nanotubes formed in PC membranes with parallel nanopores (300 nm diameter) and subsequently mineralized at 37°C during 48h.

Energy-dispersive X-ray spectroscopy (EDX) analyses were carried out to identify and quantify the elemental composition of the nanotubes formed. The resulting spectra for the two systems studied are shown in Figure 3.9. These spectra reveal two prominent peaks in both cases, one at 2.013 keV and the other at 3.69 keV corresponding respectively to the emissions of P and Ca, the main components of hydroxyapatite (whose chemical formula is $Ca_{10}(PO_4)_6(OH)_2$). The Ca/P ratio is equal to 1.56 for nanotubes formed from mineralized $(PAH/ALP)_5$ multilayers (Figure 3.9A) and has a value of 1.46 for mineralized $(Col/HA)_3(PAH/ALP)_5$ nanotubes (Figure 3.9B). As these values are not close to the Ca/P ratio of biological hydroxyapatite, which is 1.67, it is insufficient to conclude that the CaP mineral formed is indeed HAp. Furthermore, other peaks are also present on the EDX spectra and they correspond to the elements C, O, Mg and Al. The presence of Mg comes from the $Mg^{2+}$ ions of the mineralization solution ($CaCl_2$ and Mg-glycerol phosphate) which partly substitutes $Ca^{2+}$ in the hydroxyapatite composition. This result was highlighted by Colaço et al in a study on enzymatic-induced mineralization of calcium phosphate in solution, proving the presence of $Mg^{2+}$ ions in the surface of CaP particles. [55]
These EDX spectra therefore allow confirming the successful formation of CaP mineral in both types of nanotubes studied.

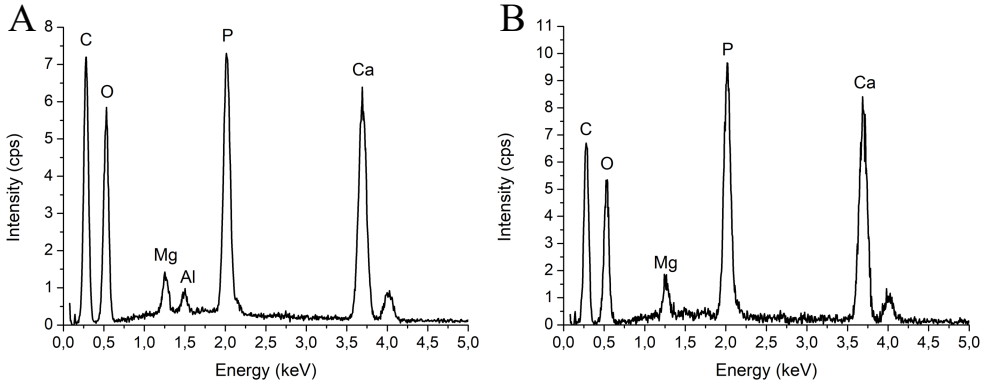


Figure 3.9: EDX spectra identifying and quantifying the elemental composition of individual mineralized nanotubes composed of $(PAH/ALP)_5$ (A) and $(Col/HA)_3(PAH/ALP)_5$ (B) multilayers.

SEM images showed a slight improvement in the case of mineralized $(Col/HA)_3(PAH/ALP)_5$ multilayers (Figure 3.8B and D) that provide a higher amount of nanotubes reaching longer lengths, but these are nevertheless not uniform and partially porous, highlighting a lack of stability. This enhancement may be associated to either the higher enzymatic activity demonstrated previously or to the significant role of the $(Col/HA)_3$ multilayer in mineralization proven on planar surfaces, or a combination of both phenomena.
This leads to the conclusion that the assembly of $(PAH/ALP)_5$ and $(Col/HA)_3(PAH/ALP)_5$ multilayers followed by mineralization result in the formation of mineralized nanotubes. However, the systems studied require some improvements to obtain nanotubes with better mechanical stability and whose length reaches expected values close to 25 $\mu$m, the thickness of the template membrane.

### 3.2.2 Influence of confinement on nanotube formation and mineralization

The influence of confinement on nanotubes formation and mineralization was investigated by the assembly of $(PAH/ALP)_5$ and $(Col/HA)_3(PAH/ALP)_5$ multilayers performed in PC membranes with straight pores of different diameters, i.e. 200, 300 and 500 nm. A previous study carried out by Colaço et al. on 200 and 500 nm pores showed that the confinement had an impact on the crystallinity of the mineral phase formed and that the influence of the $(Col/HA)_3$ multilayer on the mineralization was more pronounced in 500 nm pores due to a higher adsorption of collagen.[6] Therefore, varying the pore size of the template membrane could improve the mechanical stability of the formed nanotubes.
The influence of confinement was studied on two different systems and the conditions used for the layer-by-layer assembly and mineralization of the different multilayers are the same as those used in the previous study (3.2.1). After the collection of the nanotubes formed by dissolving the template membranes, the samples were analysed by SEM, as shown in Figure 3.10.

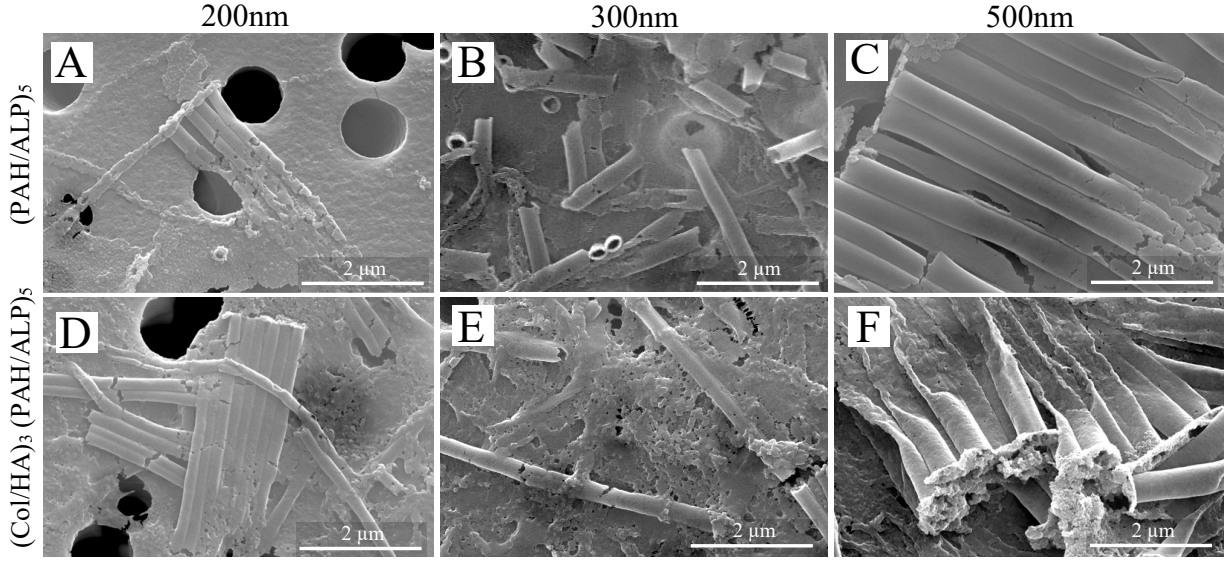


Figure 3.10: SEM images of the $(PAH/ALP)_5$ (A-C) and $(Col/HA)_3(PAH/ALP)_5$ (D-F) nanotubes formed in PC membranes with parallel nanopores of 200 nm (A,D), 300 nm (B,E) and 500 nm (C,F) and subsequently mineralized at 37°C during 48h.

The high magnification images reveal that the nanotubes formed from assembly and mineralization in 200 nm pores are broken and very brittle in both systems studied (Figure 3.10A and D). However, it appears that the presence of $(Col/HA)_3$ multilayers (Figure 3.10D) improves the formation and uniformity of the nanotubes without significantly enhancing their mechanical strength. Furthermore, very few nano-objects were collected on the PET membranes suggesting that a large proportion of the tubes were not properly formed or mineralized.

Then, the nanotubes constructed in the 300 nm pores appear to have different structures than those obtained in 200 nm pores, these are presented in Figure 3.10B and E. Indeed, they seem better formed over the thickness of the template membrane resulting in longer tubes, without reaching the value of the membrane thickness. The nanotubes of mineralized $(PAH/ALP)_5$ multilayers (Figure 3.10B) are more broken than those of the $(Col/HA)_3(PAH/ALP)_5$ (Figure 3.10E) multilayers suggesting weaker formation of the tubes. Overall, the nanotubes of 300 nm thickness have a better stability than those of 200 nm. This could be due to more pronounced diffusion constraints of (bio)macromolecules into nanopores of 200 nm which would result in poor mechanical integrity and therefore less stable nanotubes.

Finally, the most interesting results are those obtained with 500 nm pores, visible in Figure 3.10C and F. Indeed, the morphologies of the nanotubes collected are very different from those of the tubes constructed in the 200 and 300 nm pore size membranes. These nanotubes are well formed and defined close to the membrane surface but break, flatten and twist in the middle. A lower magnification SEM image of the nanotubes formed from the mineralized $(PAH/ALP)_5$ multilayers, shown in Figure 3.11, highlights this particular morphology. It can be seen that the phenomenon is present throughout the entire membrane thickness, allowing to reach nanotube lengths of 25 $\mu$m. These results could be due to the fact that the enzyme substrate diffuses more easily in larger pores and that the mineralization products are evacuated more efficiently, preventing the inhibition of enzymatic activity. The phenomenon of brittleness in the middle of the tubes is hard to explain, TEM analyses carried out at several stages during the mineralization process could provide a better visualisation of the mineralization mechanism in 500 nm pores.
Despite the use of the same method and conditions, these particular results obtained with 500 nm pores are different than those achieved previously by Colaço et al. ([6]), demonstrating the complexity of the build-up of such systems where many parameters have to be finely controlled.

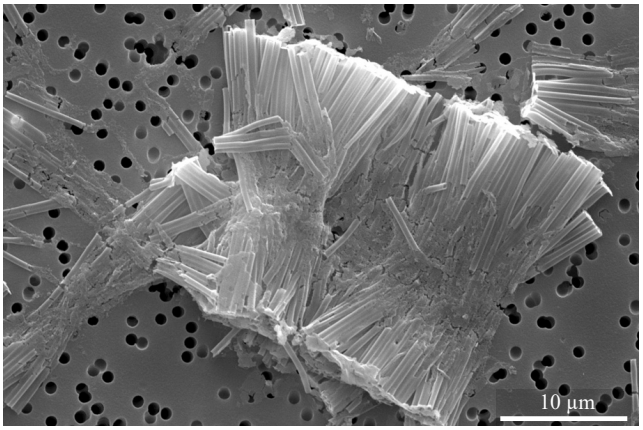


Figure 3.11: Low magnification SEM image of the $(PAH/ALP)_5$ nanotubes formed in a PC membranes with parallel nanopores of 500 nm diameter and subsequently mineralized at 37°C during 48h.

In conclusion, the results obtained in the different pore sizes of the template membrane showed that confinement had an effective impact on the formation and mineralization of nanotubes. The tubes built in the 500 nm pore size showed promising interesting results that require further improvements to achieve better uniformity and stability.

### 3.2.3 Influence of cross-linking conditions on nanotube formation and mineralization

The promising results obtained with nanotubes formed from mineralized $(Col/HA)_3(PAH/ALP)_5$ multilayers pave the way for the investigation of other parameters aiming at improving their mechanical stability. In the continuity of this study, the influence of a specific step in the synthesis of nanotubes in 300 nm pores has been analysed in more detail, namely the cross-linking step. This process allows the stabilisation of the $(Col/HA)_3$ multilayer formed by LbL assembly at pH 4.5 prior to subsequently adsorbing the five $(PAH/ALP)_5$ bilayers and performing the enzymatic-induced mineralization at physio-

logical pH. Indeed, the chemical cross-linking in the presence of EDC and NHS consists in the formation of amide bonds between the carboxyl groups of HA and the amine groups of Col, therefore stabilising the interactions between these biomacromolecules in the multilayers. The aim is to study the influence of temperature and a decrease of concentration on the stabilisation of the EDC/NHS complex and therefore the mechanical resistance of the $(Col/HA)_3$ multilayer, which has been shown to have an important impact on mineralization. Varying the cross-linking conditions could enhance the role of these three bilayers and therefore improve the stability of the nanotubes formed.
For this purpose, the $(Col/HA)_3$ multilayers built in the straight pores of a PC membrane (300 nm pore diameter) were stabilized by different conditions of cross-linking performed overnight: two cross-linkings with similar concentrations (EDC 30 mM/NHS 50 mM) but performed at RT or 4°C and a third cross-linking performed at 4°C with a concentration of EDC of 7.5 mM.

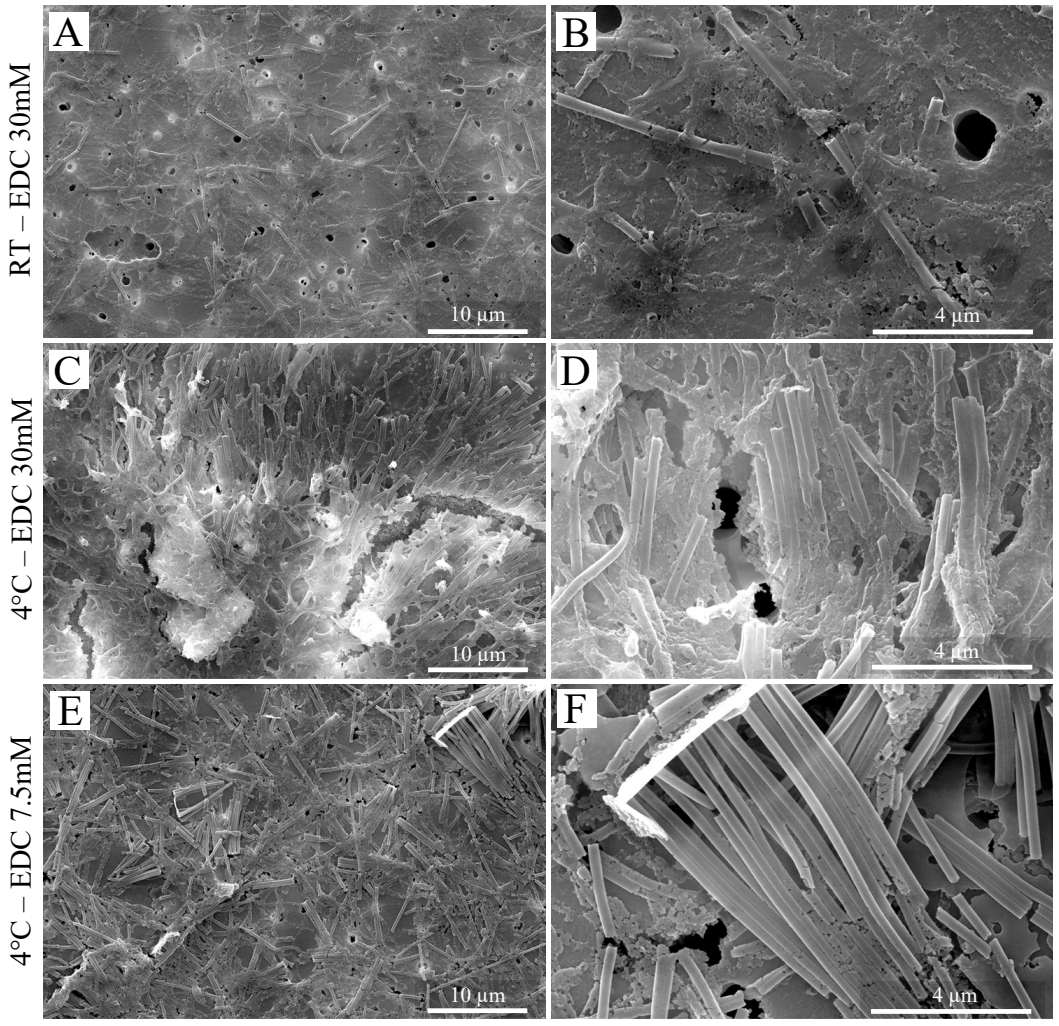


Figure 3.12: SEM images of $(Col/HA)_3(PAH/ALP)_5$ nanotubes formed in PC membranes with parallel nanopores (300 nm) and subsequently mineralized at 37°C during 48h. The cross-linking step was performed by incubation at RT in EDC(30 mM)/NHS(50 mM) solution (A,B) or at 4°C in either EDC(30 mM)/NHS(50 mM) (C,D) or EDC(7.5 mM)/NHS(50 mM) (E,F) solutions overnight.

The SEM images recorded for the three systems studied, shown on Figure 3.12, firstly highlight the influence of the cross-linking temperature on the amount of nanotubes collected. Indeed, by comparing Figures 3.12A, C and E, it appears that more nanotubes are collected on the PET membrane after dissolution of the PC template in the two last cases suggesting a better formation and/or mineralization of the tubes when cross-linking is performed at 4°C. Furthermore, the higher magnification images show more continuous and uniform nanotubes when the cross-linking was carried out at 4°C (Figure 3.12D and F).

Then, no relevant differences emerge from the SEM images of nanotubes whose $(Col/HA)_3$ bilayers were stabilised by incubation at 4°C in cross-linking solutions of different concentrations, without taking into account the numerous PC residues, visible in Figure 3.12C, which are due to a dissolution issue described previously. It therefore seems that a decrease in the concentration of EDC does not significantly affect the mineralized multilayers constituting the nanotubes.
As a result, this study demonstrated the influence of the temperature at which the cross-linking step was carried out on the formation of nanotubes, suggesting a better stabilization of the EDC/NHS complex at the temperature of 4°C. Then, a change of EDC concentration did not show a significant impact on the stability of the formed nanotubes. However, a more quantitative study on the influence of the concentration of EDC and NHS on cross-linking of Col and HA in nanopores would be useful in order to draw a more well-founded conclusion on the effect of the concentration.

### 3.2.4 Replacement of hyaluronic acid (HA) by alginate (ALG)

Given the previous results on individual nanotubes formed from mineralized $(Col/HA)_3(PAH/ALP)_5$ multilayers, which showed the influence of the collagen and hyaluronic acid multilayer on tube formation, the assembly of collagen with another polyanion is investigated. Therefore, hyaluronic acid (HA) present in the three $(Col/HA)_3$ bilayers was replaced by alginate (ALG), a polymer with similar structural and physicochemical properties. Alginate is a natural disaccharide produced by brown seaweed and approved by the U.S. Food and Drug Administration (FDA). It is extensively used in medical applications due to its excellent biocompatibility and its ability to support osteoblast differentiation. [56, 57] The layer-by-layer assembly of alginate with collagen on a planar titanium surface has shown promising results in a previous study, resulting in a biocompatible fibrillar structure that mimics the ECM. [58]
Thus, based on this study, LbL assembly of $(Col/ALG)_3(PAH/ALP)_5$ multilayers in the straight pores of a PC membrane followed by mineralization were performed. For this purpose, a first anchoring layer was built followed by the assembly of Col and ALG into three bilayers. This assembly was carried out at pH 4. Indeed, since the isoelectric point of Col is between 6 and 7 ([6, 53]) and the pKa of ALG is around 3.2 ([59]), the former is expected to be positively-charged while the latter is negatively-charged at pH 4, thus favouring their electrostatic attraction. Then, the formed layers were stabilised by chemical cross-linking at RT or 4°C overnight. After stabilisation of the multilayers deposited, PAH and ALP were assembled into five bilayers at pH 7.4 and 37°C with subsequent mineralization by incubation in $CaCl_2$ and Mg-glycerol phosphate solution during 48h at 37°C. The individual mineralized nanotubes formed were then collected on a PET filter by the dissolution of the membrane template.

In a first step, the replacement of HA by ALG was studied by building nanotubes in 300 nm pores with similar conditions as the first studied nanotube systems formed from the mineralized $(Col/HA)_3$ $(PAH/ALP)_5$ multilayers (section 3.2.1). The SEM results obtained in this study are shown in Figure 3.13A and B. The low and high magnification images show the successful formation of a high number of mineralized nanotubes. These tubes have a diameter around 300 nm on average but their length does not reach the value of the membrane thickness, i.e. 25 $\mu$m. These tubes are rather well formed but they lack sufficient mechanical stability as in the case with hyaluronic acid. These results show, however, that the replacement of HA by ALG in multilayers with Col is effective and allows the production of individual mineralized nanotubes.

In a second step, LbL assembly of $(Col/ALG)_3(PAH/ALP)_5$ multilayers and subsequent mineralization was carried out in PC membranes with 500 nm pores to investigate whether the use of ALG allowed the formation of nanotubes in different pore sizes. As shown in Figure 3.13C and D, the morphology of the tubes obtained is similar to the one with hyaluronic acid in 500 nm pores (Figure 3.10F), i.e. well-formed tubes close to the membrane surface that flatten, twist and break in the middle. This again suggests that the replacement of HA by ALG does not affect nanotube formation and that the mineralization mechanism is therefore relatively similar.
However, it should be noted that a study in 200 nm pores did not allow the collection of $(Col/ALG)_3$ $(PAH/ALP)_5$ nanotubes on the PET membrane. The use of this type of PC membrane with hyaluronic acid had shown the formation of few relatively brittle tubes (Figure 3.10D). The absence of nanotubes

with alginate could be explained by the fact that these fragile tubes did not have sufficient mechanical strength to be harvested or that ALG could not diffuse sufficiently into this pore size preventing the build-up of the multilayers. Further experiments should be needed to understand the exact mechanism of the assembly of ALG with Col in 200 nm pores.

In a third step, an attempt was made to improve the stability of the three $(Col/ALG)_3$ bilayers by modifying the cross-linking temperature to 4°C, based on the previously demonstrated results (section 3.2.3), and by increasing the EDC concentration to a value of 100 mM, according to a study of Richert et al. achieving a multilayer with improved stability by cross-linking at high EDC concentrations.[60] As shown in Figure 3.13E and F, the studied system leads to the successful formation of mineralized nanotubes. These tubes, being retained by a film formed at their end, hold vertically demonstrating good rigidity and homogeneity. However, the comparison with the nanotubes whose cross-linking was performed at RT with EDC 30 mM (Figure 3.13A and B) makes it difficult to affirm that the variation of cross-linking conditions has significantly improved the stability of the nanotubes.

In conclusion, the replacement of hyaluronic acid by alginate in the three bilayers with collagen similarly leads to the successful formation of mineralized nanotubes in 300 and 500 nm nanopores. Decreasing the incubation temperature and increasing the EDC concentration in the cross-linking solution seems to well stabilize the formed multilayer of Col and ALG resulting in homogeneous nanotubes.

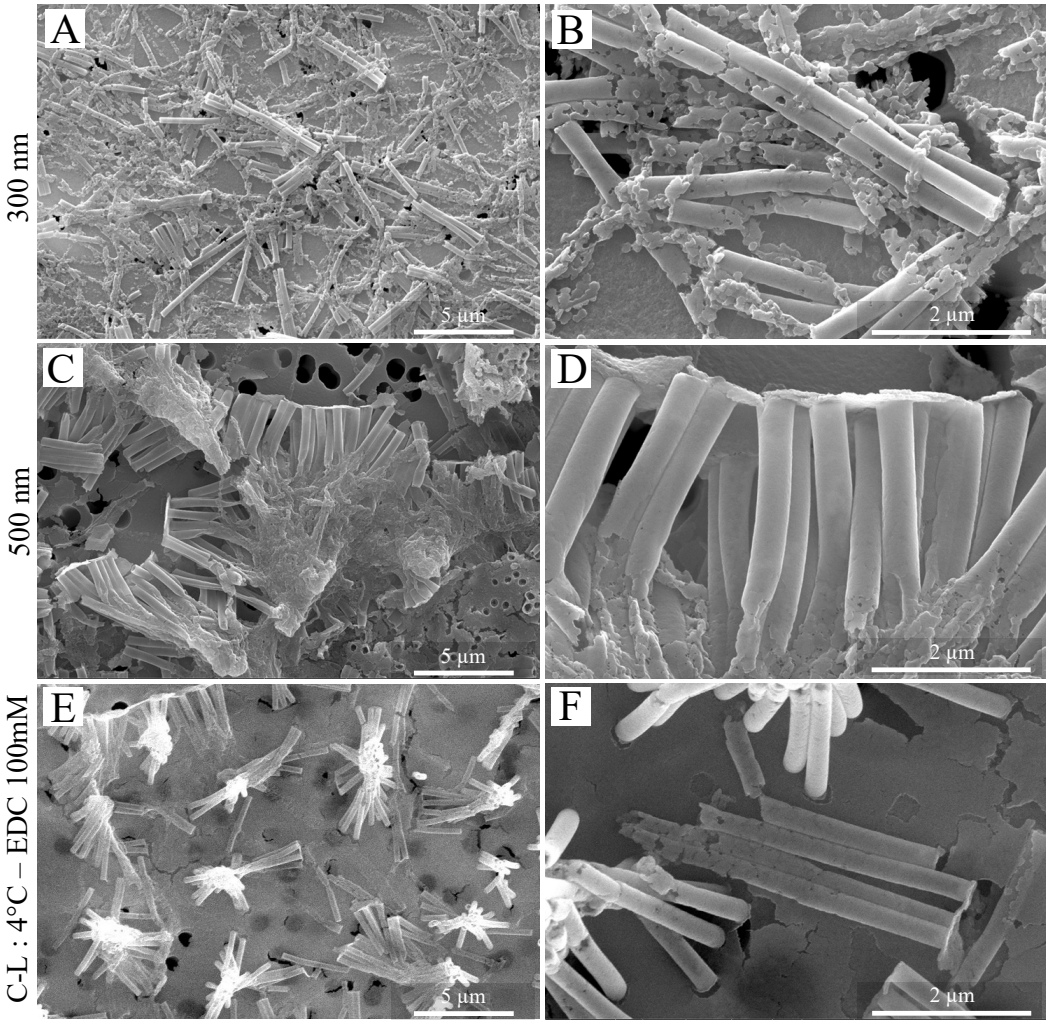


Figure 3.13: SEM images of $(Col/ALG)_3(PAH/ALP)_5$ nanotubes formed in PC membranes with parallel nanopores of 300 nm (A,B) and 500 nm (C,D) size and subsequently mineralized at 37°C during 48h. The cross-linking step was performed by incubation at RT in EDC(30mM)/NHS(50mM) solution (A-D) or at 4°C in EDC(100mM)/NHS(50mM) (E,F) solution overnight.

## 3.3 LbL assemblies and mineralization in intersected nanopores

The previously obtained promising results of individual mineralized nanotubes formed in the straight pores of a PC membrane raised the interest to extend the technique into PC membranes with intersected nanopores. The aim is therefore to synthesise a network of intersected nanotubes of ECM-derived macromolecules that closely mimics the bone extracellular matrix. For this purpose, the layer-by-layer assembly of collagen, hyaluronic acid and alkaline phosphate in the intersected pores of the template membrane followed by mineralization were carried out with the same steps and conditions as in the PC membranes with parallel pores (described in section 3.2.1).
As schematically illustrated in Figure 3.14, the main steps for the assembly and mineralization of $(Col/HA)_3$ $(PAH/ALP)_5$ multilayers in the intersected pores of a PC membrane were firstly the build-up of an anchoring layer, then the $(Col/HA)_3$ multilayers were deposited at RT and pH 4.5 followed by overnight cross-linking. The five bilayers $(PAH/ALP)_5$ were then assembled at pH 7.4 and 37°C and were subsequently mineralized during 48h at 37°C. Finally, the intersected nanotube network was collected on a PET membrane by dissolving the template in order to analyze the built structure.

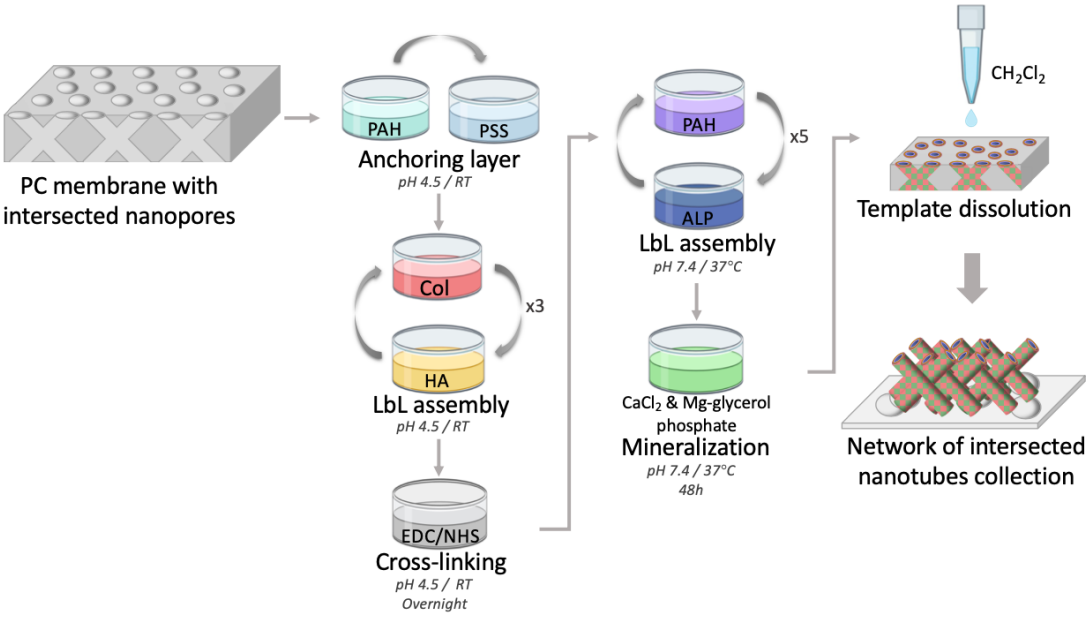


Figure 3.14: Schematic representation of the strategy used for the formation of mineralized $(Col/HA)_3(PAH/ALP)_5$ multilayers in a PC membrane with intersected nanopores.

Prior to SEM analysis of the morphology of the mineralized nanotube network, the enzymatic activity of alkaline phosphatase (ALP) embedded in the multilayers deposited in the intersected nanopores was measured to verify whether the enzyme maintained its activity. To do this, the amount of 4-nitrophenol (pnp) produced by immersing the membrane in a 7 mM 4-nitrophenyl phosphate (pnpp) solution was recorded by UV-visible spectrophotometer at 37°C during 20 minutes by agitating the pnpp solution every 5 minutes. Therefore, the absorbance versus time was recorded to determine the enzymatic activity of ALP in the $(PAH/ALP)_5$ or $(Col/HA)_3(PAH/ALP)_5$ multilayers shortly after the LbL assemblies, the result is shown in Figure 3.15A (fresh). These enzyme activities (in $\mu$mol.L$^{-1}$.min$^{-1}$) were then determined by converting the absorbance to the amount of pnp produced and measuring the slope of the linear regression line corresponding to the initial rate of pnp production. These values were then normalised by the surface area of membrane pores to compare the enzyme activities measured for the different samples. The resulting enzymatic activities (in $\mu$mol.L$^{-1}$.min$^{-1}$.cm$^{-2}$) are summarised in the histogram shown in Figure 3.15B. The trend obtained with the activities measured shortly after LbL assembly (Figure 3.15B, fresh) is similar to the one achieved in the straight nanopores (Figure 3.6B, fresh). Indeed, an increase in activity of about 17% can be detected with the multilayers containing the three $(Col/HA)_3$ bilayers compared to without. The reasons for this increase could therefore be analogous to those in parallel pores,

i.e. a greater amount of ALP entrapped by the presence of the bilayers $(Col/HA)_3$ and/or an enhancement of activity by the interaction of Col and HA with ALP.

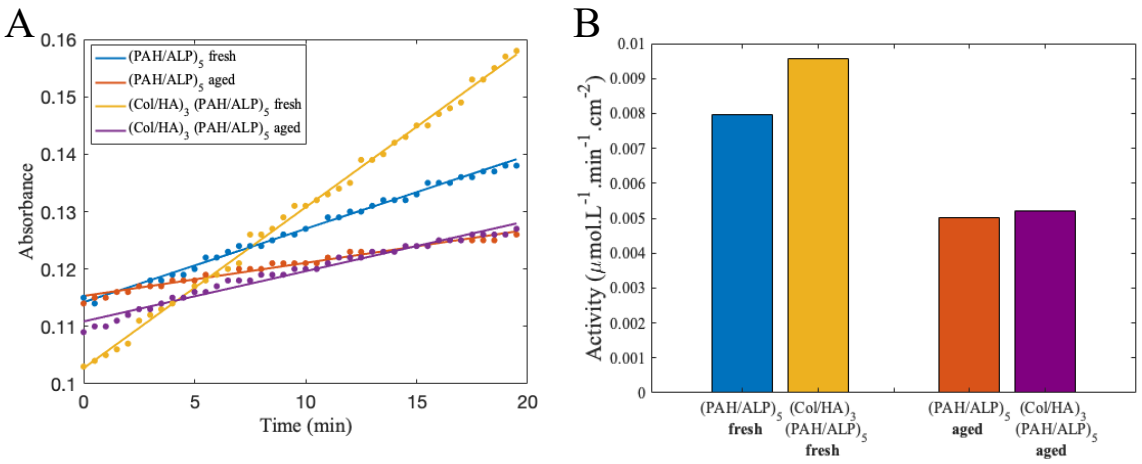


Figure 3.15: ALP activity in $(PAH/ALP)_5$ (blue and orange) and $(Col/HA)_3(PAH/ALP)_5$ (yellow and purple) multilayers built in PC membranes with intersected pores, measured rapidly after the assembly (fresh) and after 12 days (aged). (A) Evolution of the absorbance versus time due to the production of pnp, measured by UV-visible spectrophotometer at 410 nm and 37°C. (B) Histogram of enzyme activity computed from pnp concentration versus time.

Subsequently, the preservation of enzyme activity over time was investigated by measuring the absorbance with membranes containing the $(PAH/ALP)_5$ or $(Col/HA)_3(PAH/ALP)_5$ multilayers stored during 12 days at 4°C in Milli-Q water at pH 7.4. The resulting graphs are shown in Figure 3.15A (aged). As with the freshly measured activities, the enzymatic activities normalised by the surface area of the membrane pores were calculated and can be seen in the histogram in Figure 3.15B (aged). The gap between the activities in the presence or absence of the $(Col/HA)_3$ bilayers is less marked after 12 days than freshly measured but is still slightly present. Then, comparing the activities measured rapidly or 12 days after LbL assembly, it appears that the activity significantly decreased with time, by about 38% in the absence and about 46% in the presence of the $(Col/HA)_3$ bilayers. As previously demonstrated, this decrease in activity is presumably related to the desorption of ALP during membrane storage.
This allows to conclude that the enzymatic activity is preserved when ALP is assembled in five bilayers with PAH in the intersected pores of the PC membrane. Furthermore, the trend between the different systems also confirms the results obtained previously with straight pores and removes the doubt about a certain measurement error.

After confirming the preservation of ALP activity in the PC membranes with intersected pores, the nanotubes mineralized by incubation in a solution of $CaCl_2$ and Mg-glycerol phosphate at 37°C during 48h were analysed. For this purpose, the network of intersected nanotubes collected on a PET filter after the dissolution of the template membrane is imaged by SEM. The build-up of two different systems was studied, first a network of nanotubes composed of mineralized $(PAH/ALP)_5$ multilayers and then intersected nanotubes built from mineralized $(Col/HA)_3(PAH/ALP)_5$ multilayers. The analysis of the morphology of the two networks of nanotubes formed gives a good overview on the mineralization of the tubes, a complementary information is the identification and quantification of the elemental composition of these nanotubes. To this end, EDX analyses were performed on the two different samples.

Figure 3.16 summarizes the different results obtained for the $(PAH/ALP)_5$ nanotube networks, i.e. SEM images (A,B,C) and EDX spectrum (D).
The low magnification SEM images (Figure 3.16A and B) firstly demonstrate the successful formation of a large network of hollow intersected nanotubes. These images taken from the top reveal the straight position of the nanotubes, suggesting that they are well mineralized and thus have good mechanical

strength. The nanotube network seems to be fixed by a film that has formed on the bottom and top of it. This film may be due to mineralization on the surface of the PC membrane caused by the presence of a macromolecular film formed during the LbL assembly despite the decrusting step.
The higher magnification SEM image (Figure 3.16C) gives a better view of the morphology of the formed nanotubes. Various interesting features can be observed such as broken tubes (shown by an arrow), tubes with a well-defined intersection (circled) and several tubes joining without being completely defined (framed). These nanotubes have an external thickness close to the pore size of the template membrane, which is 300 nm, but their length does not reach the expected value, which is the membrane thickness (25$\mu$m) divided by sin(45). This suggests that their mechanical stability was not sufficient to maintain their full length or that the nanotubes did not form uniformly along the entire pore length.
Thirdly, the EDX spectrum (Figure 3.16D) contains two intense peaks corresponding to the elements P and Ca, the main elements of hydroxyapatite, indicating successful mineralization of the nanotubes. This analysis determined the Ca/P ratio which is 1.60, a value close to the ratio of stoichiometric biological hydroxyapatite, which is 1.67, but not enough to affirm that the CaP mineral formed is indeed HAp. In addition, a peak at an energy of 1.253 keV corresponding to Mg emission is also present on the EDX spectrum, which is in agreement with the results obtained with straight pores (Figure 3.9).
The present results demonstrate the feasibility of producing networks of intersected mineralized nanotubes with rather good mechanical strength from $(PAH/ALP)_5$ multilayers. However, some improvements are necessary in terms of stability along the entire length of the tube in order to reach a denser network like the one obtained with polypyrrole nanotubes, presented in Figure 2.2.

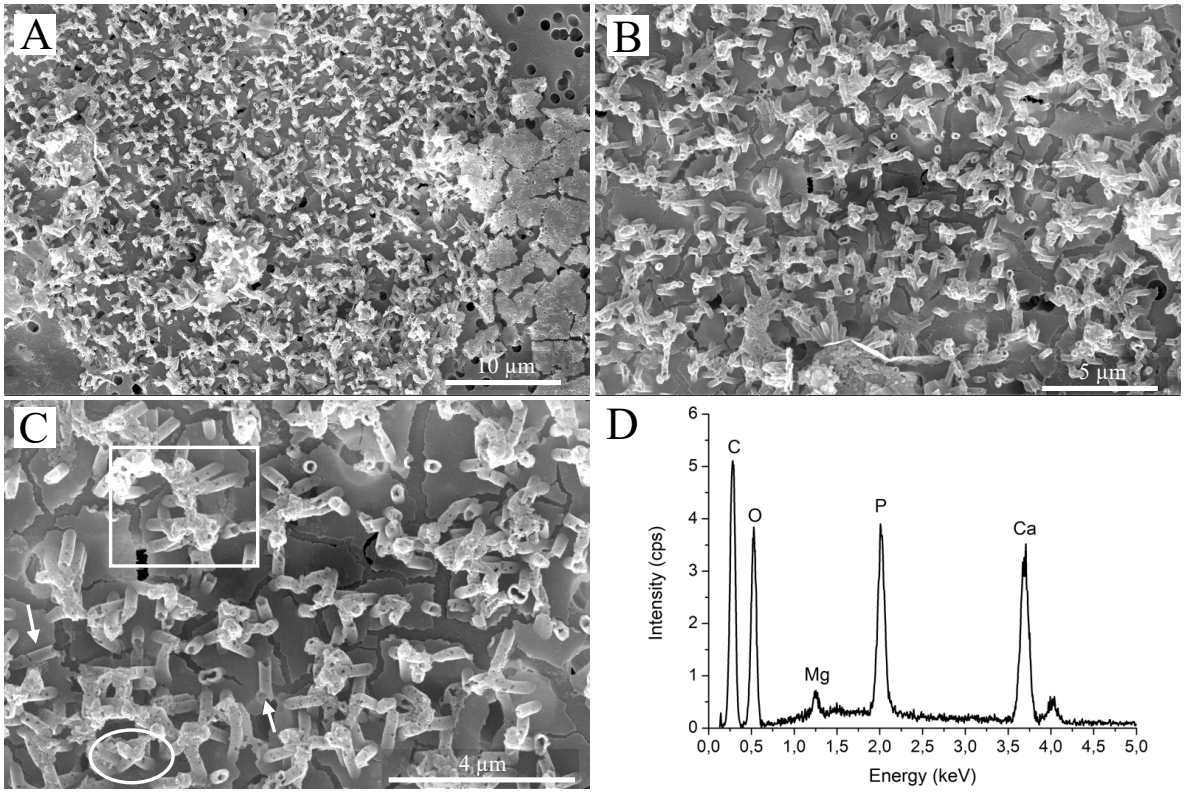


Figure 3.16: Characterisation of intersected nanotubes formed by the assembly of $(PAH/ALP)_5$ multilayers in the intersected pores of a PC membrane and the subsequent mineralization at 37°C during 48h : SEM images at low (A,B) and high (C) magnification characterising the morphology, the arrows indicate broken tubes, the circle shows a well-defined intersection between two tubes and the square shows joining tubes, and EDX spectrum (D) defining the elemental composition.

LbL assembly of $(PAH/ALP)_5$ multilayers and subsequent mineralization in intersected nanopores was performed a second time with exactly the same conditions in order to study the reproducibility of

such mineralized intersected nanotube network. The SEM results, shown in Figure 3.17A and B, also show the successful formation of an intersected nanotube network. However, the morphology of this network is not exactly the same as the one obtained previously. Indeed, the nanotubes reach higher lengths and the network is more compact in this case. Moreover, the tubes seem to be clogged in contrast to the previous one where their hollowness was clearly visible. The EDX spectrum, visible in Figure 3.17C, contains, as in the previous study, two intense peaks corresponding to the elements P and Ca, confirming the successful formation of CaP mineral. However, the peak corresponding to the element C, at an energy of 0.277 keV, is significantly higher than the other two peaks of P and Ca. This could be related to the presence of a large amount of polycarbonate originating from the template membrane.
These rather significantly different results highlight the complexity of the construction of such nanotubular systems due to a high number of parameters that should be finely controlled. In particular, the persistent formation of rigid films, during the nanotube fabrication process, on top and bottom of the PC template membrane can block the entrances of the pores preventing the full construction and/or mineralization of the nanotubes. The presence of those rigid and compact films on both template surfaces can also impact on its further dissolution and thereby on the release of the nanotube network.

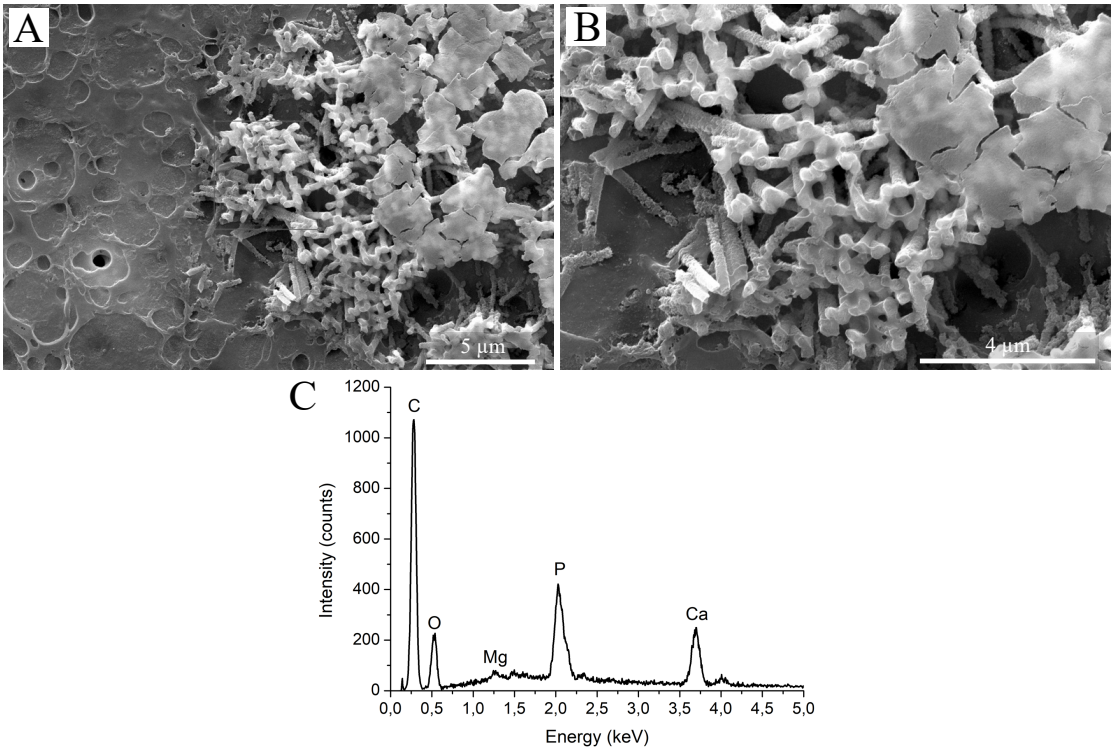


Figure 3.17: Characterisation of intersected nanotubes formed by the assembly of $(PAH/ALP)_5$ multilayers in the intersected pores of a PC membrane and the subsequent mineralization at 37°C during 48h : SEM images characterising the morphology (A,B) and EDX spectrum defining the elemental composition (C).

The LbL assembly and mineralization in intersected nanopores were then studied with $(Col/HA)_3$ $(PAH/ALP)_5$ multilayers. The resulting SEM images and EDX spectrum are promising and can be seen in Figure 3.18. Indeed, the low magnification SEM images (Figure 3.18A and B) demonstrate equivalent results to those obtained with $(PAH/ALP)_5$ multilayers (Figure 3.16) and a well-formed network of mineralized nanotubes can be seen. The film that holds the network in place is also present and the top film is clearly visible in Figure 3.18A.
The SEM image with higher magnification (Figure 3.18C) reveals similar morphologies to those observed previously, but it seems that the tubes are more homogeneously formed in this case. This is in agreement with the results obtained on individual nanotubes where the influence of the $(Col/HA)_3$ multi-

layer on mineralization has been well demonstrated and this could also be related to the fact that a higher enzymatic activity was obtained with the presence of these three bilayers (Figure 3.15B). The difference is less significant in this case, but a slight improvement in mechanical strength can be observed.
Finally, the EDX spectrum (Figure 3.18D) shows the presence of the elements P and Ca in the composition of the nanotubes, highlighting their successful mineralization. The Ca/P ratio calculated from the elemental analysis is 1.39. This value being rather far from the expected Ca/P ratio of hydroxyapatite (1.67) does not allow to conclude that the CaP mineral phase is hydroxyapatite.
In short, these preliminary results show that the assembly of $(Col/HA)_3(PAH/ALP)_5$ multilayers in the intersected pores of a PC template, followed by mineralization lead to the formation of networks of mineralized nanotubes and that the presence of the $(Col/HA)_3$ bilayers has a favourable impact on the mechanical stability of the nanotubes. Though, optimization of the fabrication process is still required to achieve stronger networks of fully well-shaped nanotubes.

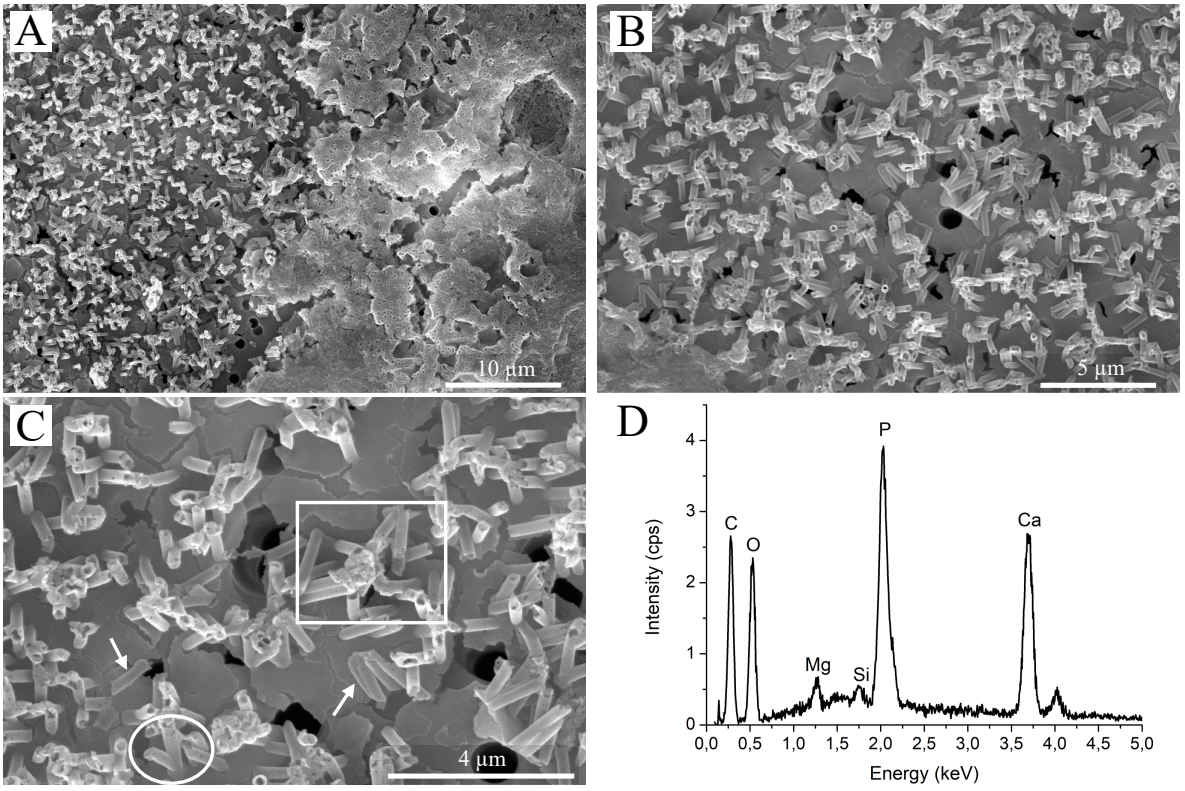


Figure 3.18: Characterisation of intersected nanotubes formed by the assembly of $(Col/HA)_3(PAH/ALP)_5$ multilayers in the intersected pores of a PC membrane and the subsequent mineralization at 37°C during 48h : SEM images at low (A,B) and high (C) magnification characterising the morphology, the arrows indicate broken tubes, the circle shows a well-defined intersection between two tubes and the square shows joining tubes, and EDX spectrum (D) defining the elemental composition.

The presence of the rigid film in the three different cases studied being questionable, the surface of the polycarbonate membrane, after the LbL assembly of the $(Col/HA)_3(PAH/ALP)_5$ multilayers and the subsequent mineralization, was analysed by SEM. A hypothesis for the presence of this coating could be that the decrusting step with NaCl (3 M, pH12) to remove the (bio)macromolecules deposited on the membrane surface during LbL assembly is not completely effective and that a mineralized multilayer crust is formed on the surface of the PC membrane. To investigate this assumption, two different PC membrane surfaces were imaged, one that underwent the decrusting steps during nanotubes synthesis and a second without these cleaning steps.
The images in Figure 3.19A and C, showing the surface of a non-decrusted membrane, highlight a sur-

face mineralization similar to the one observed while studying the LbL assemblies and mineralization on planar surfaces (Figure 3.3B and D). Indeed, small aggregated particles but also larger CaP spheres are present with the formation of mineral particles preferentially close to fibrillar nanostructures, probably collagen fibers. This suggests that a non-negligible amount of (bio)macromolecules assembled on the surface of the PC membrane which were then enzymatic-induced mineralized. The formed mineral layer blocks the nanopores of the membrane at some locations preventing the enzyme substrates from diffusing into the pores and thus resulting in poorly mineralized nanotubes.
SEM images of the surface of the PC membrane that has undergone the decrusting steps show a smooth, material-free surface, visible in Figure 3.19B and D. Compared to the images of the non-decrusted membrane (Figure 3.19A and C), it is evident that the decrusting step is essential and allows an efficient removal of the (bio)macromolecules deposited on the surface. These results do not therefore support the hypothesis of an inefficient decrusting that would explain the presence of the rigid film observed above and below the intersecting nanotube networks. This film can be a residue from the surface of the PC template that has not been completely dissolved. This could explain the presence of pores in this film clearly visible in Figure 3.18A, but could not provide an explanation for the film morphology visible in Figure 3.17A. This would mean that the PC membrane surfaces might not always be as successfully decrusted as presented here, in Figure 3.19B and D. This again highlights the numerous parameters that need to be finely controlled demonstrating the complexity of building such nanotube systems.

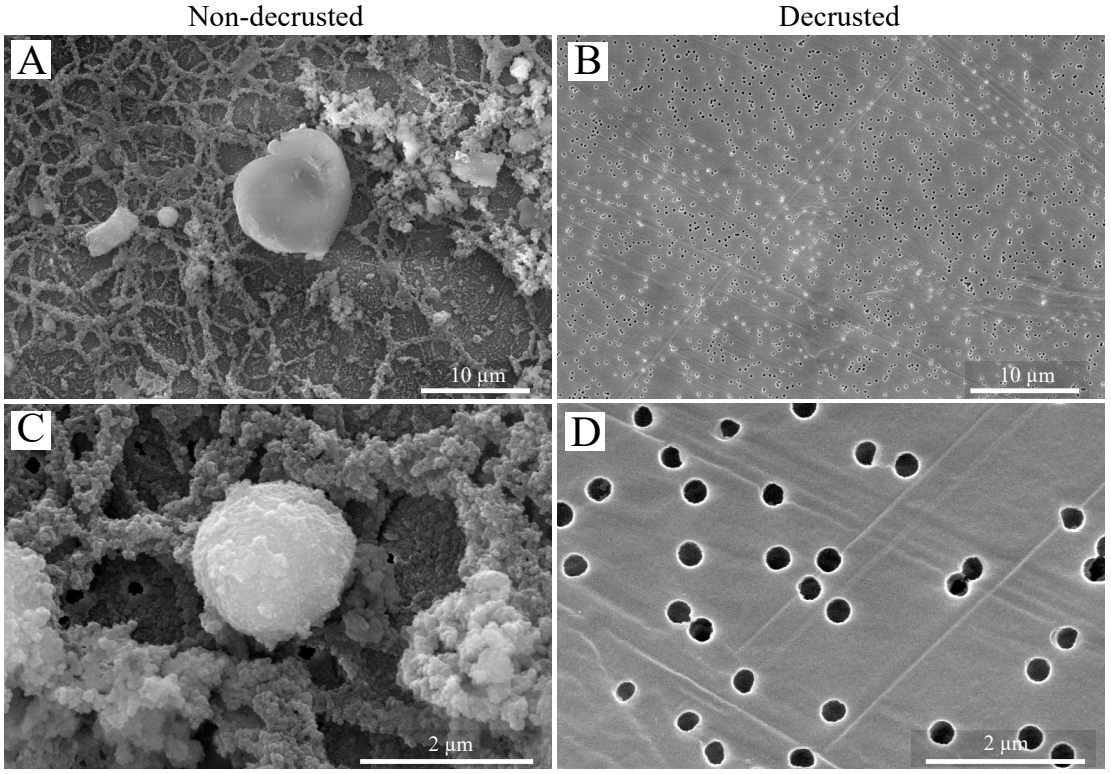


Figure 3.19: SEM images recorded on the surface of PC membrane after the build-up of $(Col/HA)_3(PAH/ALP)_5$ multilayers and subsequent mineralization at 37°C during 48h. (A,C) Surface of a membrane that has not undergone the decrusting steps and (B,D) surface of a membrane that has been cleaned several times.

## 3.4 Investigation of LbL assembly mechanisms in parallel vs intersected nanopores

Previous studies on the formation of mineralized nanotubes in parallel and intersected pores have proven to be successful. Indeed, SEM images showed evidence of mineralized nanotubes in both cases and EDX spectra confirmed the formation of CaP mineral indicating effective enzymatic-induced mineralization.

Previous studies have been carried out aiming at identifying the exact mechanism of assembly in straight pores but very few have been performed in intersected nanopores.
In order to investigate the mechanisms of LbL assembly and mineralization in straight and intersected pores, the quantitative results on enzyme activity in the two types of pores are compared in the histogram in Figure 3.20. The ALP catalytic activity values were normalised by the surface area of the membrane pores for comparing them. It should be noted that due to their orientation at 45°, the intersected nanopores are longer and the total surface area of the pores is therefore higher. The main features of the two types of template membranes, such as thickness, pore length and pore density, are listed in Table 3.1 below.

Table 3.1: Main features of PC membranes with parallel and intersected nanopores.

| | **Membrane with parallel nanopores** | **Membrane with intersected nanopores** |
|---|---|---|
| Average pore diameter | 300 nm | 300 nm |
| Thickness | 25 $\mu$m | 25 $\mu$m |
| Pore length | 25 $\mu$m | 35.35 $\mu$m |
| Pore density | $10^8$ cm$^{-2}$ | 2.8 $10^8$ cm$^{-2}$ |
| Surface area of 1 pore | 2.36 $10^{-7}$ cm$^2$ | 3.33 $10^{-7}$ cm$^2$ |

From the comparative histogram in Figure 3.20, it is first noticeable that the activity is significantly lower in the intersected pores than in the straight pores. Indeed, there is a decrease of 73% with the $(PAH/ALP)_5$ multilayers and the diminution is of about 80% with those of $(Col/HA)_3(PAH/ALP)_5$. This considerable difference is due to the surface area of the membrane intersected pores, which is about four times higher than the parallel ones. The higher density and length of the intersected pores could suggest a higher amount of (bio)macromolecules deposited during LbL assembly and thus a higher enzymatic activity, but the graph shows an opposite trend. This could be due to the fact that the deposition of ALP in intersected pores is less efficient than in straight pores or that the substrate of the enzyme diffuses less easily in intersected pores thus inducing a poorer catalytic activity or even that ALP loses its activity when immobilized in intersected pores. Further studies would be required to verify these hypotheses.
Another trend that emerges from this comparative histogram is the increase in activity in the presence of $(Col/HA)_3$ bilayers in both pore types studied. This phenomenon could be explained by the fact that the roughness of the $(Col/HA)_3$ bilayers allows more ALP to be trapped, inducing a higher activity or that collagen and/or hyaluronic acid have an activating catalytic capacity when they interact with ALP. This activity gap is however two times higher in parallel pores than in intersected nanopores. The assumption previously made about a higher diffusion constraint of (bio)macromolecules in intersected pores could explain this finding.

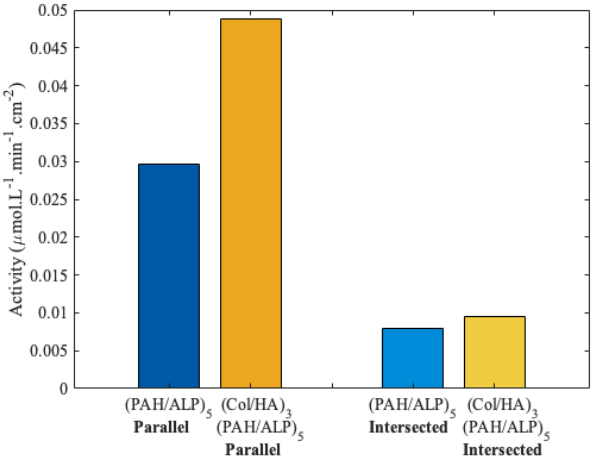


Figure 3.20: Histogram of enzyme activity of ALP assembled in multilayers of $(PAH/ALP)_5$ (blue) or $(Col/HA)_3(PAH/ALP)_5$ (yellow) formed in PC membranes with parallel (dark colors) and intersected (light colors) nanopores.

To study the influence of collagen and hyaluronic acid on ALP activity, enzymatic activity was measured in solution by recording the production of pnp in the presence of the pnpp substrate by UV-visible spectrophotometer at 410 nm and 37°C. For this purpose, absorbance versus time was measured for three different types of solutions: without collagen, with collagen (0.1 mg/mL) and with collagen (0.1 mg/mL) and hyaluronic acid (1 mg/mL), and different concentrations of ALP, i.e. 0.1 mg/mL, 0.05 mg/mL, 0.01 mg/mL and 0.005 mg/mL, were then added to these solutions to catalyse the hydrolysis reaction of pnpp. The different absorbance curves obtained were then converted into pnp concentration versus time curves. The ALP activity, corresponding to the initial rate of pnp production, was then determined for each ALP concentration by taking the slope of the linear regression line. The different activity values obtained for the three different solutions as a function of the four ALP concentrations are plotted in Figure 3.21A. Then, the specific activity in the different solutions was determined by taking the slope of the linear regression lines from the graph in Figure 3.21A, the values obtained are shown in the histogram in Figure 3.21B.

The specific activity is on average 87% higher in the absence than in the presence of collagen alone and collagen with hyaluronic acid. This result therefore suggests that these biomacromolecules do not have catalytic activating capacity. The effect of collagen and hyaluronic acid in solution is hard to explain and further investigations are required. This decrease in activity could be due to the fact that the presence of the biomacromolecules constrains the movement of ALP and thus limiting the access to the enzyme substrate.

In conclusion, these results therefore show that the higher activity observed in the pores with the $(Col/HA)_3$ bilayers is not directly due to an activating catalytic capacity of collagen and hyaluronic acid. Further investigations aiming at determining the amount of enzyme entrapped in LbL multilayers including or not $(Col/HA)_3$ bilayers are therefore required to verify the second hypothesis explaining the increased enzymatic activity in presence of Col/HA based bilayers.

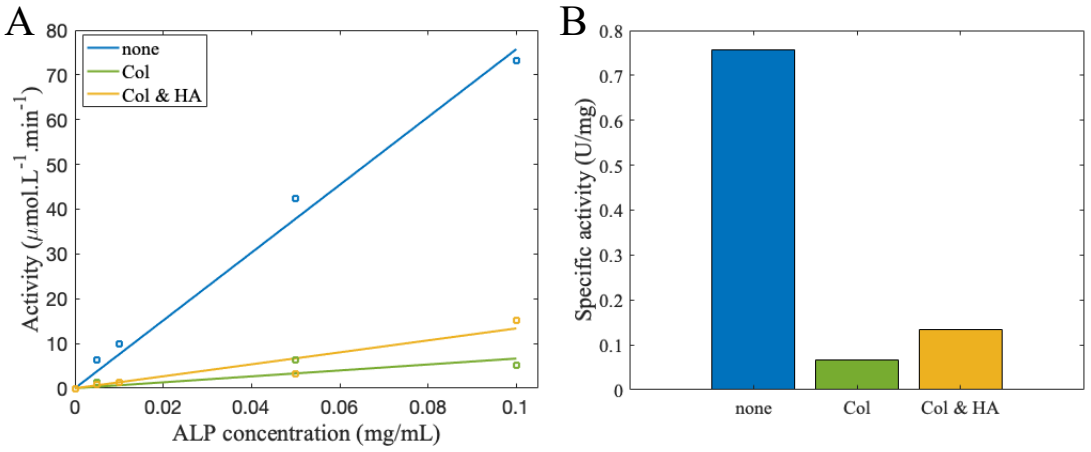


Figure 3.21: (A) Evolution of the enzymatic activity measured with UV-Visible spectrophotometer (410 nm and 37°C) as a function of ALP concentration in a solution of pnpp (7 mM) (blue), pnpp (7 mM) and Col (0.1mg/mL) (green) and pnpp (7 mM), Col (0.1mg/mL) and HA (1mg/mL) (yellow). (B) Histogram of the specific activity determined for the three different solutions.

# Chapter 4

# Conclusion and perspectives

The main purpose of this Master thesis was to produce biomineralized nanostructured biointerfaces mimicking the bone extracellular matrix for future use in tissue engineering applications. To achieve this, the techniques of layer-by-layer assembly, enzymatic-induced mineralization and template synthesis were combined. In this study, two types of nanoporous templates were used, i.e. PC membranes with parallel or intersected nanopores, giving rise to individual nanotubes for the former while the latter leads to the build-up of a network of intersected nanotubes, closely mimicking the ECM structure. The composite biointerfaces produced in this way are promising as they combine the biocompatibility and osteogenicity properties by including collagen and hyaluronic acid, as well as mechanical properties through the formation of hydroxyapatite using the biomineralization technique induced by the alkaline phosphatase enzyme.

The successful mineralization of (bio)macromolecule multilayers was demonstrated on planar surfaces and in porous membranes. Indeed, the production of CaP compounds was highlighted by infrared analysis on planar surfaces and the presence of Ca and P, the main elements of hydroxyapatite, was confirmed by EDX analysis on the built nanotubes. The LbL assembly of $(PAH/ALP)_5$ or $(Col/HA)_3(PAH/ALP)_5$ multilayers followed by mineralization in PC membranes with straight and intersected nanopores resulted in the successful formation of mineralized nanotubes, as evidenced by SEM analyses. The resulting individual and intersected nanotubes possessed a diameter equivalent to the size of the membrane pores, although their length did not reach the expected value related to the membrane thickness. This lack of mechanical stability points to the need for further optimization of the fabrication process in order to achieve fully well-shaped nanotubes.

The study on the incorporation of the three $(Col/HA)_3$ bilayers demonstrated the beneficial effect of collagen-based multilayers on the mineralized biointerfaces produced.
Indeed, this effect was first shown on planar surfaces where a more pronounced mineralization with a larger surface coverage was observed. Small aggregated particles as well as large spheres were produced in the presence of the Col/HA based bilayers. The ATR spectra showed however that these bilayers had no significant influence on the crystallinity of the particles formed.
Secondly, improvement on the formation and mineralization of nanotubes in the presence of collagen-based multilayers formed in straight and intersected nanopores was also demonstrated. SEM images revealed a greater amount of collected nanotubes reaching higher length values in the presence of the $(Col/HA)_3$ bilayers.
In order to enhance the effect of these Col/HA based multilayers, their stabilisation was investigated by varying the temperature and concentration of the cross-linking process. This study showed that a decrease in the cross-linking temperature to 4°C led to a better stabilisation of the EDC/NHS complex, highlighted by the formation of a greater amount of nanotubes being more continuous and uniform. However, a decrease of the EDC concentration in the cross-linking solution did not show promising results. One suggestion that could be investigated in the future, would be to increase the EDC concentration

while carrying out the cross-linking step at 4°C. This could enhance the pivotal role of the Col/HA based bilayers on the mechanical strength of the nanostructures formed.
The influence of collagen-based multilayers was also demonstrated when measuring the enzymatic activity in straight and intersected nanopores. A significant increase of activity in the presence of the $(Col/HA)_3$ multilayers was indeed observed, even when the measurements were performed after 12 days. These interesting results of higher enzymatic activity led to the investigation of a possible catalytic activating role of collagen and hyaluronic acid when interacting with ALP. The specific enzymatic activity in solution was in this way studied in the presence and absence of collagen and hyaluronic acid. The results showed a much higher activity in the absence of collagen, therefore discarding the hypothesis stated. Another explanation could therefore be that the roughness of the $(Col/HA)_3$ bilayers might lead to the entrapment of a greater quantity of ALP. Further investigations aiming at determining the exact amount of enzyme entrapped in the presence of the Col/HA based bilayers could be intersecting to verify this second hypothesis. It is important to mention, however, that all enzyme activity measurements were carried out only once for each system. It would be therefore useful to perform replicates in order to confirm the reported findings.

A second effect influencing the mineralization and formation of nanotubes was partly highlighted by the studies on enzymatic activity, this is the type of membrane template used.
Indeed, a significant loss of activity in intersected nanopores compared to parallel pores was demonstrated. Some hypotheses could explain this result, the most probable being that the diffusion of (bio)macromolecules would be less efficient in this type of nanopores. This assumption could be further analysed in detail by TEM analysis at several stages of assembly and mineralization in intersected nanopores.
The interesting results obtained in 500 nm straight pores highlight the influence of confinement on nanotube formation and mineralization. Nanotubes with well-formed ends and a length reaching the value of the membrane thickness were effectively obtained compared to 200 and 300 nm pores. This result is therefore promising but requires further investigation in order to understand the loss of mechanical strength present in the middle of the nanotubes.
The marked presence of a rigid film observed by SEM on the intersected nanotube networks showed the complexity of finely controlling the numerous parameters, such as the decrusting step and the dissolution of the template membrane, on the build-up of such nanotube systems. An improvement is clearly needed in this field to be able to later use the formed nanostructures in future biomedical applications.

The replacement of hyaluronic acid by alginate in bilayers with collagen led to the successful formation of individual mineralized nanotubes in 300 and 500 nm pores. This promising result highlighting the versatility of LbL assembly paves the way to new perspectives for tissue engineering applications. Indeed, it could be interesting to explore the incorporation of signaling molecules into the biointerfaces to induce osteogenic differentiation and therefore to generate new bone tissue. Indeed, many side effects on the direct injection of growth factors have been demonstrated in the literature and one way to circumvent them would be to directly adsorb growth factors such as the bone morphogenetic protein family into the multilayers forming the nanotubes or to integrate them into the hollow structure of the tubes.
A suitable scaffold for bone tissue engineering necessitates requirements at the structural, biological and mechanical levels. Regarding the structural requirements, the network of intersecting nanotubes offers promising porosity and a nanotopography similar to the one of the ECM. At the biological level, the incorporation of collagen and hyaluronic acid is promising for good biocompatibility and osteogenicity. Finally, as the mechanical properties of the biointerfaces formed in this study are unknown, a perspective would be to measure their compressive strength as well as their Young's modulus to study their possible suitability as an ECM-derived scaffold.
In order to complete the tissue engineering triad consisting of scaffold, growth factor and cells, one future prospect would be to study the adhesion, proliferation and differentiation of cells such as pre-osteoblast cells on the formed biointerfaces. This would allow studying the ability of the formed nanostructures to behave as cell-instructive material leading to the formation of new bone tissue.

# Bibliography


[1] X. Lin, S. Patil, Y. G. Gao, and A. Qian. The Bone Extracellular Matrix in Bone Formation and Regeneration. *Frontiers in Pharmacology*, 11(May):1–15, 2020.

[2] The Editors of Encyclopaedia Britannica. Homeostasis. `https://www.britannica.com/science/homeostasis`, 2020. [Online; Accessed 25 February 2021].

[3] B. M. Manzini, L. M. R. Machado, P. Y. Noritomi, and J. V. Lopes da Silva. Advances in Bone tissue engineering: A fundamental review. *Journal of Biosciences*, 46, 2021.

[4] R. Florencio-Silva, G. R. S. Sasso, E. Sasso-Cerri, M. J. Simões, and P. S. Cerri. Biology of Bone Tissue: Structure, Function, and Factors That Influence Bone Cells. *BioMed Research International*, 2015:421746, 2015.

[5] T. Albrektsson and C. Johansson. Osteoinduction, osteoconduction and osseointegration. *European Spine Journal*, 10:S96–S101, 2001.

[6] E. Colaço, C. Guibert, J. Lee, E. Maisonhaute, D. Brouri, C. Dupont-Gillain, K. El Kirat, S. Demoustier-Champagne, and J. Landoulsi. Embedding collagen in multilayers for enzyme-assisted mineralization: a promising way to direct crystallization in confinement. *Biomacromolecules*, Status: Submitted.

[7] C. Frantz, K. M. Stewart, and V. M. Weaver. The extracellular matrix at a glance. *Journal of Cell Science*, 123(24):4195–4200, 2010.

[8] H. Ao, C. Lin, B. Nie, S. Yang, Y. Xie, Y. Wan, and X. Zheng. The synergistic effect of type i collagen and hyaluronic acid on the biological properties of Col/HA-multilayer-modified titanium coatings: An in vitro and in vivo study. *RSC Advances*, 7(42):25828–25837, 2017.

[9] Y. Kim, H. Ko, I. K. Kwon, and K. Shin. Extracellular Matrix Revisited: Roles in Tissue Engineering. *International Neurourology Journal*, 20(2):168–168, 2016.

[10] J. Nicolas, S. Magli, L. Rabbachin, S. Sampaolesi, F. Nicotra, and L. Russo. 3D Extracellular Matrix Mimics: Fundamental Concepts and Role of Materials Chemistry to Influence Stem Cell Fate. *Biomacromolecules*, 21(6):1968–1994, 2020.

[11] P. H. Schlesinger, H. C. Blair, D. B. Stolz, V. Riazanski, E. C. Ray, I. L. Tourkova, and D. J. Nelson. Cellular and extracellular matrix of bone, with principles of synthesis and dependency of mineral deposition on cell membrane transport. *American Journal of Physiology - Cell Physiology*, 318(1):C111–C124, 2020.

[12] W. Friess. Collagen - Biomaterial for drug delivery. *European Journal of Pharmaceutics and Biopharmaceutics*, 45(2):113–136, 1998.

[13] J. Landoulsi, S. Demoustier-Champagne, and C. Dupont-Gillain. Self-assembled multilayers based on native or denatured collagen: Mechanism and synthesis of size-controlled nanotubes. *Soft Matter*, 7(7):3337–3347, 2011.

[14] P. H. Byers and J. F. Bonadio. 4 - The molecular basis of clinical heterogeneity in osteogenesis imperfecta: Mutations in type I collagen genes have different effects on collagen processing. In June K Lloyd and Charles R Scriver, editors, *Genetic and Metabolic Disease in Pediatrics*, Butterworths International Medical Reviews, pages 56–90. Butterworth-Heinemann, 1985.

[15] A. M. Ferreira, P. Gentile, V. Chiono, and G. Ciardelli. Collagen for bone tissue regeneration. *Acta Biomaterialia*, 8(9):3191–3200, 2012.

[16] P. Zhai, X. Peng, B. Li, Y. Liu, H. Sun, and X. Li. The application of hyaluronic acid in bone regeneration. *International Journal of Biological Macromolecules*, 151:1224–1239, 2020.

[17] L. Liu, Y. Liu, J. Li, G. Du, and J. Chen. Microbial production of hyaluronic acid: current state, challenges, and perspectives. *Microbial Cell Factories*, 10(1):99, 2011.

[18] S. Amorim, C. A. Reis, R. L. Reis, and R. A. Pires. Extracellular Matrix Mimics Using Hyaluronan-Based Biomaterials. *Trends in Biotechnology*, 39(1):90–104, 2021.

[19] C. E. Schanté, G. Zuber, C. Herlin, and T. F. Vandamme. Chemical modifications of hyaluronic acid for the synthesis of derivatives for a broad range of biomedical applications. 85:469–489, 2011.

[20] L. Silvester, J. Lamonier, R. Vannier, C. Lamonier, M. Capron, A. Mamede, F. Pourpoint, A. Gervasini, and F. Dumeignil. Structural{,} textural and acid–base properties of carbonate-containing hydroxyapatites. *J. Mater. Chem. A*, 2(29):11073–11090, 2014.

[21] Y. Lu, W. Dong, J. Ding, W. Wang, and A. Wang. *Hydroxyapatite Nanomaterials: Synthesis, Properties, and Functional Applications*. Elsevier Inc., 2019.

[22] K. Lin and J. Chang. *Structure and properties of hydroxyapatite for biomedical applications*, pages 3–19. Number 8. 12 2015.

[23] M. Uddin, T. Matsumoto, M. Okazaki, A. Nakahira, and T. Sohmura. *Biomimetic Fabrication of Apatite Related Biomaterials*. 03 2010.

[24] J. An, S. Leeuwenburgh, J. Wolke, and J. Jansen. Mineralization Processes in Hard Tissue: Bone. *Biomineralization and Biomaterials: Fundamentals and Applications*, pages 129–146, 2016.

[25] M. Murshed. Mechanism of Bone Mineralization. *Cold Spring Harbor perspectives in medicine*, 8(12):1–12, 2018.

[26] Y. C. Chai, A. Carlier, J. Bolander, S. J. Roberts, L. Geris, J. Schrooten, H. Van Oosterwyck, and F. P. Luyten. Current views on calcium phosphate osteogenicity and the translation into effective bone regeneration strategies. *Acta Biomaterialia*, 8(11):3876–3887, 2012.

[27] H. Orimo. The mechanism of mineralization and the role of alkaline phosphatase in health and disease. *Journal of Nippon Medical School*, 77(1):4–12, 2010.

[28] L. Yu and M. Wei. Biomineralization of collagen-based materials for hard tissue repair. *International Journal of Molecular Sciences*, 22(2):1–17, 2021.

[29] F. Nudelman, A. J. Lausch, N. A.J.M. Sommerdijk, and E. D. Sone. In vitro models of collagen biomineralization. *Journal of Structural Biology*, 183(2):258–269, 2013.

[30] B. M. Oosterlaken, M. P. Vena, and G. de With. In Vitro Mineralization of Collagen. *Advanced Materials*, 2004418, 2021.

[31] U. Sharma, D. Pal, and R. Prasad. Alkaline phosphatase: An overview. *Indian Journal of Clinical Biochemistry*, 29(3):269–278, 2014.

[32] J. L. Millán. Alkaline phosphatases. *Purinergic Signalling*, 2(2):335–341, 2006.

[33] T.E.L. Douglas, P.B. Messersmith, S. Chasan, A.G. Mikos, E.L.W. de Mulder, G. Dickson, D. Schaubroeck, L. Balcaen, F. Vanhaecke, P. Dubruel, J.A. Jansen, and S.C.G. Leeuwenburgh. Enzymatic Mineralization of Hydrogels for Bone Tissue Engineering by Incorporation of Alkaline Phosphatase. *Macromolecular Bioscience*, 12(8):1077–1089, 2012.

[34] N. Li, L. Zhou, W. Xie, D. Zeng, D. Cai, H. Wang, C. Zhou, J. Wang, and L. Li. Alkaline phosphatase enzyme-induced biomineralization of chitosan scaffolds with enhanced osteogenesis for bone tissue engineering. *Chemical Engineering Journal*, 371:618–630, 2019.

[35] J. Yao, W. Fang, J. Guo, D. Jiao, S. Chen, S. Ifuku, H. Wang, and A. Walther. Highly Mineralized Biomimetic Polysaccharide Nanofiber Materials Using Enzymatic Mineralization. *Biomacromolecules*, 21(6):2176–2186, 2020.

[36] A. Aminian, K. Pardun, E. Volkmann, G. Li Destri, G. Marletta, L. Treccani, and K. Rezwan. Enzyme-assisted calcium phosphate biomineralization on an inert alumina surface. *Acta Biomaterialia*, 13:335–343, 2015.

[37] E. Colaço, D. Lefèvre, E. Maisonhaute, D. Brouri, C. Guibert, C. Dupont-Gillain, K. El Kirat, S. Demoustier-Champagne, and J. Landoulsi. Enzyme-assisted mineralization of calcium phosphate: exploring confinement for the design of highly crystalline nano-objects. *Nanoscale*, 12(18):10051–10064, 2020.

[38] N. Rauner, M. Meuris, M. Zoric, and J.C. Tiller. Enzymatic mineralization generates ultrastiff and tough hydrogels with tunable mechanics. *Nature*, 543(7645):407–410, 2017.

[39] A. Biswas, I. S. Bayer, A. S. Biris, T. Wang, E. Dervishi, and F. Faupel. Advances in top-down and bottom-up surface nanofabrication: Techniques, applications & future prospects. *Advances in Colloid and Interface Science*, 170(1-2):2–27, 2012.

[40] S. K. Chakarvarti and J. Vetter. Template synthesis - A membrane based technology for generation of nano-/micro materials: A review. *Radiation Measurements*, 29(2-6):149–159, 1998.

[41] A. Karataş and A. H. Algan. Template synthesis of tubular nanostructures for loading biologically active molecules. *Current topics in medicinal chemistry*, 17, 12 2016.

[42] it4ip. DEVELOPER, MANUFACTURER AND SUPPLIER OF TRACK-ETCHED MEMBRANE FILTERS. `https://www.it4ip.be`. [Online; Accessed 6 April 2021].

[43] M. H. Asghar, F. Placido, and S. Naseem. Characterization of reactively evaporated TiO 2 thin films as high. *European Physical Journal Applied Physics*, 184(3):177–184, 2006.

[44] Y. Wang, A. S. Angelatos, and F. Caruso. Template synthesis of nanostructured materials via layer-by-layer assembly. *Chemistry of Materials*, 20(3):848–858, 2008.

[45] K. Ariga, J. P. Hill, and Q. Ji. Layer-by-layer assembly as a versatile bottom-up nanofabrication technique for exploratory research and realistic application. *Physical Chemistry Chemical Physics*, 9(19):2319–2340, 2007.

[46] J. J. Richardson, J. Cui, M. Björnmalm, J. A. Braunger, H. Ejima, and F. Caruso. Innovation in Layer-by-Layer Assembly. *Chemical Reviews*, 116(23):14828–14867, 2016.

[47] C. J. Roy, C. Dupont-Gillain, S. Demoustier-Champagne, A. M. Jonas, and J. Landoulsi. Growth mechanism of confined polyelectrolyte multilayers in nanoporous templates. *Langmuir*, 26(5):3350–3355, 2010.

[48] H. Alem, F. Blondeau, K. Glinel, S. Demoustier-Champagne, and A. M. Jonas. Layer-by-layer assembly of polyelectrolytes in nanopores. *Macromolecules*, 40(9):3366–3372, 2007.

[49] T. D. Lazzara, K. H. Aaron Lau, W. Knoll, A. Janshoff, and C. Steinem. Macromolecular shape and interactions in layer-by-layer assemblies within cylindrical nanopores. *Beilstein Journal of Nanotechnology*, 3(1):475–484, 2012.

[50] A. vander Straeten, D. Lefèvre, S. Demoustier-Champagne, and C. Dupont-Gillain. Protein-based polyelectrolyte multilayers. *Advances in Colloid and Interface Science*, 280, 2020.

[51] D. G. Ramírez-Wong, C. Coelho-Diogo, C. Aimé, C. Bonhomme, A. M. Jonas, and S. Demoustier-Champagne. Effects of geometrical confinement in membrane pores on enzyme-based layer-by-layer assemblies. *Applied Surface Science*, 338:154–162, 2015.

[52] A. S. De León, T. Garnier, L. Jierry, F. Boulmedais, A. Muñoz-Bonilla, and J. Rodríguez-Hernández. Enzymatic Catalysis Combining the Breath Figures and Layer-by-Layer Techniques: Toward the Design of Microreactors. *ACS Applied Materials and Interfaces*, 7(22):12210–12219, 2015.

[53] D. Lefèvre, J. Louvegny, M. Naudin, E. Ferain, C. Dupont-Gillain, and S. Demoustier-Champagne. Biofunctionalized and self-supported polypyrrole frameworks as nanostructured ECM-like biointerfaces. *RSC Advances*, 8(41):22932–22943, 2018.

[54] OriginLab Corporation USA. OriginPro, Version 8.5.1, 2011.

[55] E. Colaço, D. Brouri, C. Méthivier, L. Valentin, F. Oudet, K. El Kirat, C. Guibert, and J. Landoulsi. Calcium phosphate mineralization through homogenous enzymatic catalysis: Investigation of the early stages. *Journal of Colloid and Interface Science*, 565:43–54, 2020.

[56] K. J. Kang, B. H. Min, J. H. Lee, E. R. Kim, C. O. Sung, J. Y. Cho, S. W. Seo, and J. J. Kim. Alginate hydrogel as a potential alternative to hyaluronic acid as submucosal injection material. *Digestive Diseases and Sciences*, 58(6):1491–1496, 2013.

[57] M. Rubert, M. Alonso-Sande, M. Monjo, and J. M. Ramis. Evaluation of alginate and hyaluronic acid for their use in bone tissue engineering. *Biointerphases*, 7(1-4):1–11, 2012.

[58] D. Gregurec, G. Wang, R. H. Pires, M. Kosutic, T. Lüdtke, M. Delcea, and S. E. Moya. Bioinspired titanium coatings: Self-assembly of collagen-alginate films for enhanced osseointegration. *Journal of Materials Chemistry B*, 4(11):1978–1986, 2016.

[59] FooDB. Showing compound sodium alginate. `https://foodb.ca/compounds/FDB019541`. [Online; Accessed 26 May 2021].

[60] L. Richert, F. Boulmedais, P. Lavalle, J. Mutterer, E. Ferreux, G. Decher, P. Schaaf, J. C. Voegel, and C. Picart. Improvement of stability and cell adhesion properties of polyelectrolyte multilayer films by chemical cross-linking. *Biomacromolecules*, 5(2):284–294, 2004.

# Appendix A

# Non-mineralized nanotubes

This appendix aims at showing the morphology of non-mineralized nanotubes obtained by scanning electron microscopy (SEM).
These nanotubes were build up by the LbL assembly of five multilayers $(PAH/ALP)_5$ in the parallel pores of a PC membrane. To dissolve the template and collect the formed nanotubes, the PC membrane was deposited on a PET filter, coated with a thin layer of gold, and $\sim$50 mL of dichloromethane ($CH_2Cl_2$) was poured dropwise onto it. The obtained nanotubes were then observed by SEM (JSM- 7600F, Jeol) at 5 kV and the acquired images are shown in Figure A.1.

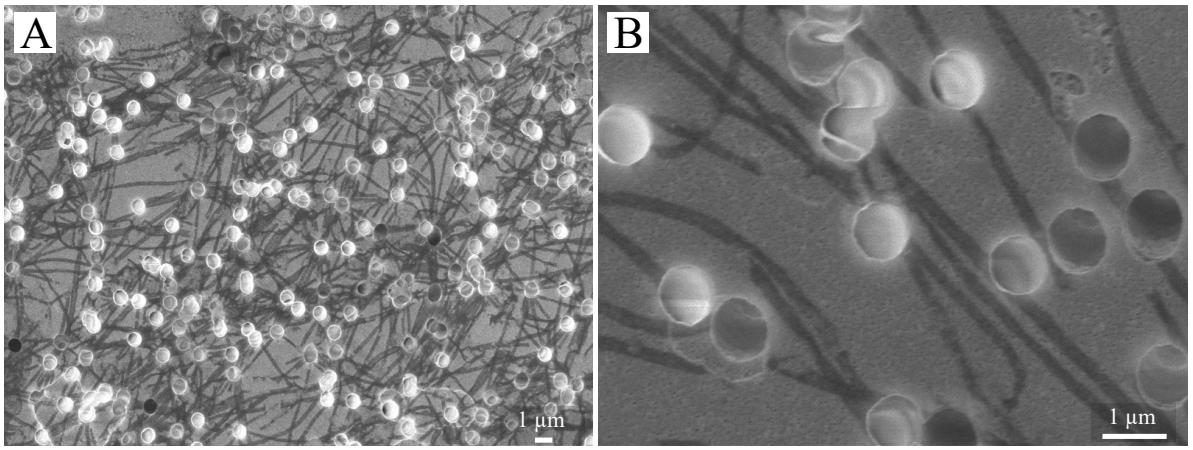


Figure A.1: SEM images of non-mineralized $(PAH/ALP)_5$ nanotubes formed in PC membranes with parallel nanopores (300 nm diameter) at low magnification (A) and high magnification (B).

**UNIVERSITÉ CATHOLIQUE DE LOUVAIN**
**École polytechnique de Louvain**
Rue Archimède, 1 bte L6.11.01, 1348 Louvain-la-Neuve, Belgique | **www.uclouvain.be/epl**